X-ray Standing Waves Analyses
at Solid/Liquid Interfaces

Dissertation
at the Department of Physics
Technische Universität Dortmund

Martin Brücher

2010

Contents

List of Figures

3

Chapter 1

Introduction

1.1   Motivation

Interfaces between solids and liquids are omnipresent in nature and of great importance in many fields of biology, chemistry, medicine and research. Here, a multitude of processes which are important for life and health, like the transport of ions through cell membranes or the adsorption of bacteria and proteins on surfaces takes place [1, 2]. In general, solid/liquid interfaces are charged and many of the processes mentioned above are controlled or influenced by the electric interfacial potential [3, 4, 5]. Therefore, for a comprehensive understanding of interfaces and the related phenomena, knowledge of this so-called ζ-potential and the distribution of charges is necessary. Not only natural surfaces and their charge are of interest, but also the systematic modification of surfaces in order to control and influence the properties of interfaces and fluids [6, 7, 8, 9]. Such surface functionalization methods are of particular relevance for the development of microfluidic devices [10, 11].

However, possibilities of experimental analysis of the ζ-potential are restricted, mainly for two reasons: The presence of a liquid phase excludes all methods depending on vacuum conditions; and the lateral extension of the ζ-potential, typically limited to few nanometres, requires a high spatial resolution. These restrictions are overcome by the experimental method described in this work, known as X-ray standing Waves (XSW) measurements. The distribution of ions adjacent to the surface, indicating the strength of the ζ-potential, is scanned vertically using XSW. X-ray standing waves are stationary electromagnetic interference fields generated by interference of an incoming an a reflected X-ray beam. The intensity of XSW-excited fluorescence as a function of the incident

angle enables the determination of element concentration profiles in the sample volume near the interface. X-ray standing waves have proven to be a well-suited tool for the study of nanometre-sized structures. The method is non-destructive, element sensitive and compatible to atmospheric pressure. The experiments performed are summarized below.

Surface Functionalizations

The experiments described in the third chapter are dedicated to the analysis of functionalized solid/liquid interfaces. First, the influence of a surface modification by functional groups on the interfacial charge and potential is studied. Results from the measurement of the streaming current yielding ζ-potential values and XSW scans of the diffuse ion layer are combined for the quantitative determination of the interfacial charge density. A detailed discussion of the evaluation of XSW-excited fluorescence signals is included, explaining the correction of the effects which are induced by the morphology of the sample and the influence of scattering.

A further functionalization type is the coating of a surface with polymer brushes, which is of particular interest for the control of flows in microfluidic devices. Here, a combination of infrared ellipsometry and XSW scans was applied to determine the pH-dependent behavior of the brushes and their influence on wetting properties of the surface, respectively.

Polymer Layers

The second class of samples investigated in the framework of these studies are thin polymer layers containing an inhomogeneous distribution of sulfur ions. These samples are applied to the development of a novel fabrication process for organic light emitting diodes (OLEDs). Here, the main target of XSW experiments is the detection and characterization of a thin front of sulfur ions at low concentration. Herewith, a proposed polymer crosslinking mechanism is verified.

Although the actual topic of this work is the analysis of solid/liquid interfaces, the present sample type fits into the scope of the studies: In terms of reflection, refraction and absorption of X-rays, the polymer layers correspond to thin liquid films and can therefore regarded as solid-state solutions.

Furthermore, the initiation of the crosslinking process is observed in a series of experiments recorded during the reaction. The investigation of element distribution within

the polymer layers not only provides insight into the sample structure and the reaction process, but also helps to understand the limitations of applicability of the experimental method: The vertical extension of the standing waves field is determined, which enables the estimation of the measuring range.

1.2 Historical Background

Shortly after the discovery of X-rays by Röntgen in 1895, the value of this new type of radiation for analytical purposes was recognized. The diffraction experiments at crystals performed by M. v. Laue in 1912 were the first analyses of structures of atomic and molecular size taking advantage of X-ray interference. With the work of Moseley, who introduced the principles of element identification using X-ray fluorescence spectrometry (1913) and Compton, who first reported on total reflection of X-rays (1923), the foundations of the XSW method were laid [12, 13].

But only in 1971, Yoneda and Horiuchi combined these advantageous properties in the development of total-reflection X-ray fluorescence analysis (TXRF), which has become an established method in analytical chemistry [14, 15]. In the following years, instrumentation was developed and also first experiments using synchrotron radiation were performed [16, 17]. In the field of solid/liquid samples, XSW generated by total external and Bragg reflection have proven useful for the analysis of various interfacial processes and phenomena [18, 19], including the adsorption of ions, biofilms and proteins on surfaces [20, 21, 22, 23], the study of biologically relevant membranes [24, 25, 26, 27] and surface reactivity [28, 29].

Compared to other X-ray related analytical techniques, XSW experiments are of relatively limited application, mainly due to the special demands on beam quality which are only practically met by synchrotron radiation.

Chapter 2

Theoretical Background

2.1 Charged Solid/Liquid Interfaces

2.1.1 Ion Distribution Models

In general, interfaces between solids and solutions are charged. This is mainly due to dissociation of surface groups or to adsorption of ions from the solution onto a neutral surface [30, 31]. This charge and the resulting potential is of great relevance for many interfacial processes, but cannot be measured directly. Therefore, the distribution of ions at the interface, which is determined by the electric potential, is of particular interest for the analysis of solid/liquid interfaces.

For the description of ion distributions, several models have been developed, of which three fundamental ones are shown in Figure 2.1. In the simplest model (**a**), proposed by Helmholtz [32], the charge of the solid surface is compensated by a layer of adsorbed (oppositely charged) counterions. Above this adsorbed layer, the solution is charge neutral. The second model (**b**), developed by Gouy and Chapman [33, 34], gives a more appropriate representation of the interface by taking into account the thermal motion of ions in the solution. This motion leads to the formation of a diffuse ion layer of exponentially decreasing counterion concentration, which shields the interfacial charge. With decreasing strength of the potential, the concentration of (equally charged) co-ions rises. Considering co- and counterions, the diffuse ion layer is also referred to as *electric double layer* (EDL). In the bulk solution far from the interface, the concentration of both ion types is constant (bulk concentration). The Stern model (**c**) combines the features of the previously discussed models [35], consisting of an adsorbed layer and the diffuse layer of the Gouy-Chapman model. The thickness of the Stern layer determines the position of
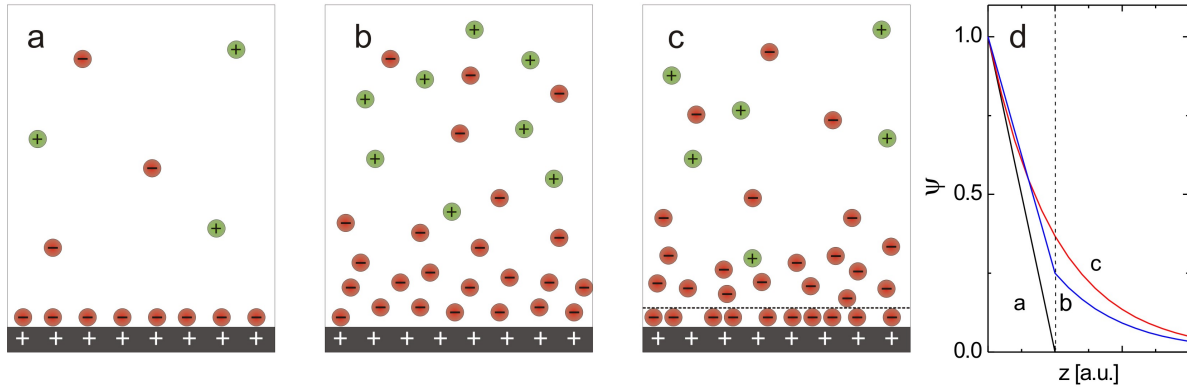
Figure 2.1: Models for the distribution of ions adjacent to a charged interface according to Helmholtz (**a**), Gouy / Chapman (**b**) and Stern (**c**). The plot **d** schematically shows the relative potential strength $\psi(z)$ for each case. The dashed line in **c** and **d** indicates the shear plane, separating adsorbed and mobile ions.

the shear plane which constitutes the boundary between mobile and immobilized ions. For the analysis of the properties of charged solid/liquid interfaces with XSW, the diffuse ion layer is the most interesting part of the ion distribution. In the following discussion, a short derivation of the parameters which will be used for the characterization of the charge and the potential of the interface is given.

2.1.2 The Poisson-Boltzmann Equation

The Poisson equation is the fundamental equation for the description of the electric potential of a distribution of charges. For the discussion of the characteristics of ion distributions in the electric potential above a surface, a charged plane is considered [36]. The potential ψ of the interfacial charge is determined by the Poisson equation

$$\nabla^2 \psi = \frac{-\rho}{\varepsilon_r \varepsilon_0} \tag{2.1}$$

with the charge density ρ, vacuum permittivity ε_0 and relative permittivity ε_r. The concentration of (oppositely charged) counterions within this potential is given by the Boltzmann equation

$$n_i = n_i^0 \exp\left(\frac{-c_i e \psi}{kT}\right) \tag{2.2}$$

c_i is the valency of ion species i and n_i^0 is its bulk concentration far from the interface. This concentration is not any more influenced by the ζ-potential and therefore is constant. Considering all i ion species of the solution, the relation between the potential and the ion concentration is given by the Poisson-Boltzmann equation:

$$\nabla^2 \psi = \frac{-1}{\varepsilon_0 \varepsilon_r} \sum_i n_i^0 c_i e \exp\left(\frac{-c_i e \psi}{kT}\right). \tag{2.3}$$

Assuming a small potential ($e\psi \ll kT$), the Poisson-Boltzmann equation can be expanded:

$$\nabla^2 \psi = \frac{-1}{\varepsilon_0 \varepsilon_r}\left[\sum_i c_i e n_i^0 - \sum_i c_i^2 e^2 n_i^0 \psi / kT\right]. \tag{2.4}$$

Due to the neutrality of the bulk solution, the first sum has to be zero, which leads to the following linear approximation:

$$\nabla^2 \psi = \left[\frac{\sum_i^2 e^2 n_i^0}{\varepsilon_0 \varepsilon_r kT}\right]\psi = \kappa^2 \psi \tag{2.5}$$

with the Debye-Hückel parameter κ. Equation 2.5 is solved by exponentially decreasing potentials of the type $\psi(z) = \psi_0 \exp(-\kappa z)$. The inverse of the Debye-Hückel parameter is the Debye length $L_D = 1/\kappa$, which is a measure for the extension of the diffuse ion layer. At $z = L_D$, the concentration of counterions has decreased to $1/e \approx 37\%$, the influence of the interfacial potential extends over a range of $3L_D$ to $4L_D$.

However, in the case of most interesting charged interfaces, the condition for small potentials $e\psi \ll kT$ is not fulfilled and the approximation discussed above cannot be made. Therefore, the Debye length of the counterion distribution above the analyzed interfaces will be determined experimentally applying X-ray standing waves.

2.1.3 The Interfacial Charge

The charge σ of the surface (per unit area) is balanced by the charge of the counterions of the diffuse layer:

$$\sigma = \int_0^\infty \rho(z)dz \tag{2.6}$$

or, using the Poisson equation,

$$\sigma = -\int_0^\infty \varepsilon_0 \varepsilon_r \frac{d^2\psi}{dz^2} dz = \varepsilon_0 \varepsilon_r \left[\frac{d\psi}{dz}\right]_\infty^0. \tag{2.7}$$

In the bulk solution ($z \to \infty$) the potential is constant, so the surface charge is given by

$$\sigma = \varepsilon_0 \varepsilon_r \frac{d\psi_0}{dz} \tag{2.8}$$

with $\psi_0 = \psi(z = 0)$. The integration of the complete (one-dimensional) Poisson-Boltzmann equation yields:

$$\frac{d\psi}{dz} = -\frac{2\kappa kT}{ce} \sinh\left(\frac{ce\psi_0}{2kT}\right). \tag{2.9}$$

Inserting into equation 2.7 gives:

$$\sigma = -\frac{2\kappa\varepsilon_0\varepsilon_r kT}{ce} \sinh\left(\frac{ce\psi_0}{2kT}\right), \tag{2.10}$$

the so-called Grahame equation [30, 37]. Thus, knowing the values of ψ_0 and $L_D = 1/\kappa$, the interfacial charge can be calculated. In the following, the experimental methods for the measurement of these parameters, summarized in Table 2.1, will be discussed.

Parameter	Variable	Unit	Exp. Method
ζ-Potential	ψ_0	mV	Streaming Current
Debye Length	L_D	nm	XSW
Surface Charge	σ	mC/m^2	-

Table 2.1: Parameters and experimental methods related to the characterization of charged solid/liquid interfaces described in this work.

2.2 Streaming Current Measurements

The ζ-potential ψ_0 at the interface is determined by the electrokinetic measurement of the streaming current. Figure 2.2 schematically shows the experimental setup: An electrolyte solution is driven by external pressure through a channel or a capillary of the sample material. The flow also carries downstream the accumulated counterions of the diffuse layer, causing a net charge transport, the streaming current. As the concentration of counterions of the diffuse layer depends on the ζ-potential, the streaming current is related to ψ_0 [31]:

$$I_s = \frac{\varepsilon\varepsilon_0\psi_0}{\eta}\frac{\Delta P}{L}A.$$ (2.11)

where η is the viscosity of the electrolyte, $\Delta P/L$ the pressure gradient along the channel length and A the cross section of the channel or capillary.
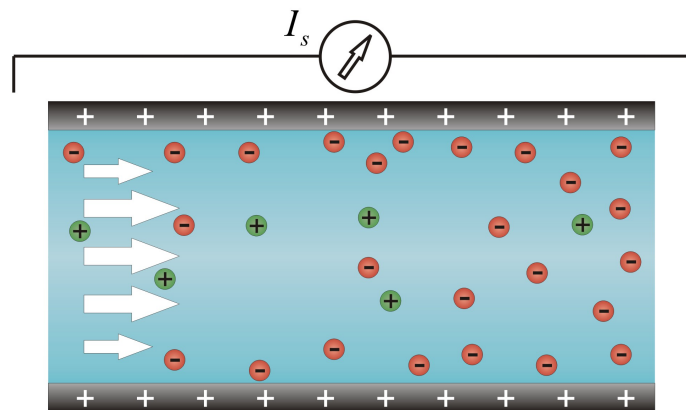
Figure 2.2: Principle of the measurement of the streaming current. The flow in the channel or capillary moves the electric double layer, causing the streaming current I_s.

2.2.1 Titration Reactions at Interfaces

The strength and polarity of an interfacial potential is determined by the interaction of the charges of functional surface groups with the ions in the liquid phase. This interaction is described by titration reactions. The pH dependent reaction equilibrium of two interfaces bearing different functional groups A and B is considered. Equation 2.12 **a** describes the

protonation of molecule A in acidic solution, inducing a positive ζ-potential at low pH values. A negative surface charge is induced by the deprotonation of the hydroxyl groups of molecule B, represented by equation 2.12 **b**:

$$\text{A} + \text{H}_3\text{O}^+ \rightleftharpoons \text{A-H}^+ + \text{H}_2\text{O} \qquad\qquad \text{(a)}$$
$$\text{B-OH} + \text{OH}^- \rightleftharpoons \text{B-O}^- + \text{H}_2\text{O} \qquad\qquad \text{(b).}$$

$$(2.12)$$

In the case of interfaces comprising several types of functional groups, the ζ-potential is given by the superimposition of the potentials induced by the single reactions. An example is plotted in Figure 2.3 (curve **c**). The pH value, for which positive and negative charges balance out each other, causing a neutral interface, is called the *isoelectric point*.
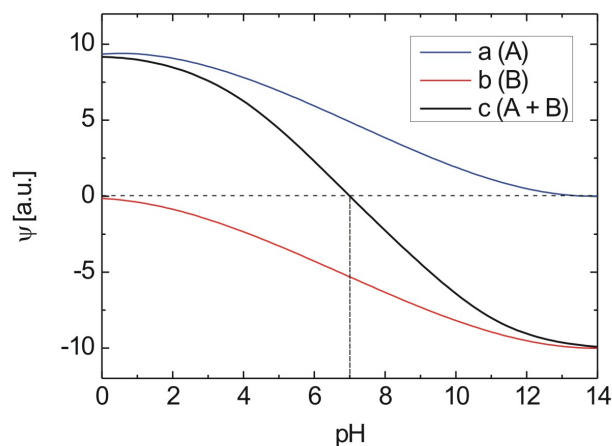
Figure 2.3: Titration curves for interfaces with different types surface groups determining the charge. In curve **a**, the pH dependent ζ-potential induced by functional groups of type A, being protonated in acidic solution, is plotted and curve **b** shows the potential corresponding to a deprotonation of hydroxyl groups (B) with rising pH. The potential of an interface bearing functional groups of both types is represented by curve **c**. At pH 7, the isoelectric point ($\psi_c = 0$) of the interface described by curve **c** is passed.

2.3   Principles of X-ray Standing Waves

2.3.1   X-ray Fluorescence

X-rays are electromagnetic waves of short wavelength, following the ultraviolet range in the electromagnetic spectrum. Their energy, in the present work generally given in kiloelectronvolts (keV), is related to the wavelength λ and can be calculated by

$$E = \frac{h\nu}{c} = \frac{1.2397}{\lambda[\text{nm}]} \text{ keV}. \tag{2.13}$$

X-rays can be produced in the form of *primary* and *secondary* radiation. For the generation of primary X-rays, charged particles (electrons or positrons), are accelerated in electric fields (as in X-ray tubes) or magnetic fields (bending magnets or insertion devices of synchrotrons). Secondary X-rays are emitted by the transition of an electron from one energy level of an atom to a lower one. The principle of this process is shown in Figure 2.4.
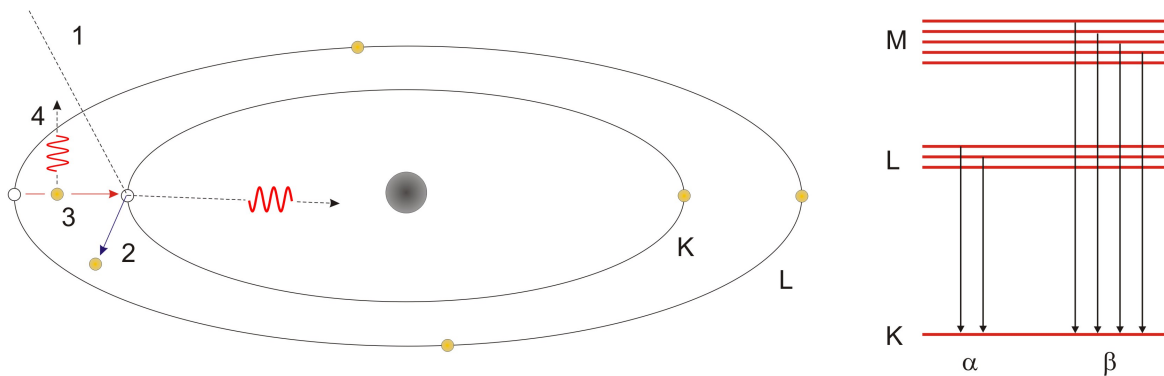
Figure 2.4: Left: Principle of X-ray fluorescence excitation. An incoming X-ray photon (1) expels an electron of an inner shell of the atom (2). An electron from a higher energy level moves, filling the vacancy (3). The energy difference between the two shells is balanced by the fluorescent emission of a photon (4). In the picture, the excitation of the $K\alpha$ line of carbon is shown as an example. Right: $K\alpha$ and $K\beta$ electron transitions.

Referring to Figure 2.4, the basic principle of X-ray fluorescence spectrometry is explained as follows: A primary X-ray photon of wavelength $\lambda = c/\nu$ hits an electron of

one of the inner shells and, if the photon energy $h\nu$ is higher than its binding energy, removes it. To restore an energetically favorable state, a second electron from a higher energy level moves and occupies the vacant position. The energy difference between the two shells is compensated by the fluorescent emission of a (secondary) photon. Its energy is approximately determined by the principal quantum numbers n_1 and n_2 of the two shells and by the atomic number Z of the irradiated element:

$$E_{ph} = \frac{Z^2 e^4 m_0}{32\pi^2 \varepsilon_0^2 \hbar^2} \left(\frac{1}{n_2^2} - \frac{1}{n_1^2} \right).$$
(2.14)

In the example of the carbon $K\alpha$ transition shown in Figure 2.4, the values are $Z = 6$, $n_1 = 1$ and $n_2 = 2$. By this transition, a photon of $E_{ph} = 0.277$ keV is emitted. As a consequence of this, elements can be identified by the spectrum of their characteristic X-ray fluorescent emission. A more detailed introduction into X-ray fluorescence spectrometry can be found in the references [38] and [39].

2.3.2 Reflection and Refraction of X-rays

The basic principles and conditions for the generation of X-ray standing waves fields will be discussed below [41, 42]. An X-ray beam passing the interface between two media of different electron density is considered. The deflection of the incident beam, schematically shown in Figure 2.5, is described by Snell's law of refraction

$$n_1 \cos \alpha_i = n_2 \cos \alpha_t$$
(2.15)

where α_i and α_t are the angles of the incident and transmitted beam relative to the surface, respectively. For grazing incidence X-rays, angles are measured relative to the surface instead of to its normal, as it is usually done in optics.

The (complex) refractive indices of the media n_1 and n_2 are defined by

$$n = 1 - \delta + i\beta$$
(2.16)

with the imaginary unit[1] $i = \sqrt{-1}$. The real part δ is called the decrement and describes the dispersion of beam. Attenuation of the radiation in the medium is given by the

---

[1]Alternative notation: $n = 1 - \delta - i\beta$, in this case the sign of the complex term changes.
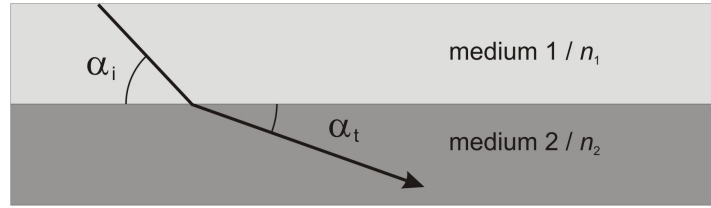
Figure 2.5: Refraction of an X-ray beam passing an interface between two media of different refractive indices. Here, medium 1 is optically thicker ($n_1 > n_2$).

imaginary part β. The two parameters depend on material properties of the irradiated media and on the wavelength λ of incident radiation

$$\delta = \frac{\lambda^2}{2\pi} r_e \rho_e \tag{2.17}$$

$$\beta = \frac{\lambda}{4\pi} \mu \tag{2.18}$$

with the classical electron radius $r_e = e^2/(4\pi\varepsilon_0 m_e c^2) = 2.814 \cdot 10^{-14}$ nm, electron density $\rho_e = N_A Z \rho / A$ (N_A: Avogadro's number, A: atomic mass) and the absorption coefficient μ. For X-rays, the parameters δ and β normally are of the order of magnitude 10^{-6} and 10^{-9}, respectively. The real part of the refractive index in media is smaller than in vacuum ($n < n_{vac} = 1$), thus X-rays hitting a vacuum/medium interface under grazing incidence are deflected towards the interface. A critical incident angle α_c exists, where the angle of the transmitted beam α_t is zero. If the electron density of medium 1 can be neglected, $\cos \alpha_c = n_2$ applies (from equations 2.15 and 2.16) and for the small incident angles used in XSW experiments, the following approximation can be used

$$\cos \alpha_c \approx 1 - \frac{\alpha_c^2}{2} \tag{2.19}$$

from which (considering only the dispersion given by δ) the critical angle can be calculated

$$\alpha_c = \sqrt{2\delta}. \tag{2.20}$$

At the interface of two media of both non-negligible electron density (example shown in
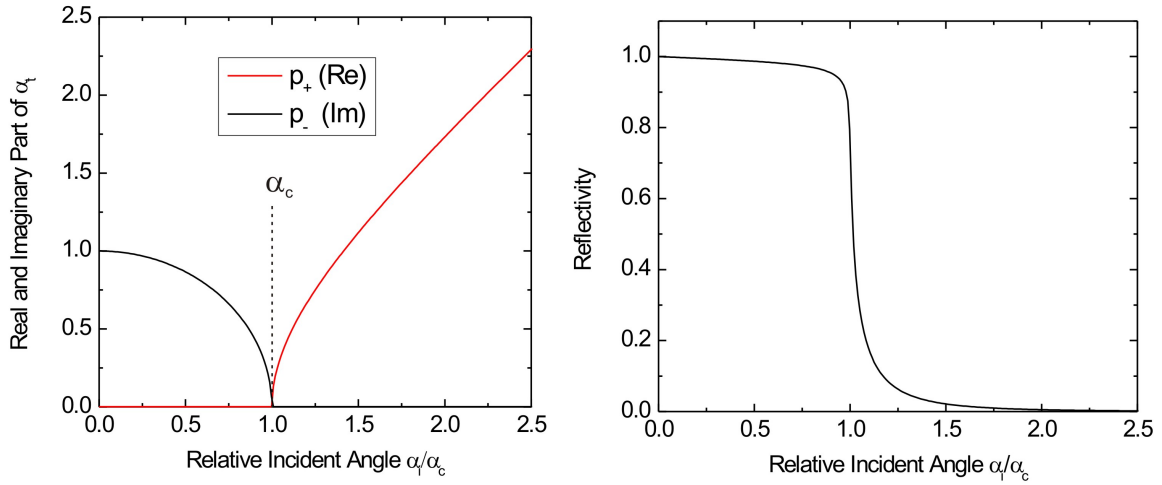
Figure 2.6: Left: Real and imaginary part of the transmission angle α_t. For $\alpha < \alpha_c$, incident radiation is reflected, α_t is imaginary. For incident angles exceeding the critical angle, α_t becomes real and the radiation penetrates into the medium. In the right graph, the calculated reflectivity curve of a Si surface is plotted. The x-axis of both plots is normalized to the critical angle α_c.

Figure 2.7), dispersion is determined by the difference of the two decrements $\delta = \delta_2 - \delta_1$. Using equations 2.15 and 2.16, the transmission angle α_t can be approximated by

$$\alpha_t = \sqrt{\alpha_i^2 - 2\delta + 2i\beta} \tag{2.21}$$

The real and the imaginary part of the transmission angle $\alpha_t = p_+ + ip_-$ is defined by the equation

$$p_{+/-}^2 = \frac{1}{2}\left[\sqrt{(\alpha_i^2 - \alpha_c^2)^2 + 4\beta^2} \pm (\alpha_i^2 - \alpha_c^2)\right] \tag{2.22}$$

The two components are plotted in Figure 2.6. For $\alpha_i \gg \alpha_c$, the real part of α_t asymptotically approximates α_i. Below the critical angle, equation 2.15 yields no real value for α_t. The transmission angle is complex and the incident wave does not penetrate into the medium. Instead, radiation is totally reflected at the interface [13, 40]. The intensity of the reflected beam is calculated according to the Fresnel formulas and is given by

$$R_F(\alpha_i) = \frac{(\alpha_i - p_+)^2 + p_-^2}{(\alpha_i + p_+)^2 + p_-^2}. \tag{2.23}$$

The left graph of Figure 2.6 gives an example of an ideal reflectivity curve calculated for a silicon substrate irradiated by X-rays of 15.5 keV energy. The intensity of the reflected beam is affected by the ratio β/δ and by the roughness of the reflecting surface. Different approaches exist to take into account roughness [41, 43], in the calculations discussed in this work it is done by multiplication of R_F with a Debye-Waller factor

$$r_{DW} = e^{\frac{-q_z^2 \sigma_{rms}^2}{2}} \tag{2.24}$$

with the vertical wave vector transfer $q_z = 4\pi \sin\alpha/\lambda$, σ_{rms} is the root-mean-square roughness.
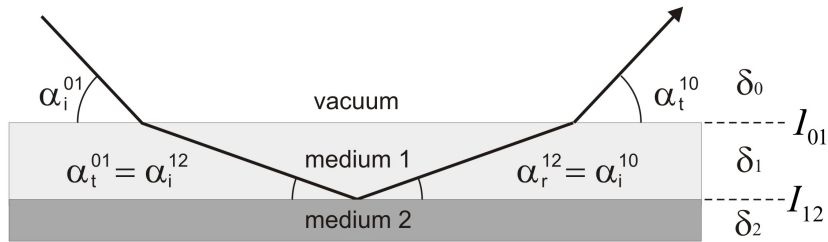
Figure 2.7: Refraction and reflection of an X-ray beam at a system of two interfaces. The beam, coming from vacuum ($\delta_0 = 0$), hits the interface I_{01} under an incident angle $\alpha_i^{01} > \sqrt{2\delta_1}$ and is transmitted into medium 1 under the angle α_t^{01}. The new incident angle α_i^{12} inside medium 1 is smaller than the critical angle of the interface between medium 1 and medium 2 ($\alpha_i^{12} < \sqrt{2(\delta_2 - \delta_1)}$), thus total reflection occurs at I_{12}.

Figure 2.7 demonstrates the refraction and reflection of X-rays at interfaces in the case of a beam path through a layered sample of different media. In the example, the parameters of radiation and sample material are chosen in such way that the beam is transmitted into medium 1 and then reflected at the interface between the media 1 and 2. The reflected beam is again refracted at the surface of medium 1 and leaves the sample under the exit angle $\alpha_t^{10} = \alpha_i^{01}$.

2.3.3   The X-ray Standing Waves Field

When a beam of monochromatic, coherent and parallel X-rays hits a plane surface with $\alpha_i < \alpha_c$, the incident and reflected part of the radiation interfere in the overlap region, generating the *X-ray standing waves* field. X-ray standing waves are stationary electromagnetic fields of alternating intensity minima (nodes) and maxima (antinodes) parallel to the reflecting surface. Figure 2.8 schematically shows the geometrical parameters and the vertical intensity distribution of an XSW field.
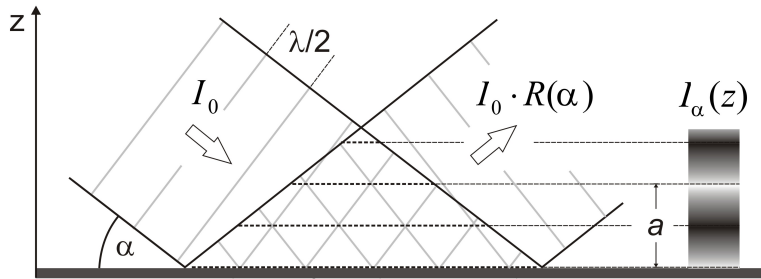
Figure 2.8: Schematic plot of an XSW field and its vertical intensity distribution $I_\alpha(z)$. The relation of wavelength λ to the distance a between two maxima is explained in the text.

The intensity of the field is a function of the incident angle α and the vertical distance z from the reflecting surface. In the following, the incident angle is referred to as α.

$$I(\alpha, z) = I_0 \left[1 + R(\alpha) + 2\sqrt{R(\alpha)} \cos(2\pi z/a - \phi(\alpha)) \right]. \tag{2.25}$$

The intensity of incoming beam is assumed to be constant. For the reflectivity $R \leq 1$ applies, as shown in Figure 2.6. The third term of equation 2.25 describes the interference of the incident and the reflected wave. The argument of the cosine includes the path difference of incoming and reflected wave $2\pi z/a$ and the phase shift $\phi(\alpha)$. Under total reflection conditions, the interference term takes values between $+2\sqrt{R(\alpha)}$ and $-2\sqrt{R(\alpha)}$. Depending on α and z, the summation of all three terms leads to the oscillation of intensity $I_\alpha(z)$ between 0 and $\leq 4 \cdot I_0$. The phase shift $\phi(\alpha)$ is given by

$$\phi(\alpha) = \arccos[2(\alpha/\alpha_c)^2 - 1]. \tag{2.26}$$

The phase shift has its maximal value of π at $\alpha = 0$, decreasing to zero at $\alpha = \alpha_c$. The distance a between two field nodes or antinodes is

$$a = \frac{\lambda}{2 \sin \alpha} \tag{2.27}$$

This distance decreases with increasing incident angle, its minimal value $a_{\min}$ is reached at the critical angle

$$a_{\min} = \frac{\lambda}{2 \sin \alpha_c} \tag{2.28}$$

Using radiation of constant wavelength, the vertical position of nodes and antinodes is changed by the variation of the incident angle. The increase of α shifts nodes and antinodes towards the surface and causes a compression of the XSW field. Figure 2.9 shows the vertical intensity distribution of some XSW fields calculated for X-rays of different energy and incident angle, reflected at a silicon surface. The parameters of these field are given in Table 2.2. The parameters of the fields are summarized in Table 2.2. The energy values of 10 and 15 keV were chosen according to the experiments, which will be discussed in the following chapters. Most measurements have been carried out using radiation of 15 - 15.5 keV, the corresponding field is shown in diagram **a** of Figure 2.9. The lowest energy applied to the generation of standing waves was 10 keV, the intensity distribution is displayed in plot **b**. Curves of same color represent fields of identical angle of incidence, so the dependency of the period a of the fields from λ and α can clearly be seen: The increase of energy, corresponding to a decrease of wavelength λ, reduces the distance between the respective nodes of the field. Comparing the curves plotted blue, red and black, which corresponds to incident angles of $\alpha = 0.039°, \alpha = 0.077°$ and $\alpha = 0.116°$, respectively, the compression of standing waves is obvious. For $E = 15$ keV, the first two chosen angles correspond to one third (blue) and two thirds of α_c (red); the black curve shows the maximal compression for the field at the critical angle. Here, the period of the standing waves field takes its minimal value $a_{\min}$. The vertical accuracy of XSW scans of elemental distributions, which will be explained in the next section, largely depends on this quantity.
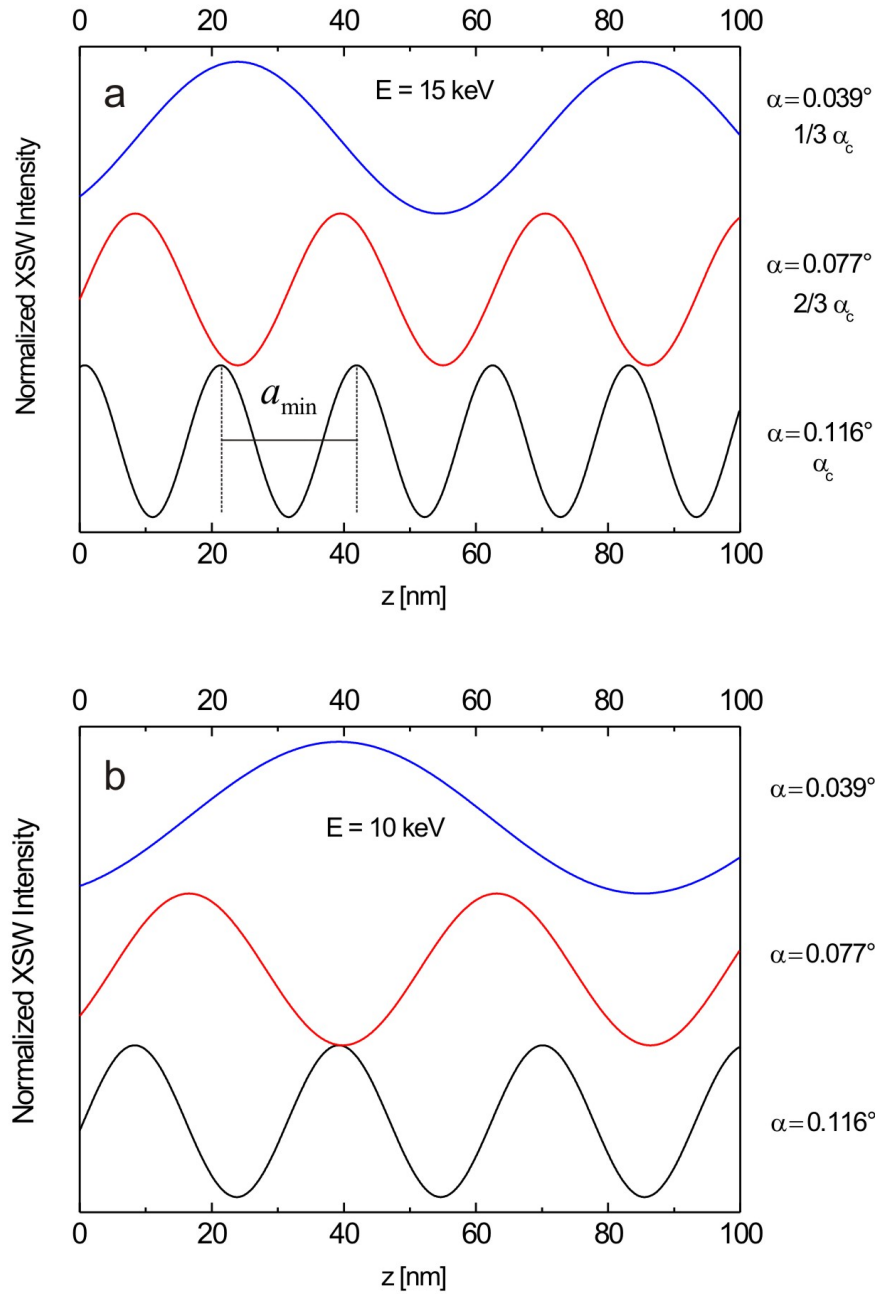
Figure 2.9: Vertical intensity distribution of XSW fields on a Si reflector for different energies and incident angles. Signals were calculated for an X-ray energy of 15 keV (**a**) and 10 keV (**b**). Incident angles are 0.039° (blue), 0.077° (red) and 0.116° (black). For $E = 15$ keV, the chosen angles correspond to $1/3\alpha_c, 2/3\alpha_c$ and α_c, respectively.

$I(z)$ graph	$\alpha[°]$	α/α_c ($E = 15$ keV)	$a_{15\text{keV}}$[nm]	$a_{10\text{keV}}$[nm]
blue	0.039	1/3	61.1	91.7
red	0.077	2/3	31.1	46.5
black	0.116	1	20.6	30.9

Table 2.2: Parameters of the XSW fields plotted in Figure 2.9.

2.3.4   Excitation of Marker Fluorescence

Now, a distribution of atoms or ions near on a surface or near an interface will be considered. This surface or interface is irradiated by a grazing-incidence X-ray beam and a standing waves field is produced, which overlaps the element distribution. Consequently, the fluorescence of these so-called markers is excited by the intensity maxima (antinodes) of the XSW field. Compared to conventional fluorescence excitation which is done using only the intensity of incident radiation I_0, the interference of incident and reflected beam in the XSW field according to equation 2.25 significantly amplifies the excitation of fluorescence. Thus, the detection limit of an analyte excited to fluorescence by XSW is considerably lower than in the case of conventional XRF analysis.

With angular resolved measurements of XSW-excited fluorescence, distribution of elements can be determined. As already mentioned, the position of XSW field maxima depends on the incident angle and the wavelength of the radiation. Usually, the wavelength is adjusted to a constant value for XSW experiments, so the variation of the incident angle is used to move the antinodes of the field through the marker distribution. For a given angle interval, typically ranging from $\alpha = 0$ to $\alpha \approx 1.5 \cdot \alpha_c$, the fluorescence of the atoms or ions within the XSW field is recorded, whereas the incident angle is increased stepwise. In doing so, the distribution of elements is scanned vertically.

The measured fluorescence signal is the product of the intensity of the XSW field $I(z)$ and the marker concentration at the respective height over the surface. The fluorescent photons from the entire vertical range of the sample volume are collected simultaneously, so the relative intensity of an XSW-excited marker distribution $D(z)$ is given by the integral

$$I(\alpha) = \int_0^{z_{\max}} I(\alpha, z) \cdot D(z) dz. \tag{2.29}$$

Assuming a typical value for the beam height of ca. 100 μm and a wavelength on the

order of magnitude of 0.1 nm, several hundreds maxima and minima are expected within the XSW field. However, the interference field does not fill the entire intersection volume of incoming and reflected beam, as in the idealized case shown in Figure 2.8, but extends only to a limited distance from the reflecting surface, which is indicated by the upper integration limit $z_{\max}$ [44]. This parameter determines the vertical extension of the XSW field, which is limited by the finite longitudinal coherence length of incoming and reflected radiation.

Later on, this issue will be analyzed in more detail and different factors influencing the vertical extension of the XSW field will be discussed. Furthermore, the fading of the interference field by the decrease of node/antinode contrast as a function of distance to the surface will be examined. Above $z_{\max}$, the interference field is replaced by the unmodulated overlap of incoming and reflected beam. Thus, the fluorescence of any markers situated in this region is excited by

$$I_{z>z_{\max}}(\alpha) = I_0\big[1 + R(\alpha)\big] \tag{2.30}$$

and may, for sufficient marker concentrations and $\alpha \leq \alpha_c$ contribute to the XSW-excited signal in the form of an intensity offset.

Depending on the volume and composition of the sample material covering the reflecting surface, scattered radiation may cause a further contribution to the excitation of marker fluorescence. Especially, when the interesting markers are embedded in a liquid, as for example ions in aqueous solutions, this effect must be taken into account. The correction of this influence will be discussed in the experimental section.

2.3.5   Simulation of Fluorescence Signals

Different types of elemental distributions have been analyzed in the context of these studies. The most important ones are exponentially decreasing concentration profiles of counterions and thin marker layers at a distance of up to 130 nm from the surface. To introduce the characteristic features of the corresponding fluorescence signals, some intensity curves which are expected for these distributions are calculated and will be discussed in the following. Figure 2.10 shows some typical counterion signals which were calculated using the Gouy-Chapman model with varying Debye length. Simulations were done for an X-ray energy of 10 keV, here the minimal period of the XSW field $a_{\min}$ of ca. 20 nm is significantly larger than the vertical extension of the marker distribution. Correspond-

ingly, only the lowest XSW antinode overlaps with the ions and only one fluorescence maximum appears. Comparing the curves **a** - **d**, the relation between the extension of the diffuse ion layer (given by L_D) and the shape of the maximum in the related fluorescence signal is demonstrated. A scan of the distribution profile **a**, representing a highly compressed diffuse layer ($L_D = 1$ nm), leads to a very sharp fluorescence maximum, which is located at the critical angle. This is explained as follows: Only shortly before α_c, the antinode reaches the region of significant ion concentration, thus here the largest part of fluorescence is excited before reflectivity drops off. In the case of a broad ion distribution, as shown in the profile **d** ($L_D = 4$ nm), the wave overlaps at a given angle with a much higher marker concentration compared to case **a**. Thus, also the resulting fluorescence maximum is broader and its angle position slightly shifted towards smaller values.

Figure 2.10: Calculated examples of XSW-excited fluorescence intensity curves (left) with the corresponding marker distribution profiles (right). Curves **a** - **d** represent an exponentially decaying marker concentration, which is typical for counterion distributions. The curves were calculated for a Si substrate and 10 keV X-ray energy, the critical angle is marked by a dashed line.

Results like those shown in Figure 2.11 are expected for XSW scans of thin marker layers at a distance of several XSW field periods above the surface. Here, the fluorescence signal oscillates, which indicates the transition of XSW maxima through the layer. Each antinode of the field passing the layer generates one fluorescence maximum. Here, the distance between the reflecting surface and the marker layer is larger than the shortest possible oscillation period $a_{\min}$ of the standing waves field, so for m maxima before the

critical angle, the position of the layer can be estimated to $m \cdot a_{\min} \leq z < (m+1) \cdot a_{\min}$ (cf. equation 2.28). For the marker layer at a distance of 30 nm above the surface, two fluorescence maxima appear. A shift of the layer to $z = 70$ nm increases this number to four.
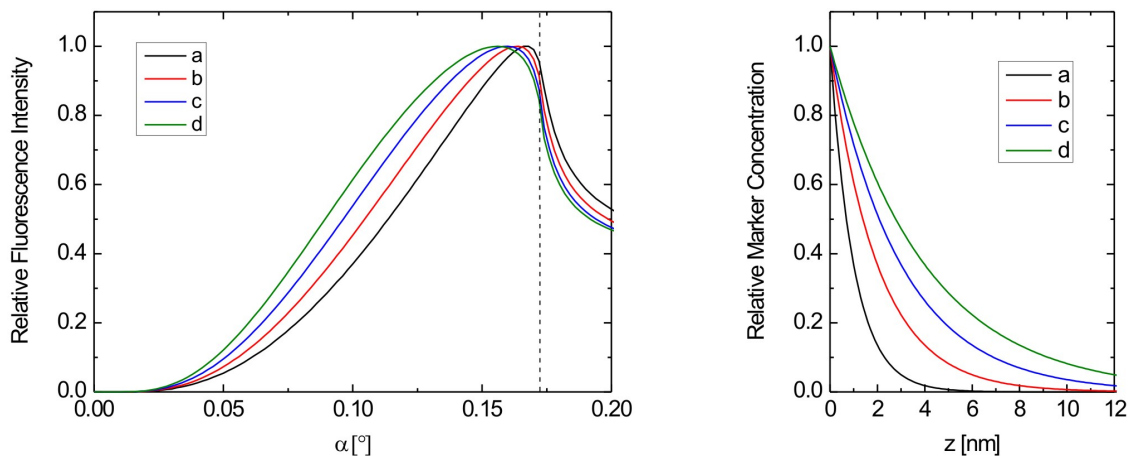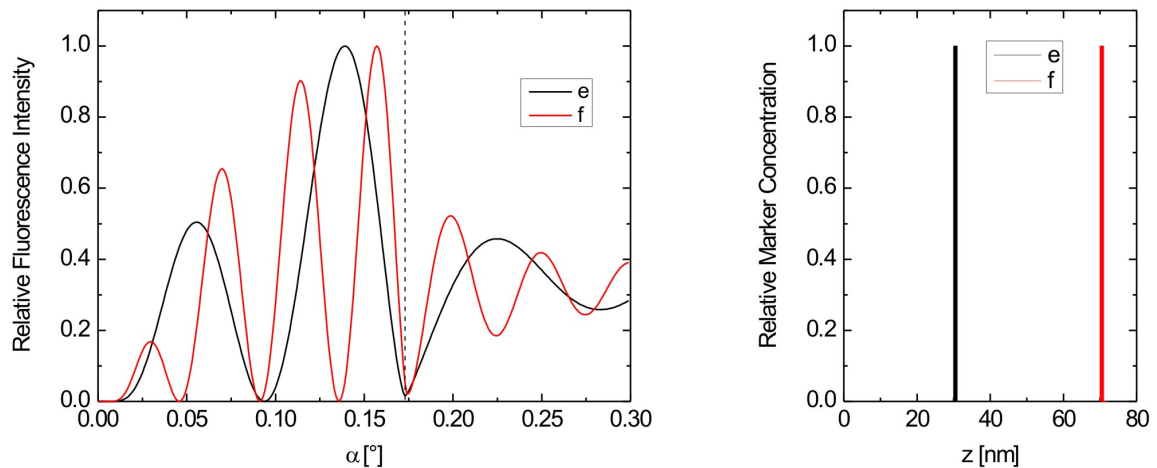

Figure 2.11: Calculated examples of XSW-excited fluorescence intensity curves (left) with the corresponding marker distribution profiles (right). The signal expected for a thin marker layer is plotted in the curves **e** and **f** for different layer positions. The curves were calculated for a Si substrate and 10 keV X-ray energy, the critical angle is marked by a dashed line.

Generally, it can be noticed that fluorescence detected near the critical angle originates from markers near the surface ($z < a_{\min}$), whereas markers far from the surface ($z \gg a_{\min}$) contribute to the signal measured at small angles ($\alpha < \alpha_c/2$).

For the evaluation of XSW-excited fluorescence signals, an intensity curve $I(\alpha)$ is calculated and fitted to the measured data. As mentioned above, the fluorescence intensity is the integrated product of the intensity of the XSW field $I(\alpha, z)$ and the element distribution $D(z)$. With the parameters of the sample (refractive indices of the components of the sample) and of the beam (wavelength, incident angle, critical angle), also the XSW field is known. From sample preparation, often a certain distribution of markers can be expected or, considering the criteria explained above, can be deduced from the measured signal. So, a first probable distribution profile $D(z)$ is proposed. Then, the simulation of the XSW-excited fluorescence signal according to equation 2.29 is calculated using the chosen distribution model. This simulation procedure is repeated, varying the parameters

of $D(z)$ in order to optimize the agreement between measured and calculated data. The model, for which optimal fit quality is achieved, can be regarded as representing the actual marker distribution at the interface of the analyzed sample.

2.3.6 Vertical Limitation of the XSW Field

As every experimental method, XSW scans have their limitations of applicability. The following discussion explains the restriction of the vertical range of measurement, which is already suggested by the upper integration limit z_{max} used in equation 2.29.

Until now, an ideal XSW field has been considered, where nodes and antinodes fill the entire intersection volume of incoming and reflected beam. However, in experiments it has been found that this does not match real conditions. This is mainly caused by the finite longitudinal coherence of the radiation which generates the field. Figure 2.12 demonstrates the realistic case, where the beams interfere only in the lower part of the overlap triangle. This effect has two main reasons: the longitudinal coherence length of the incident radiation is finite and the fraction of coherent radiation of the incoming beam is reduced by scattering processes inside the sample material. The longitudinal coherence length of an X-ray beam is defined as the distance, that two parallel wave trains starting from the same point have to propagate until their respective maxima and minima overlap [29]. Thus, the longitudinal coherence length ξ_l depends on the wavelength and the wavelength difference between the two wave trains $\Delta\lambda$ and is given by

$$\xi_l = \frac{\lambda}{2}\frac{\lambda}{\Delta\lambda}. \tag{2.31}$$

In practice, the longitudinal coherence length of the X-rays irradiating the sample is determined by the quality of the monochromator applied to the X-ray beam. A real monochromator emits a narrow bandwidth of wavelengths. The wavelength-dependent intensity distribution of the monochromatized beam is generally described by a normal distribution. The quality of a monochromator is defined by the full width at half maximum (FWHM) $\Delta\lambda$ of the intensity distribution. Typical values for single-crystal monochromators are $\Delta\lambda/\lambda \leq 10^{-4}$. The wavelength difference $\Delta\lambda$ induces a variation Δa of the field period given in equation 2.27. Thus, the nodes and antinodes of XSW fields generated by beams of different wavelengths are shifted vertically, which reduces the contrast of the interference field.

The effect of finite beam monochromaticity is significant at positions far from the
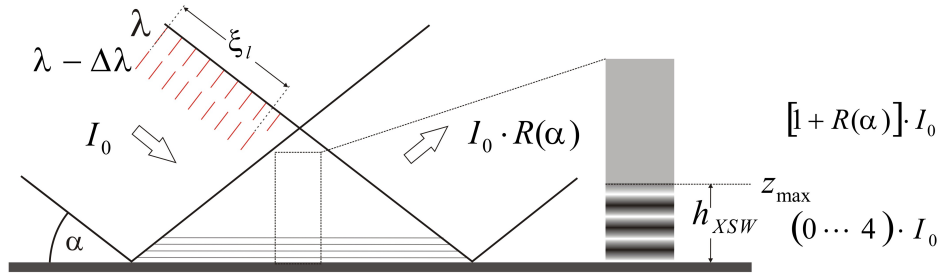
Figure 2.12: Vertical limitation of the XSW field caused by the finite coherence length of incident radiation. The dimensions are not shown in true scale.

interface and plays a role for media of very low electron density such as air or vacuum. It has been studied by von Bohlen et al. by XSW measurements of nanoparticles of up to 250 nm diameter on a silicon surface [44, 45]. From the comparison of measured and calculated fluorescence curves for particles of different size, it was observed that particles of a diameter of 100 nm and more were not any more completely irradiated by the field. From the deviation between calculated and experimental data, a vertical extension of the XSW field of $z \geq 83$ nm was deduced.

However, the finiteness of longitudinal coherence length cannot be not the only reason for the vertical limitation of the XSW field, as in experiments with solid/liquid interfaces very different values for z_{max} have been found for nearly identical combinations of X-ray energy and substrate material. Thus, it seems likely that also the solution containing the marker distribution has a great effect on the range of interference.

In experiments analyzing marker distributions embedded in liquid and polymer layers on the surface it has been observed that z_{max} of the best-fit distribution models decreases with increasing volume of the sample material covering the reflecting surface. Thus, the conclusion can be drawn that, for the transition of the beam through a medium of non-negligible electron density, the loss of coherence is mainly caused by scattering and absorption of incident photons. This can be understood using the example of an idealized case.

Considering a beam of originally coherent radiation, scattering and absorption processes reduce the fraction of coherent photons until all coherence is lost. For the cal-
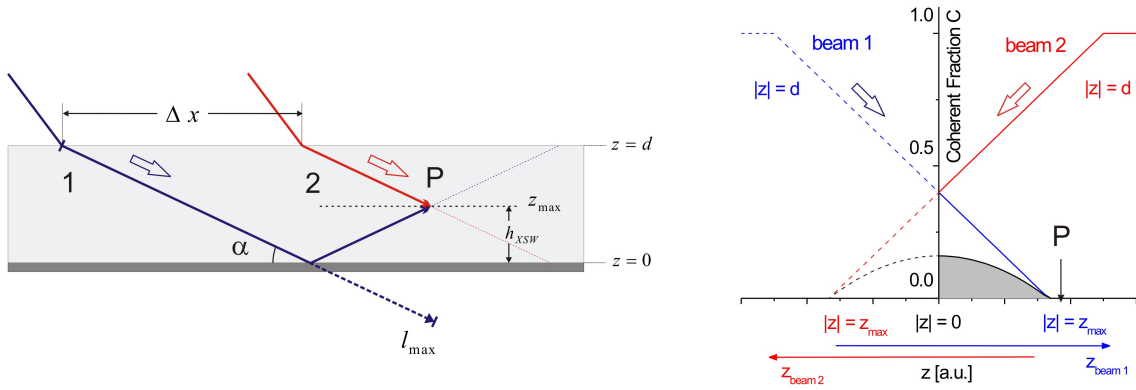
Figure 2.13: Principle of the vertical limitation of the XSW field due to a scattering-induced loss of coherence. For the two beams 1 and 2, interfering at the point **P**, a linear decrease of the coherent fraction is assumed. The maximal path length of coherent radiation l_{max} inside the medium determines the upper limit z_{max} of the interference range. Right: the fractions of coherent radiation C_1 and C_2 for the beams 1 and 2 are plotted as a function z. The shaded area indicates the relative intensity of interference, determined by the product of C_1 and C_2.

culation of h_{XSW} and the coherent fraction, the scattering and absorption properties of the respective sample must be known. For the general discussion of the effect, a simple linear decrease of the coherent photon fraction C is assumed. The geometry of the beam path is shown in Figure 2.13: The coherence of the incident beam 1, which passes a layer of thickness d is completely lost after a certain path length indicated l_{max}. The highest point, where the second beam 2 can interfere with beam 1 is marked P, its vertical position determines z_{max}. The vertical extension of the field h_{XSW} is given by

$$h_{XSW} = l_{max} \cdot \sin \alpha - d. \tag{2.32}$$

In the right part of Figure 2.13, the relative intensity of interfering (coherent) wave trains is plotted as a function of the distance z from the reflecting interface. The photons of beam 1 are moving towards the interface (blue dashed line) and reflected at $z = 0$. After reflection, the propagation direction is towards the sample surface at $z = d$ (solid line). Beam 2, hitting the the sample surface at a horizontal offset Δx, has a shorter path length (red solid line) to the point of interference P inside the medium. Consequently, the higher P is located, the more coherence is lost in beam 1 and preserved in beam 2. The product of C_1 and C_2 (marked grey), giving the relative intensity of the interference, is zero for $z > z_{max}$.

2.4 Infrared Spectroscopic Ellipsometry

A further experimental method which is used in combination with XSW experiments for the characterization of the properties of surface functionalizations is infrared spectroscopic ellipsometry (IRSE) [46, 47]. Figure 2.14 schematically shows the principle of ellipsometric measurements: Linearly polarized light is reflected at a surface. By the reflection, a phase shift Δ between the s- and p-polarized components is induced, thus the reflected radiation is polarized elliptically.
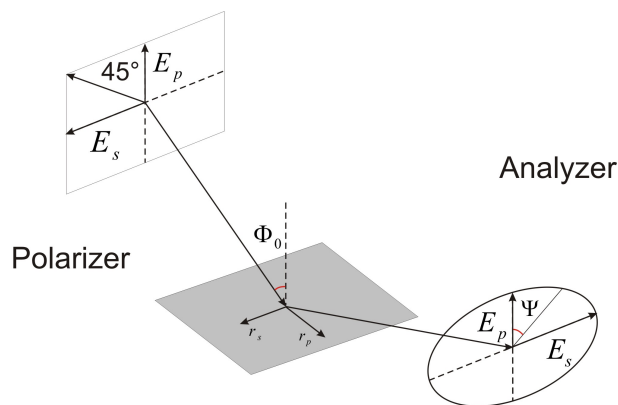
Figure 2.14: Principle of ellipsometry measurements.

The reflected radiation can be described by the amplitude ratio ρ of its (orthogonally polarized) components r_s and r_p

$$\rho = \frac{r_p}{r_s} = \tan \Psi e^{i\Delta}. \tag{2.33}$$

The absolute ratio of the amplitudes of the two components is given by

$$\tan \Psi = \frac{|r_p|}{|r_s|}. \tag{2.34}$$

Incoming infrared light excites different vibration modi of the chemical bonds in the surface molecules, which causes polarization-dependent absorption of the reflected radiation at characteristic wavenumbers, the so-called vibrational bands. By measurement of amplitude ratio of the two components of reflected intensity as function of the wavenumber ($\tan \Psi$ spectrum), these vibrational bands are detected, which enables the identification of chemical bonds and the state of surface molecules [48, 49]. In particular, the study of protonation and deprotonation processes of functional surface groups, changing the interfacial charge, is of interest for the present applications.

Summary of Chapter 2

In this chapter, the theoretical background of the experiments performed in the framework of this thesis was presented. First, some basic principles of the distribution of ions in the electric potential of a charged solid/liquid interface were introduced. The experimental methods for the measurement of the parameters characterizing the interfacial charge and potential were discussed, focusing on the X-ray standing waves field. The generation and the typical dimensions of the interference field, the evaluation of XSW-excited fluorescence signals and factors limiting the applicability of the method were explained. The experimental analysis of different types of ion distributions by standing waves will be presented in the following chapter.

Chapter 3

XSW Analyses of Solid/Liquid Interfaces

3.1 Experimental Setup

The typical components of the setup of XSW experiments are shown in Figure 3.1. For angular resolved XSW experiments, bright X-rays of high coherence and of low divergence are needed. To achieve this, synchrotron radiation is required. X-ray are generated, when charged particles (electrons or positrons) is accelerated in a magnetic field. This is done in the bending magnets, which are used to force the electrons into a circular orbit of the storage ring or in the so-called insertion devices, which are specially designed for this purpose. Common insertion devices are wigglers or undulators, consisting of a row of alternating magnetic fields. Electrons passing these devices follow a wavy trajectory, this successional acceleration of charges induces the emission of a cone of synchrotron light. Synchrotron radiation is emitted tangentially to the storage ring and led to the experimental stations by the so-called *beamlines*.

Any bending magnet and insertion device emits a continuous spectrum of radiation, so the wavelength of synchrotron radiation extends from the infrared to the hard X-ray range. At the so-called *critical energy*, the intensity of emitted radiation is near its maximum. As discussed in the previous chapter, XSW fields can only be produced using monochromatic radiation. For this purpose, the polychromatic ("white") beam is monochromatized, which in the hard X-ray range typically is done by double Bragg reflection at single crystals or at multilayer mirrors. The desired wavelength is selected by adjustment of the angle between mirror surface and the axis of the beam.

The photon energy used for the described experiments ranged between 10 and 17.48 keV. On adjusting beam energy, often a compromise has to be found between the respective advantages and disadvantages of marker excitation by high and by low energy. With X-rays of high energy, more elements can be excited to fluorescence. However, in the case of the beamlines where measurements have been carried out, the intensity of the beam is higher at lower energy values, which are nearer the critical energy. So, for example, at the SAW beamlines at DELTA ($E_{crit} = 7.9$ keV), the increase of energy of monochromatized radiation from 10 keV to 15 keV considerably reduces the brightness of the beam.
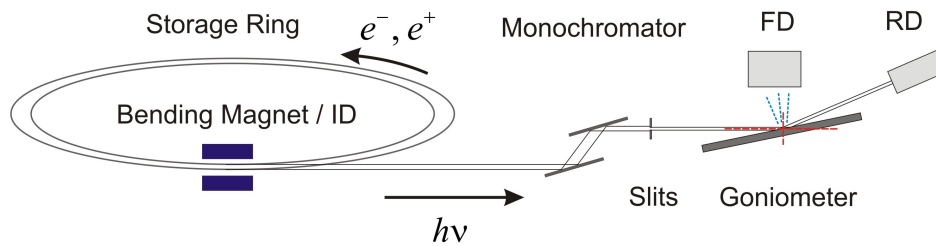
Figure 3.1: Principle of the experimental setup of XSW experiments. Radiation is generated by radial acceleration of electrons or positrons in the bending magnets or insertion devices (ID) of the storage ring. The X-ray beam is configured by the X-ray optics and irradiates the sample under grazing incidence. A goniometer is applied for the adjustment of the incident angle, a reflectivity detector (RD) records the intensity of the reflected beam. The position of the XSW field is marked by red lines. The fluorescence detector (FD) collects the photons excited in the XSW field (blue).

A system of slits confines the horizontal and vertical extension of the beam in order to limit the irradiated area (footprint of the beam) to the sample surface. The adjustment of the incident angle is done by rotation of the sample, which is placed on a goniometer capable of moving angular steps on the order of 0.001° with high repeatability.

Parallel to marker fluorescence, the intensity of the reflected beam is recorded, which is done in the present experiments using ionization chambers, scintillation counters and photodiodes. The measurement of reflectivity is applied to the exact positioning of the sample in the rotation center of the goniometer. Furthermore, reflectivity curves contain information about the structure of the sample, as for example roughness, evenness and the thickness of layers on the substrate.

The essential information of XSW experiments is the angular dependent intensity of fluorescence emitted from the marker atoms or ions. It is measured by a semiconductor detector which is mounted perpendicular to the sample. One spectrum is recorded per angle step. The use of this energy-dispersive detector type enables the element-sensitive measurement of fluorescence. The experimental procedure is controlled by a computer and consists of moving of the sample, recording reflectivity and fluorescence and processing the fluorescence signal via an MCA (Multichannel Analyzer). Table 3.1 summarizes the technical parameters and experimental settings of the beamlines employed for the measurements described in this work. Experiments were performed at the synchrotron radiation facilities DELTA (TU Dortmund, Germany) and BESSY II (Helmholtz-Zentrum Berlin für Materialien und Energie, Germany).

Beamline	BL9	BL8	BAMline
Synchrotron	DELTA		BESSY II
Beam Current [mA]	80 - 130		180 - 300
Insertion Device	SAW[1]		WLS[2]
Magnetic Field [T]	5.3		7
Crit. Energy [keV]	7.9		13.5
Monochromator	Si(311)	Si(111)	DMM[3] and Si(111)
Fluorescence Det.	Si-PIN	Si-PIN / SDD[4]	SDD
Reflectivity Det.	Scintillation counter	Ionization chamber	Photodiode
X-ray Energy [keV]	15.5	10 - 15	17.48
Angular Steps [°]	0.00125	0.001 - 0.00125	0.001
Beam Height [μm]	30	100	100

Table 3.1: Parameters of the beamlines used for the XSW experiments described in this work.

---

[1]Superconducting Asymmetric Wiggler
[2]Wavelength Shifter
[3]Double Multilayer Monochromator
[4]Silicon Drift Detector

3.2   Fluorescence Excitation Using Total X-ray Reflection

The grazing incidence geometry of XSW experiments involves particular advantages compared to classical X-ray fluorescence analysis (XRF). Under total reflection conditions, the incoming beam practically does not penetrate into the substrate carrying the sample, which causes an effective reduction of spectral noise and matrix effects. Furthermore, interference of incoming and reflected radiation significantly enhances the excitation of the sample atoms. This way, under optimal experimental conditions, a very low limit of detection (LOD) in the sub-nanogram range is achieved [16, 17].
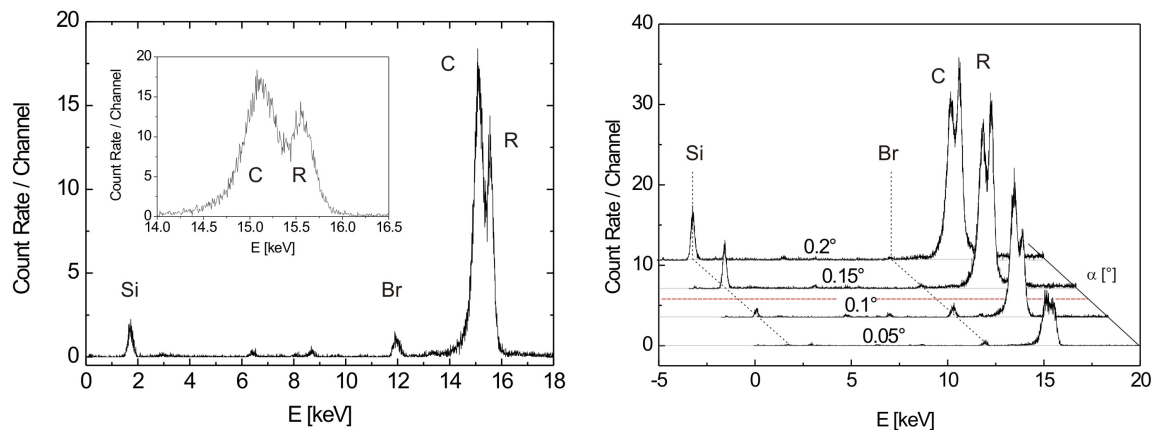
Figure 3.2: Left: Fluorescence spectrum excited under grazing incidence ($\alpha \approx \alpha_c$, $E = 15.5$ keV). The first peak (Si $K\alpha$ line) originates from the radiation penetrating into the substrate, the two peaks at the high-energy end of the spectrum (highlighted in the inset plot) are caused by scattering. Right: Development of signal intensity as function of the incident angle. The rise of scattering intensity, noise level and substrate fluorescence for $\alpha > \alpha_c$ can clearly be seen, whereas marker fluorescence vanishes. Only for $\alpha < \alpha_c$, the fluorescence marker peak (Br $K\alpha$) can clearly be separated from the spectral background . The red line indicates the position of the critical angle $\alpha_c = 0.12°$.

The typical properties of XSW-excited fluorescence signals will be discussed referring to the examples of Figure 3.2. The spectrum plotted on the left is recorded close to the critical angle, where reflectivity and with it the contrast of the XSW field begins to decrease. The marker element of the solution is bromine, the characteristic $K\alpha$ line

($E = 11.92$ keV) can easily be identified. The spectrum is recorded near the critical angle, thus fluorescence of the silicon substrate emerges (Si $K\alpha$, $E = 1.74$ keV), indicating a partial penetration of the beam into the substrate. The spectrum is dominated by the peaks of elastic (Rayleigh) and inelastic (Compton) scattering. In the right part of Figure 3.2, a series of successively recorded spectra from an XSW scan are plotted. The development of the fluorescence intensities of marker and substrate as well as Compton and Rayleigh scattering can be observed. Bromine again is the analyte, the signal is clearly separated from the background in the first two spectra. The rise of intensity indicates a maximum of bromine concentration at the reflecting interface. For $\alpha > \alpha_c$, the peak disappears in the spectral noise. The intensity of substrate fluorescence behaves inversely, the peak emerges at the end of the total-reflection range and remains at a constant level for $\alpha > \alpha_c$.

Scattering intensity strongly rises around the critical angle, whereas the Compton peak prevails for $\alpha < \alpha_c$ and Rayleigh intensity for $\alpha > \alpha_c$. The weak fluorescence lines between 6.4 and 8.6 keV ($K\alpha$ lines of Fe, Cu and Ni) are induced by the excitation of the material of the components of the experimental setup by scattered photons.

3.3 Functionalization by Surface Groups

The first samples analyzed in the framework of the presented studies are surfaces coated by functional groups. The purpose of this modification is the variation of the interfacial charge. The interfacial potential is analyzed by the measurement of the extension of the diffuse ion layer using X-ray standing waves. These experiments are done in combination with streaming current measurements. Besides the evaluation of fluorescence data, a discussion of the characterization of the structure of the liquid phase covering the surface with X-rays fluorescence and reflectivity is given, which is important for the correct interpretation of the measured curves.

In other studies, X-ray reflectivity has also been used to investigate the distribution of particles and charges near the solid/liquid interface [50, 51]. However, this technique is not element-sensitive and could therefore not be applied to the present task.

3.3.1 Sample Composition and Preparation

In these experiments, samples were silicon wafers modified by aminosilane surface groups. By means of this sample, the pH-dependent influence of a surface functionalization on

the charge and ζ-potential of the interface was studied [52]. Substrates were prepared by immersion of silicon wafers (size ca. 4 cm^2) in acetone solution containing 2-3% aminopropyl-triethoxysilane (APTS) for 10 minutes and subsequent toluene rinsing. In microfluidics, APTS is used to link other functional groups to an oxidized silicon surface [53], in the present experiment the amino group is applied to the modification of the surface charge. It is determined by the ratio of protonated amino groups (functionalization) and silanol groups (native silicon oxide layer) and given by the following equations:

$$\mathrm{NH_3^+ + H_2O \longleftrightarrow NH_2 + H_3O^+} \qquad \text{(a)}$$
$$\mathrm{SiOH + OH^- \longleftrightarrow SiO^- + H_2O.} \qquad \text{(b)}$$
$$\text{(3.1)}$$
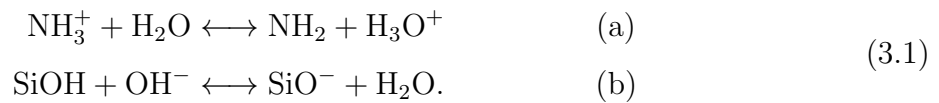
The liquid phase covering the wafers consisted of KBr and Fe(NO)$_3$ solutions of different pH values. Br$^-$ and Fe^{3+} ions were applied to the measurement of anion and cation distributions, respectively. The marker concentration was 10 mg/l in each case, the pH value determining the reaction equilibrium was adjusted by titration with HNO$_3$ and NaOH solution. Under acidic conditions, measurements were performed at pH 2.8 and 5.7, in the alkaline case at pH = 10.

Differing from XSW experiments with solid structures as particles or layer systems, in the case of the analysis of solid/liquid interfaces the problem of the stability of the sample during measurements arises. The strong scattering of X-rays in water allows an only very small volume of the liquid phase on the reflector, otherwise the high spectral background and the contribution of fluorescence originating from the unmodulated field would inhibit the identification of evaluation of the XSW-excited signal. Thus, only thin solution films can be used for the XSW analysis of ion distributions. Such films prepared on a substrate would evaporate very quickly in contact with air and have therefore to be encapsulated, which is commonly done by mylar or polypropylene foils of few μm thickness [19, 29]. However, the divergence of the incoming beam is increased during the transition through the foil. Especially at low incident angles ($\alpha < \alpha_c/2$), which are important for the characterization of the diffuse layer, absorption and broadening of the beam in the foil considerably affect the marker signal [60].

To avoid these problems, a different way of sample preparation has been chosen. A non-ionic surfactant (Tween-20) was added to the solutions, reducing the surface tension and preventing the evaporation of the liquid phase during measurement. The use of a surfactant enables the spreading of thin marker solution layers on the surface. The disruption of these layers produces sub-μm sized droplets, proving particularly favorable for XSW

experiments. This effect can be explained by the disintegration of a part of the surface groups in contact with aqueous solution. Disintegration of the functionalization is also observed in repeated streaming current measurements [54]. A more detailed discussion of the characterization of different types of the liquid phase and the respective advantages is given later.

Besides the identification of the respective distribution type and the polarity of the interface, the XSW experiments also allow the measurement of the Debye length L_D of counterion distributions. As discussed in section 2.1.2, this parameter allows the conclusion to the coverage and strength of the ζ-potential. Experiments were carried out at beamline 9 of the DELTA synchrotron radiation facility.

3.3.2   The ζ-Potential of APTS-functionalized Silicon Surface

Besides the Debye length of the ion distribution, the ζ-potential at the shear plane ψ_0 has to be determined for the calculation of the interfacial charge. For this purpose, the measurement of the streaming current was applied, using the SurPASS Electrokinetic Analyzer (Anton Paar). As schematically shown in Figure 2.2, a 1 mM KCl solution is pumped through a channel of two APTS-modified silicon wafers. The pH value of the solution was adjusted between 10.3 and 3.5 by titration with HCl and NaOH solution. From the measured streaming current, the potential at the shear plane is calculated automatically. The results for the functionalized and native silicon surface are given in the diagram shown in Figure 3.3. Its strength ranges from approximatively +70 mV at low pH to -100 mV in basic solution, the isoelectric point of the sample can be located at pH 6 - 7. The pH values 2.8 and 5.7 of the acidic solutions prepared for the XSW measurement of ion distributions correspond to a strong and a weak positive potential. Therefore, a different extension of the diffuse ion layer is expected in these cases.
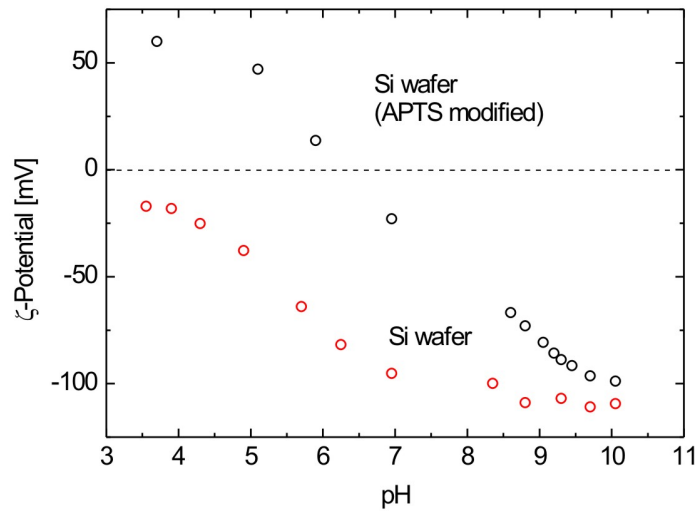
Figure 3.3: The ζ-potential of an APTS-functionalized (black) and a native (red) Si surface.

3.3.3 Correction of Scattering Influence

Previous to the discussion of the fluorescence data, some properties of solid/liquid interfaces influencing XSW measurements have to be considered. As mentioned in the introduction, scattered photons considerably contribute to the excitation of fluorescence intensity, which requires a correction of the measured marker count rate. Despite this rather unfavorable effect, the angular dependent scattering intensity yields useful information about the structure of the liquid covering the interface.

Figure 3.4 **a** shows an example for a scattering signal recorded during the XSW measurement of a solid/liquid sample. In the present case, a silicon surface covered by small droplets was irradiated by X-rays of $E = 15.5$ keV. Relative intensities of the Compton and Rayleigh peak are plotted together with the spectral noise measured at 10 keV. In the diagram, two intensity steps of different extent can be observed at $\alpha \approx 0.08°$ and at $\alpha \approx 0.12°$. At the given energy, these values correspond to the critical angles of the air/water and the air/silicon interface, respectively. Regarding the Compton signal, the first step is particularly significant, whereas at the second step only a moderate intensity rise is observed. Rayleigh intensity behaves inversely. Here, the major increase of the count rate occurs at $\alpha = 0.12°$. From these intensity distributions, the following conclusions can be drawn: Compton scattering mainly occurs within the liquid phase; while

most elastic scattering takes place in the silicon substrate. This result corresponds to the Z-dependency of the ratio of Compton and Rayleigh intensity described by Johnson and Stout [55]. For light elements, Compton scattering prevails and with rising atomic number, more elastic scattering is produced. Therefore, Compton intensity has been chosen for the normalization of the fluorescence signal [56].
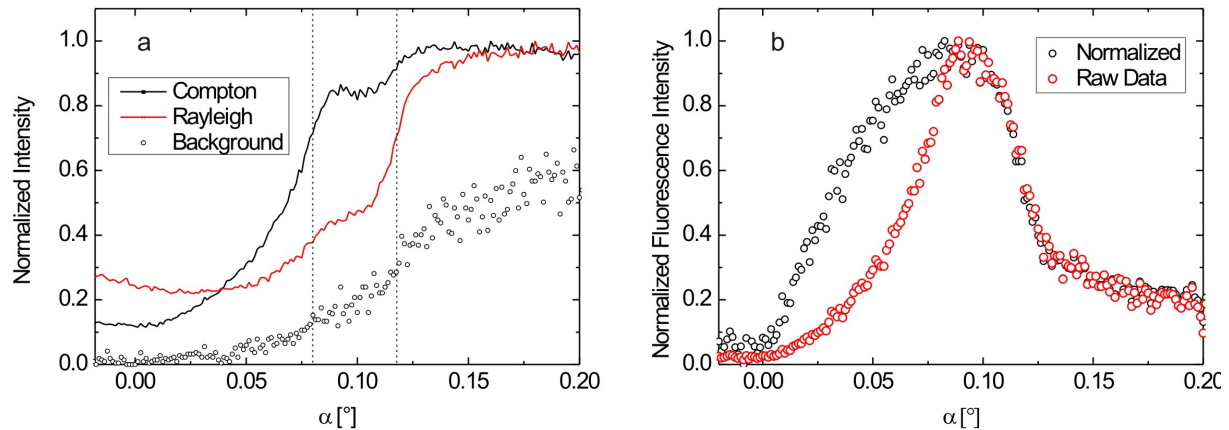
Figure 3.4: Plot **a**: Angular dependent intensity of inelastic and elastic X-ray scattering at a Si/water interface. Compton scattering mainly occurs inside the liquid phase (nearly the maximum level is reached at $\alpha_c = 0.08°$(air/water)), whereas the heavier Si substrate atoms induce the major part of elastic Rayleigh scattering (large step at $\alpha_c = 0.12°$(Si/air)). The circles mark the relative level of the spectral background intensity, in this case recorded at $E = 10$ keV. In diagram **b**, the effect of scattering normalization on the marker fluorescence signal is shown.

3.3.4 The Structure of the Liquid Phase

Water is a medium of high scattering power as it consists of solely light elements [57]. Therefore, it is favorable to keep the volume of the liquid phase covering the substrate as small as possible in order to reduce the scattering-induced noise level. In the experiments, this was achieved by the addition of a surfactant to the solution. Depending on surfactant concentration, surface hydrophilicity and air moisture, the formation of different liquid structures is possible. From X-ray fluorescence and scattering signals, two different types of structures could be identified: Thin films and micelle-like droplets. For the evaluation

of the marker fluorescence, the calculation of the intensity distribution of the XSW field has to be adapted to the respective case. In the following, the identification of these structures and their influence on the fluorescence signal will be discussed.
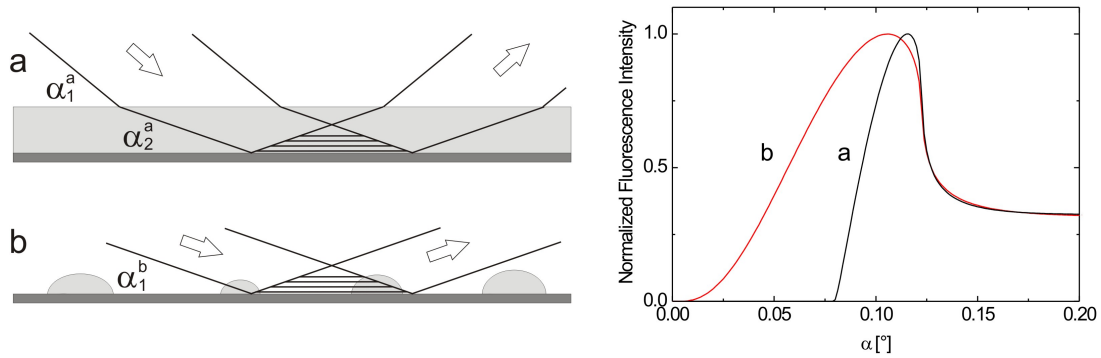

Figure 3.5: Beam path for different structures of the liquid phase. In case **a**, the solution forms a thin layer with a plane interface between water and air, refracting the incident beam. in case **b**, the surface is covered by droplets, here the beam enters the liquid phase without being refracted. The resulting signals are plotted on the right show the example of an XSW scan of a counterion distribution.

Liquid Layers and Droplets

Figure 3.5 schematically shows the reflection of an X-ray beam at a surface covered by a layer (**a**) and droplets (**b**) as well as the corresponding fluorescence signal expected for a counterion distribution. The X-ray energy of calculated and experimental data discussed in this section is 15.5 keV. The incides 1 and 2 mark the incident angle before and after refraction at the air/solution interface, respectively. In the case **a**, all radiation is reflected at the air/water interface for $\alpha < \alpha_{c1}^a = 0.08°$, consequently no ion fluorescence is excited. For greater angles, the beam is refracted into the solution layer under a new incident angle α_2^a. The critical angle of the water/silicon interface is determined by the electron density difference between water and silicon and is given by $\alpha_{c2}^a = \sqrt{2(\delta_{\text{Si}} - \delta_{\text{water}})}$. Under the given experimental conditions, the critical angle α_{c2}^a corresponds to an incident angle $\alpha_1^a = 0.12°$. Excitation of marker fluorescence occurs for $\alpha_{c1}^a < \alpha_2^a < \alpha_{c2}^a$ (plotted black).

In case **b**, radiation enters the solution through the curved surfaces of the droplets.
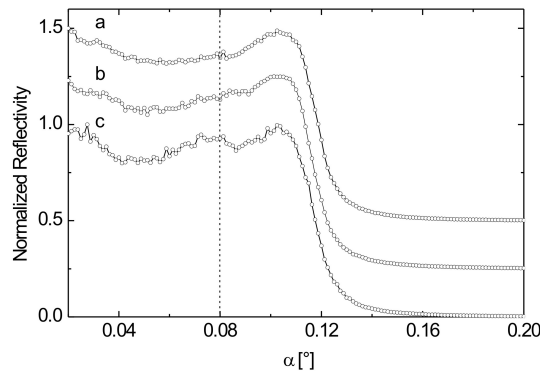
Figure 3.6: Reflectivity curves of surfaces covered by a liquid in the form of droplets (**a**, **b**) and thin layers (**c**). The layer can be identified at the decrease of reflectivity at $\alpha = 0.08°$, the critical angle of the air/water interface at 15.5 keV. In curve **b**, no such feature is detected, which indicates a non-grazing entrance of the beam into the solution over the entire angular range. In measurement **a**, only a minimal variation of intensity is visible, probably induced by some remains of a layer.

Due to the low dispersion of hard X-rays in matter, refraction can be neglected for incident angles greater than ca. 0.5°, therefore these surfaces can be treated like being perpendicular to the beam path. Here, the resulting angular range of fluorescence excitation extends from $\alpha_1^b = 0°$ to $\alpha_{c1}^b = 0.12°$, the critical angle of the air/silicon interface (red curve).

Experimental evidence for the two types of liquid phase structure is given by the measurements shown in Figures 3.6 and 3.7. In Figure 3.6, reflectivity curves of a silicon surface covered by droplets (**a, b**) and a liquid film (**c**) are plotted. The distinguishing feature of the two cases is the intensity step at $\alpha = 0.08°$, the critical angle of the air/water interface. This step is nearly non-existent in the curves **a** and **b**, where the beam enters the droplets without being refracted, but is clearly visible in case **c**, where refraction at the liquid surface occurs. For all samples, the main reflectivity decrease is at $\alpha = 0.12°$, the critical angle of silicon. This indicates that in all samples only a small fraction of the surface is covered by the solution.

Under certain conditions, not only the position of the critical angles but also the fluorescence signal itself gives information about thin liquid structures. Figure 3.7 shows a comparison of the fluorescence signals from markers inside a film (**a, b**) and of droplets

or particles (**c, d**). Thin layers of parallel surfaces can act as waveguide structures, where the excitation of transverse electric (TE) modes induces an angle-dependent oscillation of the Compton scattering signal, which itself contributes to marker fluorescence excitation [58, 43]. This effect, which will be discussed in more detail in section 4.1.2, is very obvious in the fluorescence signal of markers in a polymer layer (**a**), but can also be detected in a sufficiently even liquid film (**b**). A disintegration of such layers, caused by evaporation and disruption of the surfactant film, creates droplets of comparable dimensions. The signals plotted in the right part of Figure 3.7 are recorded from nanoparticles of 50 nm diameter (**c**) and a co-ion distribution (**d**). Although this signal is strongly noise-affected, the two curves show similar general characteristics, indicating the presence of droplets comparable to liquid nanoparticles in case **d**. The diameter of the droplets should be at least $3L_D$ to exclude the influence of effects related to the air/solution interface on the ζ-potential [59]. This condition is fulfilled for all experiments discussed in the following.
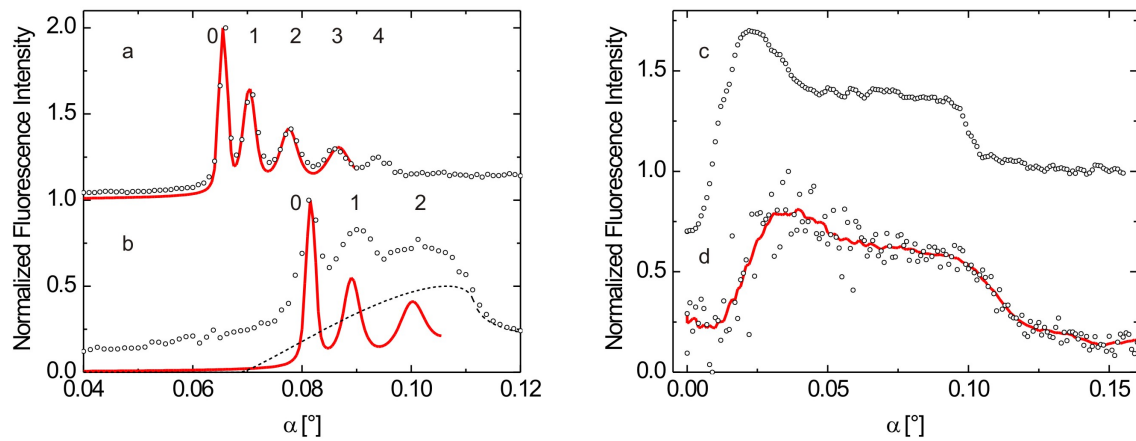
Figure 3.7: Fluorescence of marker distributions from samples of layer (**a**, **b**) and particle (**c**, **d**) shape. Curve **a** shows the signal of a homogeneous Br distribution inside a polymer layer of 127 ± 2 nm thickness. Fluorescence is excited by the transverse electric field nodes TE_n ($n = 0 - 4$). The same resonance effect is detected in the case of the liquid layer (**b**), in this case with the XSW-excited signal of a counterion distribution superimposed (dashed line). From the oscillation period, a layer thickness of 100 ± 10 nm can be derived. Graph **c** shows the XSW-excited fluorescence of Au nanoparticles on a Si substrate (diameter: 50 nm). The shape of this curve corresponds to the intensity of a co-ion Fe^{3+} distribution inside droplets plotted in **d** (red line: Average signal).

Liquid films prove disadvantageous in the case of insufficient evenness of the air/solution interface. Here, the refraction of incoming X-rays causes divergence of the beam transmitted into the liquid, which leads to a blurring of node/antinode contrast of the XSW field. In the case of droplet-covered surfaces, a too large droplet size (μm range) has to be avoided since this increases scattering and the vertical extension of the XSW field is reduced.

Previous to the evaluation of marker fluorescence data, the sample structure was identified through the criteria described above. In the first series of ion distribution measurements, only samples of the droplet type were used for ion distribution analysis. Here, a clearly defined reflection and refraction geometry can be assumed.

Plots of the XSW Scans: General Remarks

In the figures presenting the results, circles indicate the measured fluorescence signal and the red curve the corresponding simulation. Besides the signal of the respective marker element, the fluorescence intensity of the silicon substrate is included in the diagram (gray line, normalized to the maximum of marker fluorescence). The fluorescence of the substrate material gives information about the quality of the applied substrate: An abrupt rise of silicon count rate at the critical angle is typical for smooth and planar surfaces (as shown in Figure 3.8), whereas a less steep intensity rise indicates a bent or rough substrate (see Figure 4.9).

For the evaluation of the XSW scans, a good agreement of measurement and simulation is required in the total reflection domain, particularly in the angular range of $\alpha_c/2 < \alpha \leq \alpha_c$, where optimal conditions for XSW-enhanced fluorescence excitation prevail. At smaller angles, the influence of sample properties which complicates the evaluation of the signal generally is largest, thus in this angular range fit quality is lowered by a strong scattering of data points or discrepancies between measurement and calculation. The origin of these effects will be explained in more detail in the respective discussions of the scans.

Beyond the critical angle the spectral background significantly rises, whereas the amplification of fluorescence excitation through the interference of incident and reflected beam ends. Thus, for $\alpha \gg \alpha_c$ the fluorescence peak of the analyte can not be separated properly from the spectral noise, which also causes a discrepancy between measured and calculated signals. However, this effect does not impair data analysis, as the signal in the total reflection range contains all relevant information about the marker distribution.

3.4   Ion Distributions in Droplets

Figures 3.8 and 3.10 show the fluorescence intensity measured from bromine and iron containing solutions in contact with APTS-modified silicon wafers.

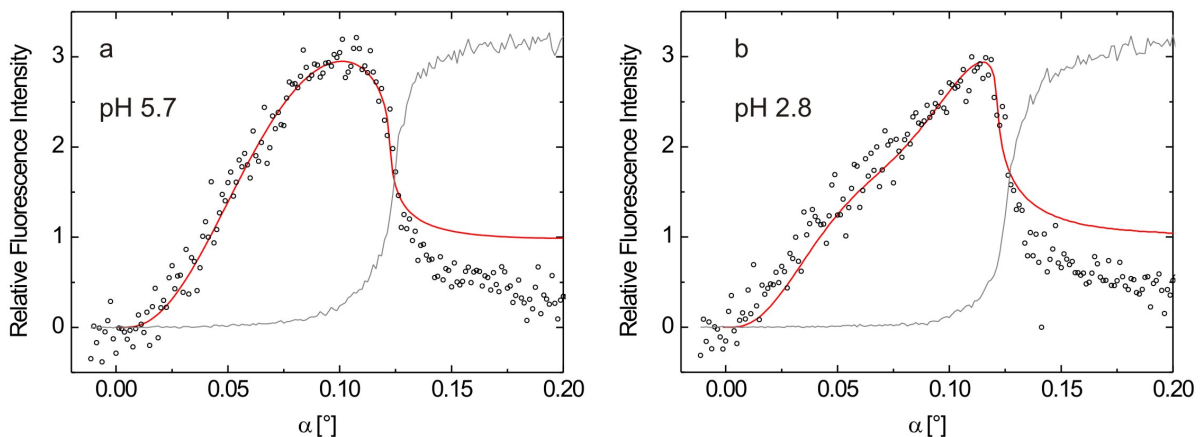### 3.4.1   Counterion Distributions

Figure 3.8: XSW-excited Br$^-$ fluorescence (circles) above an APTS-functionalized Si surface for pH 5.7 (left) and 2.8 (right). The best fit simulation curve (red line) was calculated applying the distribution models plotted in the left part of Figure 3.9. The inflection point of Si fluorescence (gray line, intensity scaled to Br signal) indicates the position of the critical angle.

First, the results of bromine fluorescence measurements will be discussed. The curves exhibit typical features of counterion signals. Characteristic features are an intensity rise up to a maximum near the critical angle, followed by an abrupt decrease of intensity and a constant count rate for $\alpha > \alpha_c$. At very small angles ($\alpha \leq 0.02°$) the detected fluorescence signal is very weak compared to the spectral background, so the subtraction of background and normalization of Compton influence lead to noise in the signal. For $\alpha > 0.02°$, a good agreement of measurement and simulation is observed. The best-fit distribution models corresponding to these signals are shown in Figure 3.9 **a**, the experimental parameters and results are given in Table 3.2. Both signals are simulated applying counterion distributions including an exponentially decreasing marker concentration.

The most important features distinguishing the two curves of Figure 3.8 are the shape and the angular position of the fluorescence maxima. In the measurement performed at pH

5.7 a broad fluorescence maximum is observed at $\alpha = 0.1°$, whereas the signal recorded at pH 2.8 features a significantly sharper maximum at $\alpha = 0.12°$, which indicates a smaller extension of the diffuse ion layer. Based on the discussion in section 2.3.5, the Debye length found for the Br^- distribution at pH 2.8 is roughly half the value of the pH 5.7 case. The position of the fluorescence maximum detected at pH 2.8 is equal to the critical angle, which indicates the existence of an adsorbed layer. The best fit of this signal is obtained by the Stern model, whereas the distribution profile applied to the simulation of the pH 5.7 curve only consists of the diffuse layer proposed by the Gouy-Chapman model.

The results of the distribution scans using XSW are confirmed by the streaming current measurement of the ζ-potential ψ_0 (Figure 3.3). A pH value of 5.7 corresponds to a relatively weak potential and a broad diffuse layer. At pH 2.8, the strong potential immobilizes ions at the interface and compresses the diffuse layer. This compression is sufficient to shield the interfacial potential within the range of the XSW field ($z_{const} < z_{max}$), so that also the bulk ions are detected. As the bulk concentration C_0 is known from sample preparation, the concentration $C(z)$ of the diffuse layer can be determined. From the diagram of Figure 3.9 **a**, the concentration of mobile ions at the shear plane can be estimated to 30 mg/l. The density of ions in the adsorbed layer is roughly three times higher. Similar to the calculation of Wang et al. [60], for ions of diameter of 0.39 nm a coverage of $3 \cdot 10^{11}$ ions/cm² can be assumed. Combining the results of XSW and streaming current measurements, the interfacial charge is calculated using the Grahame equation. The results of this are given in Table 3.2.

Regarding the near-interface volume of the solution, an interesting effect is observed: Between the surface and the maximum of the ion concentration a marker-free space exists, inhibiting the direct contact of substrate and solution. The extension d of this gap is 1.0 ± 0.2 nm in the pH 5.7 solution and 0.6 ± 0.2 nm in pH 2.8 case. These values are in good agreement with the length of the aminosilane functionalization molecule of 0.7 nm.

3.4.2 Co-ion Distributions

The most obvious difference between the Fe^{3+} co-ion distribution and the previous measurements is found in the fluorescence signal from the pH 2.8 solution shown in Figure 3.10 **a**. This scan shows the typical features of a co-ion signal, the intensity rises to a maximum at $\alpha = 0.05°$ where the first (lowest) XSW antinode (intensity maximum) illuminates the ions far from the interface (ca. $z \geq 15$ nm). A further increase of the incident angle moves this maximum downwards into the near-interface region, where the
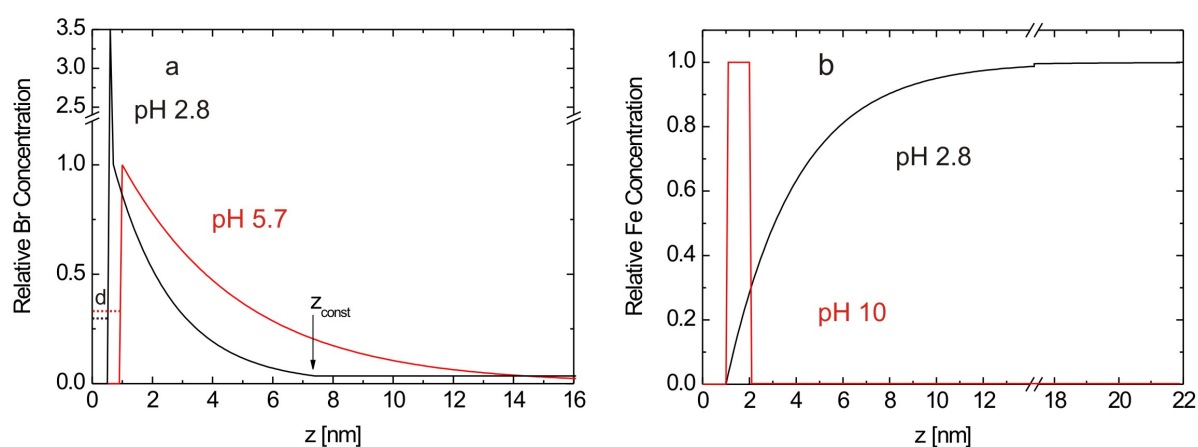
Figure 3.9: Ion distribution models applied to the simulation of XSW-excited marker fluorescence intensity. The best-fit simulation of Br and Fe fluorescence signals is achieved with the shown concentration profiles. Plot **a**: Counterion Br^- distribution over APTS-modified Si measured at pH 5.7 (red, diffuse layer) and 2.8 (black, adsorbed and diffuse layer). The transition from an exponentially decreasing to a constant ion concentration in the pH 2.8 distribution is indicated z_{const}. Plot **b**: Co-ionic Fe^{3+} distribution in the sample prepared at pH 2.8 (black) and $Fe(OH)_3$ precipitate in the pH 10 solution (red).

marker concentration is lower, which causes a decrease of fluorescence intensity. Under the present experimental conditions, the extension of the XSW field is limited to only two intensity maxima. The second antinode of the XSW field appears at $\alpha \approx 0.12°$. However, this excitation is too weak to produce a distinct fluorescence maximum.
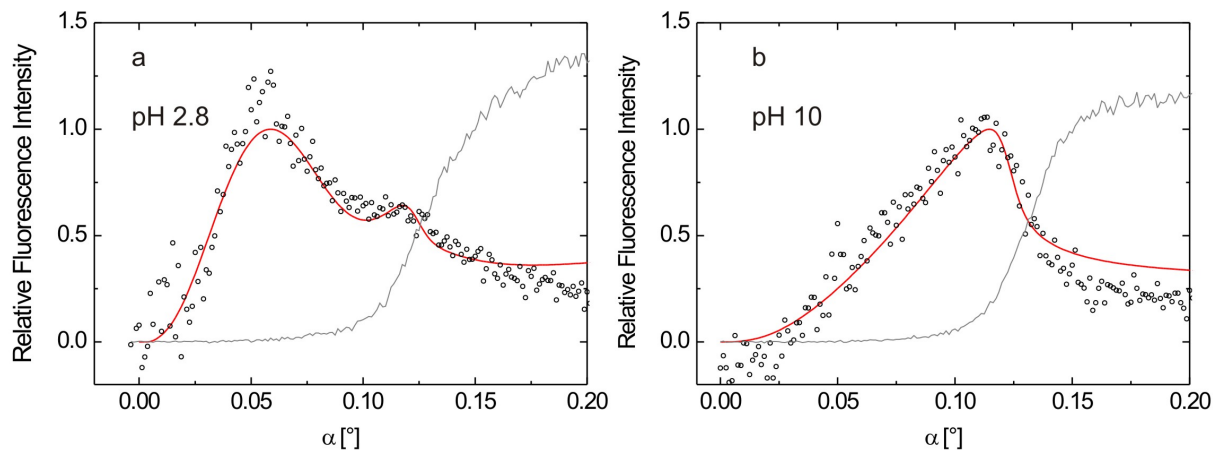
Figure 3.10: Fluorescence measured from $Fe(NO)_3$ solution in contact with an APTS-functionalized Si surface. The left plot, measured at pH 2.8, shows the typical signal of a co-ion distribution. In the pH 10 solution (XSW scan shown on the right), Fe^{3+} ions have precipitated to $Fe(OH)_3$, forming a thin layer on the substrate. This effect results in the signal of a Helmholtz-like distribution, featuring a sharp intensity maximum at the critical angle.

As in the previous case, the results from XSW measurements agree with streaming current measurement of ψ_0. The co-ion character of the Fe^{3+} distribution at pH 2.8 corresponds to the repulsion of cations by the positive ζ-potential. A more detailed quantitative analysis of co-ion distributions is not possible for several reasons:

- Most fluorescence photons are excited at small angles ($\alpha \approx 0.05°$), where the beam path inside the liquid phase is longest. As discussed in the introduction, this geometry implies a high scattering-induced noise level.

- Unlike counterion distributions, the detectable marker concentration remains largely constant over the vertical measuring range ($z < z_{max}$). A significant variation of marker concentration only occurs in the vicinity of the interface. Thus, most ions of the distribution are not affected by the ζ-potential.

- The ideal condition for an XSW scan is the overlap of only one antinode with the marker distribution. In this case, an unambiguous correlation between marker position and angular fluorescence distribution exists. This condition is not any more fulfilled in the present case, where the fluorescence signal is excited by two antinodes of different intensity.

Concerning the $Fe(NO)_3$ solution at pH 10, the marker fluorescence signal shows similarities to the Br^- distribution at pH 2.8. However, unlike this measurement, where the XSW scan of the diffuse ion layer caused a non-linear intensity rise, no evidence for such distribution feature of larger extension is found in the Fe signal. Thus, an accumulation of all detectable markers at the interface is expected, which is confirmed by the best-fit distribution model shown in Figure 3.9 **b**. The existence of this layer is explained by the precipitation of Fe^{3+}, forming a thin $Fe(OH)_3$ layer on the substrate, an effect which is also of relevance for biological surfaces [61].

Additional to the discussion and interpretation of fluorescence data, an estimation of the accuracy of the experimental method can be obtained from these measurements. For this purpose, the simulation of the signals shown in Figures 3.8 **a** and 3.10 **b** was done using distribution models without the marker-free gap of $d = 1$ nm at the interface. As shown in Figure 3.11 the simulations calculated with the modified distribution profiles (green) significantly deviate from the original simulations (plotted red). Therefore, for both counterions and Helmholtz-like distributions, the upper limit of accuracy of the fit method can be estimated to ≈ 1 nm.

Marker	Charge	pH	ψ_0 [mV]	L_D [nm]	d [nm]	σ[mC/m^2]
Br	1-	2.8	$+70 \pm 10$	2.0 ± 0.5	0.6 ± 0.2	$+4.7 \pm 0.5$
Br	1-	5.7	$+25 \pm 8$	3.9 ± 0.2	1 ± 0.2	$+33 \pm 8$
Fe	3+	2.8	$+70 \pm 10$	-	-	-
Fe	0	10	-100 ± 5^a	-	1 ± 0.2	-

Table 3.2: Experimental and simulation parameters for the XSW measurements of the ion distribution over APTS-functionalized silicon. ^{a}Here, ψ_0 is not relevant for the marker distribution.
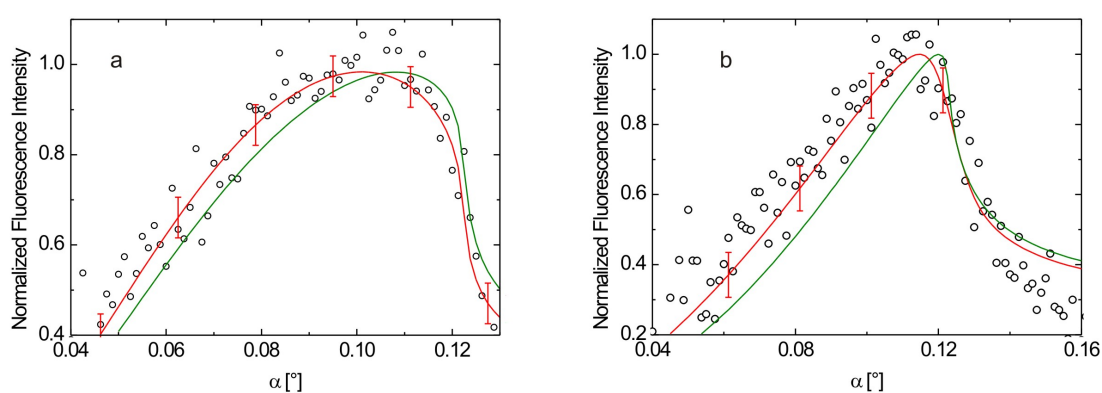
Figure 3.11: Estimation of the accuracy of XSW measurements by variation of the fit model. The plots show the intensity maxima of the fluorescence signals obtained from the Br^- solution at pH 5.7 (Figure 3.8 **a**) and the $Fe(OH)_3$ layer at pH 10 (Figure 3.10 **b**). The original simulation functions are plotted red, the error bars indicate the average deviation of measured data from the fit. The fraction of data points within the margin of error is 61% in case **a** and 57% for **b**. The curves plotted green were calculated using the distribution model with the same parameters as before, only the ion-free space at the interface is omitted. The effect of this modification is clearly visible.

3.5 Ion Distributions in Liquid Layers

3.5.1 Sample Preparation and Experiments

The effect of APTS modification of a silicon surface is shown in Figure 3.3. The charge of (protonated) amino groups shifts the surface charge towards positive values, even changing its polarity in acidic solutions. Therefore, the next step of the characterization of the functionalized surface is the measurement of the interfacial charge over a larger pH range including the isoelectric point [62]. A modified procedure of sample preparation was used than that described in section 3.3.1: APTS was dissolved in toluene instead of acetone and wafers were dried for 15 minutes at 100°C after immersing. This resulted in a more stable coating, thus for these surfaces no disruption of the solution films was observed. Instead, the occurrence of two critical angles α_c^{sol} and α_c^{sub}, seen in Figure 3.5 **b**, evidences the formation of a thin liquid layer, as discussed in section 3.3.4.

Again, Br^- was chosen as marker anion. For the measurement of cation distributions, Fe^{3+} was replaced by Rb^+ to avoid precipitation. The marker concentration was 25 mg/l in each solution. For the adjustment of the pH, HNO_3 and NaOH solution were used. At neutral pH, the low free surface energy of the uncharged interface inhibited the preparation of a liquid film [63]. Experiments were performed at the BESSY II synchrotron radiation facility (BAMline).

3.5.2 Optical Properties of Liquid Layers

An advantage of the liquid layer is the constant level of scattering intensity in the angular range of total reflection at the solid/liquid interface ($\alpha_c^{sol} < \alpha < \alpha_c^{sub}$). Therefore, here no correction of scattering influence is necessary. However, beam quality generally decreases inside the liquid layers. As shown in Figure 3.12, the surface of the real solution film is not perfectly flat but undulating. The resulting divergence of the refracted beam reduces the contrast between the maxima and minima of the XSW field, leading to an angular broadening of the fluorescence signal. This was also observed in other XSW experiments, where the liquid phase was covered by a thin polypropylene foil [28].
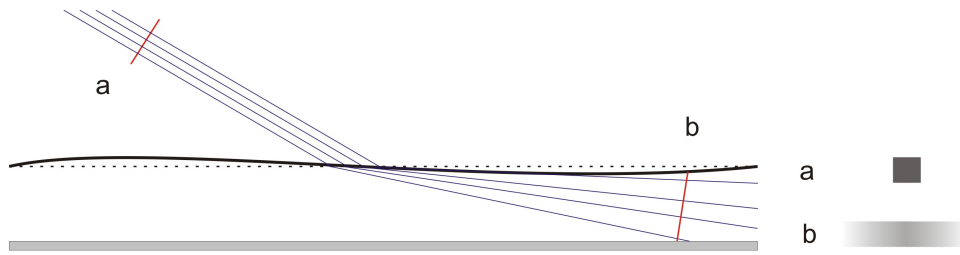
Figure 3.12: Left: Beam divergence induced by refraction of X-rays at an undulated inter-face. Right: Schematical cross section of the lateral intensity distribution before (**a**) and after refraction (**b**).

3.5.3 Analysis of Substrate Fluorescence

The beam divergence induced by surface undulation complicates data evaluation for two reasons:

- The exact localization of the fluorescence maximum is difficult due to the broadening of the signal. However, the identification of the angular position of the maximum is important for the correct adjustment of the fit parameters L_D and d (compare the differences of the curves plotted in Figure 2.10 and Figure 3.11).

- In the simulation process, the reduction of the contrast of the XSW field has to be taken into account. This was done by the convolution of the simulated signal with a Gaussian distribution of variance σ_{conv}, which is different for each sample [28]. This introduces an additional free parameter which has to be determined and reduces the unambiguousness of the fit.

One approach to deal with these problems is the evaluation of the angular dependence of substrate fluorescence intensity. Under certain conditions, this enables to fix the convolution variance precisely. Such a case of (silicon) substrate fluorescence is shown in Figure 3.13 **a**, the determination of σ_{conv} is described in the following. Assuming an ideally flat surface, a non-divergent beam and a detection area smaller than the footprint of the beam, substrate fluorescence will only emerge at α_c, where the transmission angle takes real values, as discussed in section 2.3.2. For $\alpha > \alpha_c$, radiation penetrates into the
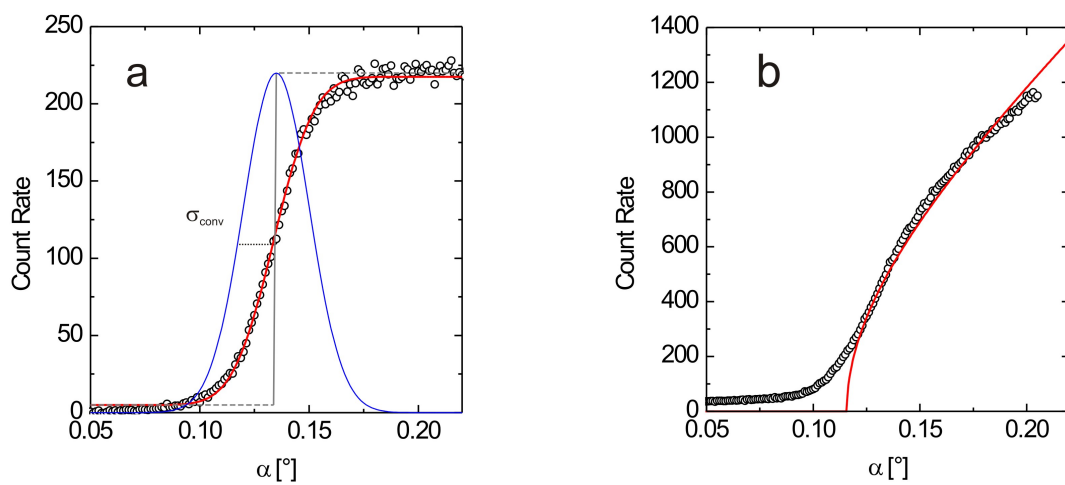
Figure 3.13: Examples for substrate fluorescence signals which are adequate (**a**) and inappropriate (**b**) to the determination of the variance σ_{conv} of the Gaussian distribution used for the convolution of marker fluorescence. Fluorescence curves **a** and **b** were measured using Si wafers and an X-ray energy of 15 and 15.5 keV, respectively. The best fit of curve **a** is obtained by a step function convolved with a Gaussian distribution of variance $\sigma_{conv} = 0.015°$ (blue). The fit applied to curve **b** is the real part p_+ of the transmission angle.

substrate, exciting silicon fluorescence. Due to absorption of fluorescence photons and the grazing incidence of the beam, fluorescent emission is detected only from a sample depth of few μm. Therefore, for $\alpha > \alpha_c$ silicon fluorescence intensity does not depend on the incident angle and remains constant. In this idealized case, the silicon signal is described as a step function, which then is convolved with a Gaussian distribution and compared to measured data. The variance σ_{conv} of this convolution function, for which optimal agreement between measured and calculated substrate fluorescence is achieved, is also applied to the convolution of marker fluorescence, as signals from both marker and substrate are affected likewise by beam divergence. Furthermore, as the value of α_c^{sub} is known from the experimental parameters, a possible inaccuracy of sample adjustment, leading to an angular shift of the curve, can be corrected.

These considerations are only valid for substrate fluorescence curves reaching a constant level of intensitiy shortly after the critical angle, as shown in Figure 3.13 **a**. Signals as shown in plot **b** of this Figure cannot by used for the determination of the convolution parameter, as here the inflection point of substrate fluorescence intensity cannot clearly be identified. Instead of a step function, these curves are similar to the real part of the transmission angle.

3.5.4 The pH-Dependent Interfacial Charge of Si/APTS

Examples for a co- and a counterion signal are shown in Figure 3.14. The effect of the reduction of XSW field contrast induced by beam divergence is obvious on comparison of the data from a film (Figure 3.14) and from droplets (Figures 3.8/3.10). In terms of sharpness of the intensity maxima and the signal/noise ratio, data from liquid layer samples do not reach the quality of the signal recorded from droplets. Therefore, an evaluation of the shape of the fluorescence signal is not sufficient for an unambiguous identification of the ion distribution. The main difference between the two distribution types is the angle position of the fluorescence maximum $\Delta\alpha$.

The fluorescence signal of the silicon substrate is fitted by a Gaussian-smoothed step function (example **b** of Figure 3.13). From this fit, values of variance σ_{conv} are obtained, which are necessary for the convolution of marker fluorescence simulation and allow the determination of the absolute angular position.

The results of the measurements performed within a pH range of 2.2 to 9 are shown in Figure 3.15. The interfacial charge was calculated from the parameters L_D and ψ_0; the change of polarity at the isoelectric point between pH 5 and pH 7 is clearly observed. The
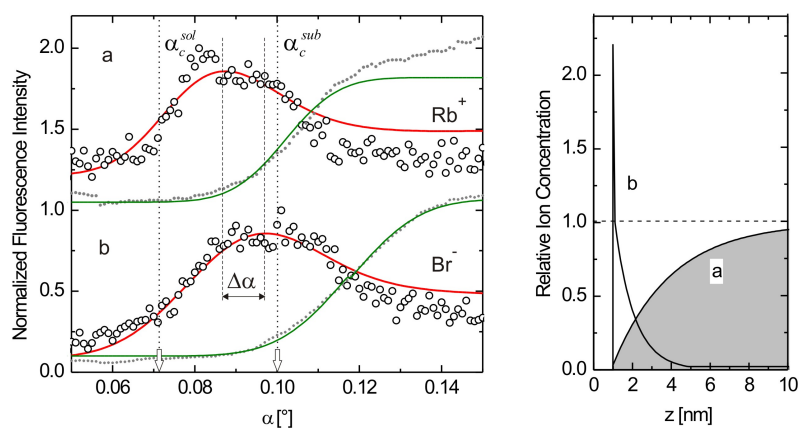
Figure 3.14: Examples for the XSW analysis of ion distributions in liquid layers on APTS-modified Si wafers with the corresponding best-fit ion profiles (right). Fluorescence intensity is plotted for a co-ion (Rb^+) distribution (**a**, curve shifted) and for Br^- counterions (**b**). Here, the distinguishing feature of the different distribution types is the angular difference $\Delta\alpha$ of the positions of fluorescence maxima. The fit of Si fluorescence (green line) allows for a very precise determination of the critical angles (indicated by arrows on the angle axis); the applied values of variance σ_{conv} are $0.0105°$ (**a**) and $0.0135°$ (**b**).

uncertainity of the data from liquid films is significantly larger compared to the results from droplet samples (summarized in Table 3.2), which is caused by the limited accuracy of L_D determination as described above.

Figure 3.15: Interfacial charge of APTS-functionalized Si as a function of the pH value. The ions forming the analyzed distributions were Br$^-$ in the acidic and Rb$^+$ in the alkaline solution.

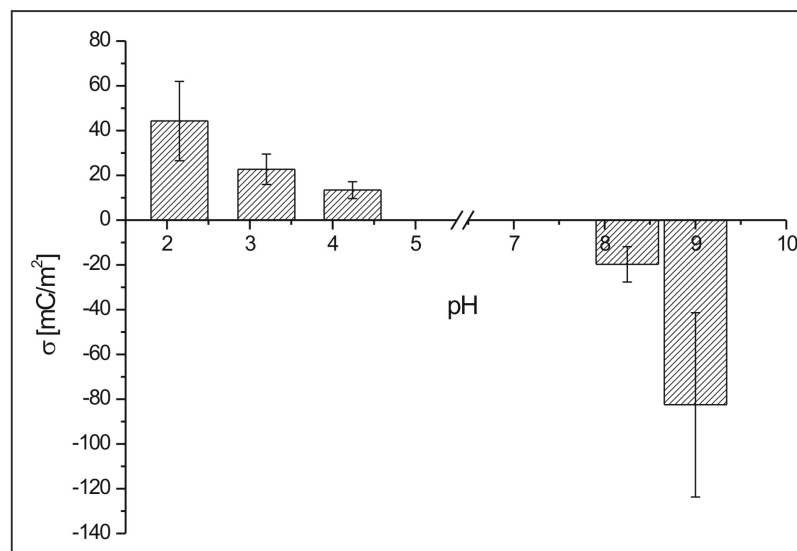# 3.6 Surface Functionalization by Polymer Brushes

3.6.1 Properties and Applications

Coating surfaces with polymer brushes is a further important type of surface functionalization. This method features chains of various polyelectrolytes which are grafted with one end onto a substrate by means of an anchoring layer. The interaction of the surface with the solution is influenced by the pH value, which determines the surface charge and wetting properties by protonation/deprotonation processes. Polymer brushes are used to control surface properties like adsorption behavior (e.g. of proteins or cells), wetting and adhesion [64]. An example for an application of medical and scientific interest is the development of pH-controlled microfluidic valves. The aim of the XSW experiments presented here is the measurement of the ion distribution inside the polymer brushes layer and in the adjacent solution as a function of the pH value and the applied ion species. By this means, a pH-controlled switching of interfacial properties is studied. Again, two analytical methods were combined to obtain a comprehensive characterization of the interaction of polymer brushes with the adjacent solution. Infrared spectroscopic ellipsometry (IRSE) was applied to the detection of the dissociation of carboxylic groups and XSW measurements were used for the analysis of the ion distribution inside and above the brushes layer [65]. This combination has already proven useful for the analysis of thin organic films [66].

3.6.2 Sample

The analyzed sample was a silicon wafer covered with brushes of poly(acrylic acid) (PAA), grafted onto the surface by means of an anchoring layer of polyglycidil methacrylate (PGMA). Figure 3.16 shows a monomer of the PAA chain in two different states: In acidic solutions (case **a**), the carboxylic groups forming the chain are collapsed, forming a thin layer of low surface charge on the substrate. The addition of hydroxide solution causes the deprotonation of the carboxylic groups. The then negatively charged chains repel each other, resulting in a swelling and stretching of the brushes layer in contact with aqueous solution (case **b**). A high concentration of cations in the solution induces a hydrophilic surface. Experiments were performed under acidic (pH 2) and alkaline (pH 8) conditions, adjusted by HCl and KOH solution. Similar to the experiments with molecular functionalizations, a non-ionic surfactant was added to the solution, leading to the formation of droplets in the present case. However, a high degree of beam divergence
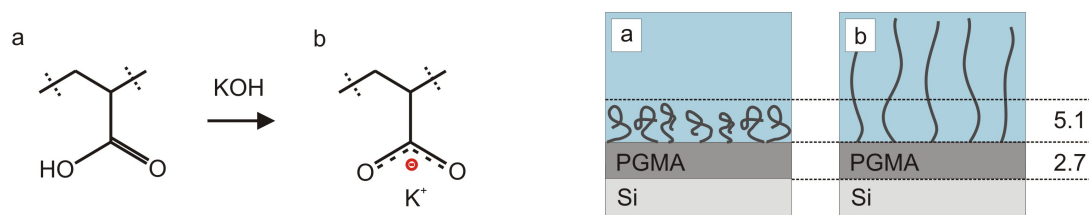
Figure 3.16: PAA polymer brushes under acidic (**a**) and alkaline (**b**) conditions. Left: Monomer of the PAA chain in neutral (**a**, COOH) and deprotonated (**b**, COO⁻) state. Right: Different states of the brushes layer, the (ellipsometrically determined) thickness values are given in nm.

occurred, reducing the vertical measuring accuracy. Possibly, this is due to some droplets with a too large volume.

3.6.3 Ellipsometry Experiments and Results

Prior to XSW experiments, the sample was characterized by infrared ellipsometric spectroscopy. Figure 3.17 shows a series of $\tan \Psi$ spectra recorded at pH values between 2 and 10. All spectra are referenced to the measurement performed at pH 2, so the change of the intensity of the vibrational bands are obvious. In the case of PAA brushes in contact with acid solution, one vibrational band is found at 1728 cm^{-1}, induced by the C=O double bond of the COOH group. On changing the pH value to 8 - 10, this band disappears and others at 1560 cm^{-1} and 1414 cm^{-1} appear. These bands indicate the existence of the COO⁻ group under alkaline conditions. The intensity ratio of the COOH and COO⁻ vibrational bands allows the conclusion to the actual state of the brushes layer. From the results of IRSE experiments, the expectation concerning the behavior of the PAA brushes is supported: In acidic solution, the brushes are collapsed, forming a thin, hydrophobic layer on the substrate. The addition of potassium ions leads to the deprotonation of carboxylic groups. The resulting repulsion of negatively charged PAA chains causes the layer to swell, so that the solution can penetrate to the reflecting surface. In this state, the surface is hydrophilic. Repeated ellipsometry measurements performed by Aulich et

al. have evidenced the reversibility of this pH-controlled switching of the brushes [65].
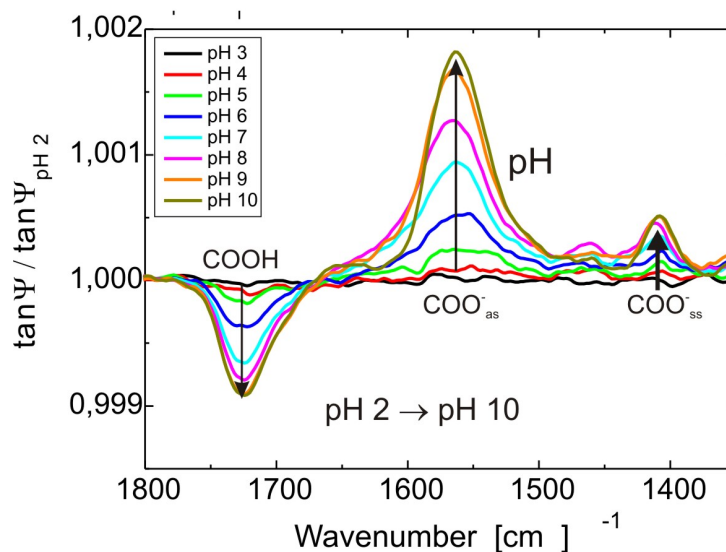

Figure 3.17: Series of $\tan \Psi$ spectra including the vibrational bands of the COOH and the COO− group recorded during the switching of PAA brushes [65].

3.6.4   XSW Experiments and Results

The ion distribution near the interface is expected to be influenced by the protonation state of the PAA brushes. In particular, the conditions, under which ions can penetrate into the brushes and reach the anchoring layer are of interest. The direct contact of ions with the interface is suspected to have a negative effect on the stability of the PGMA anchoring layer, especially for high pH values. During the measurements, the sample was kept in a sample cell, schematically shown in Figure 3.18. Inside the cell, a humid atmosphere was created by the enclosure of a small water reservoir under a mylar foil in order to avoid the evaporation of the marker solution. The described experiments were performed at DELTA, beamline 8.

Results and evaluation of fluorescence measurements are shown in Figure 3.19. All curves have the form of counterion signals. The simulation is calculated with a Debye length of 3 ± 1 nm in each case. A more precise determination of L_D is not possible due to the high beam divergence ($\sigma_{conv} = 0.03°$). The counterion character of the distributions agrees with the ζ-potential values reported by Houbenov [67]: In acidic solutions (pH < 3.2), the PAA surface is weakly positively charged, attracting anions. Alkaline
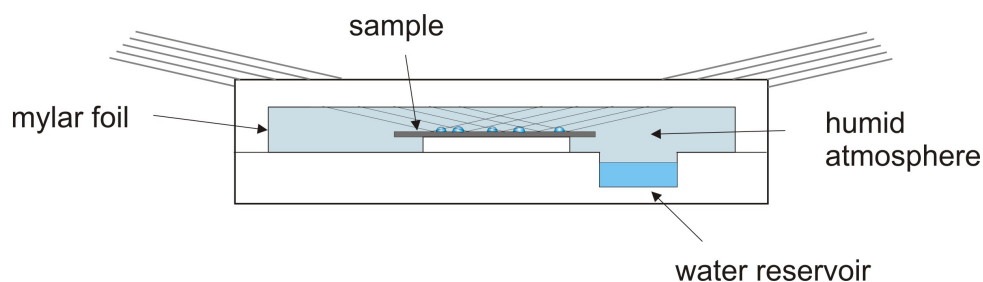
Figure 3.18: Longitudinal section of the sample cell designed for grazing-incidence X-ray experiments in humid atmosphere. The beam from the synchrotron and marker fluorescence pass a thin (2.5 μm) mylar foil encapsulating a volume of humid air. The high air moisture prevents the evaporation of the liquid of the sample.

conditions induce a negative polarity of the ζ-potential, so that cations are attracted. Comparing the scans of HCl (**a**) and KOH (**b**) solution, a relative angular shift of the maximum of potassium fluorescence towards the critical angle is observed. This difference between the fluorescence signals can be understood from the best-fit distribution models. In acidic solutions, a marker-free space of extension $d = 3 \pm 1$ nm separates the ions from the interface, similar to the previously discussed experiments (Figure 3.9). The ion distribution in the alkaline solution does not feature such gap, here potassium ions are in direct contact with the interface. Under the conditions of measurement **b**, an interaction of ions with the PGMA layer is possible.

These observations are in good agreement with the behavior of the PAA brushes deduced from ellipsometry measurements. In acidic solution, the PAA layer is impenetrable for the solution as the chains are collapsed, forming a hydrophobic layer of thickness d. In the case of alkaline pH, the adjacent solution can penetrate into the then hydrophilic PAA layer and ions can reach the interface, as the charge of deprotonated carboxyilc groups leads to a stretching of the brushes.

After the measurement at pH 8, the sample was rinsed and again an acidic solution (pH 2) as in measurement **a** was spread onto the wafer. By this means, the reversibility of the switching process should be examined. The resulting fluorescence signal is plotted in part **c** of Figure 3.19. Here, the relative position of the fluorescence intensity maximum is shifted towards smaller angles than to curve **b**. Correspondingly, in the distribution model the ion-free gap ($d = 5 \pm 1$ nm) at the interface reappears, indicating that the PAA brushes have switched back to the collapsed state. This way, the recovery of the sample
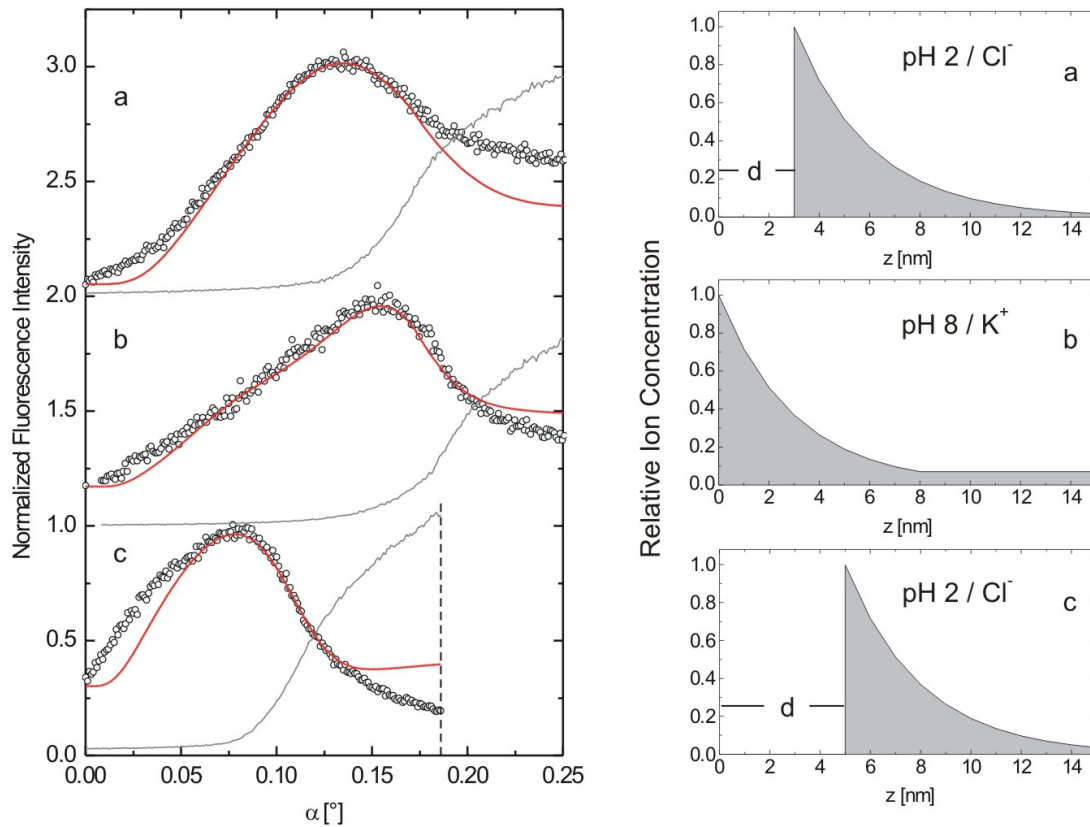
Figure 3.19: Fluorescence signals measured from marker ion solutions in contact with a Si surface coated with PAA polymer brushes (left) with the corresponding marker distributions (right). Curve **a** shows the fluorescence signal of Cl^- ions in pH 2 solution, the corresponding marker profile includes an ion-free space of width $d = 3$ nm. This gap is missing in the K^+ distribution of the subsequently prepared alkaline KOH solution, which indicates a hydrophilic surface. For the measurement **c**, again a Cl^- solution (pH 2) was spread onto the surface. Like in case **a**, a gap of comparable extension occurred, proving the reversibility of the $COOH/COO^-$ conversion. Experiments **a** and **b** were performed at $E = 10$ keV. In case **c**, an energy of 15 keV was applied for measurement and simulation. This leads to an angular compression of the signal but does not affect the information about the ion distribution.

configuration found in measurement **a** is demonstrated. The average value of $d = 4 \pm 1$ nm comes close to the ellipsometrically determined thickness of 5.1 nm of the collapsed PAA brushes layer, as shown in Figure 3.16.

Summary of Chapter 3

The subject of this chapter is the analysis of ion distributions at functionalized solid/liquid interfaces using XSW. First, the characterization of the pH-dependent effect of functional surface groups on the ζ-potential was described. The identification of co- and counterion distributions by means of the typical features of the corresponding fluorescence signals was discussed, followed by the quantitative evaluation of counterion signals by means of the parameters L_D and d. The combination of XSW with streaming current measurements enabled the quantitative measurement of the interfacial charge.

In the case of the second sample type, featuring a coating with polymer brushes, the pH-controlled switching of surface wettability was observed by the measurement of ion penetration into the brushes layer.

The liquid phase covering the functionalized surface has been detected in the form of sub-μm sized droplets and thin layers; typical properties of the different sample types in terms of X-ray scattering and refraction are explained. The analysis of element distributions in thin layers will also be the topic of the next chapter, dealing with XSW analyses of polymer layers applied to the development of organic semiconductors.

Chapter 4

XSW Analyses of Organic Semiconductors

4.1 Solution-Processed OLEDs

Solution-processed Organic Light Emitting Diodes (OLEDs) constitute a promising approach for the development of illumination and display technologies. Main advantages of this new class of semiconductors are a high efficiency, low energy consumption and a cost-effective production [68]. Compared to conventional fabrication methods like thermal evaporation or organic vapor-phase deposition, solution-processed OLEDs can be produced by simple printing techniques, which enables a considerable reduction of production costs. Light of different colors can be produced by the application of adapted polymers [69], and white light by the combination of several polymers layer emitting different colors in one device.

Multilayer structures have proven advantageous in terms of stability, efficiency and lifetime, which has been a critical factor in early OLED applications. In the following, a new fabrication method for solution-processed OLEDs known as PEDOT-initiated crosslinking (PIX) process will be presented.

The PEDOT-Initiated Crosslinking Process

The PIX process is based on a crosslinking reaction which takes place inside a polymer and is started by the heat-induced dissociation of polystyrene sulfonic acid. The main advantage of the heat-induced PIX process is the abandonment of photoacids, which are required for conventional photochemical methods. This significantly extends the life-

time of the devices. Furthermore, the layers produced by this process exactly replicate the surface structure of the substrate. This way, a laterally constant layer thickness is achieved, regardless of substrate roughness. This property is very advantageous for the production of large-scale illumination elements, as practically any material can be coated by the semiconducting polymer layers. Thin, flexible displays or lighting panels can be fabricated using foils as substrate. The PIX procedure is also excellently suited for the coating of three-dimensional objects with light-emitting polymer layers. So, for example, the classical shape of a light bulb can be combined with the innovative OLED technology [70].

The principle of the reaction is schematically shown in Figure 4.1. A substrate is coated with the polymer, which is composed of a bottom layer of a PEDOT/PSS mixture (Clevios P; H. C. Starck)[1] and a top layer of the crosslinkable polymer (x-polymer in Figure 4.1, the chemical structure of the compounds is given in reference [69]). In the readily fabricated device, the crosslinked polymer layer functions as hole conductor.

Heating of the polymer composite to a curing temperature of 130 to 200°C induces the dissociation of PSS molecules, releasing a proton. This first proton initiates the crosslinking process by the opening of an oxetane ring. By this step, referred to as cationic ring opening (CROP), the oxetane molecule is activated. The cation generated this way continues the chain reaction, until the entire layer is crosslinked and an insoluble polymer network is produced. The oxetane-containing polymer is particularly suited for this process, as it features practically no variation of volume upon curing, so a breakup of the layers is avoided. After removing the non-crosslinked part of the polymer, a second layer can be added using the same procedure. The CROP reaction is initiated at the surface of the PEDOT layer and proceeds in vertical direction. A reactive front of counterions, parallel to the PEDOT surface, is assumed to migrate through the layer alongside the ring-opening cation. The results from XSW experiments presented in this work evidence this front.

The Counterion Front

The procedure described above effectively led to the formation of insoluble polymer layers, which supports the proposed reaction mechanism. However, for its verification the existence of the counterion front still had to be evidenced [68]. Considering the properties

---

[1]PEDOT: Poly(3,4 ethylenedioxythiophene), PSS: Poly(sodium 4-styrenesulfonate) In the following, the compound is referred to only as PEDOT.

of PEDOT/PSS and the reaction process, sulfur containing anions (HSO_4^- or SO_4^{2-}) are expected to form this front [68, 71]. X-ray Standing Waves are a well-suited approach to this task. In particular, the spatial resolution on the vertical axis in the nanometre range and the low detection limit even for light elements like sulfur are ideally suited for the detection and characterization of the sulfur ion front. The experiments discussed in the following were performed at beamline 8 of the DELTA synchrotron radiation facility.
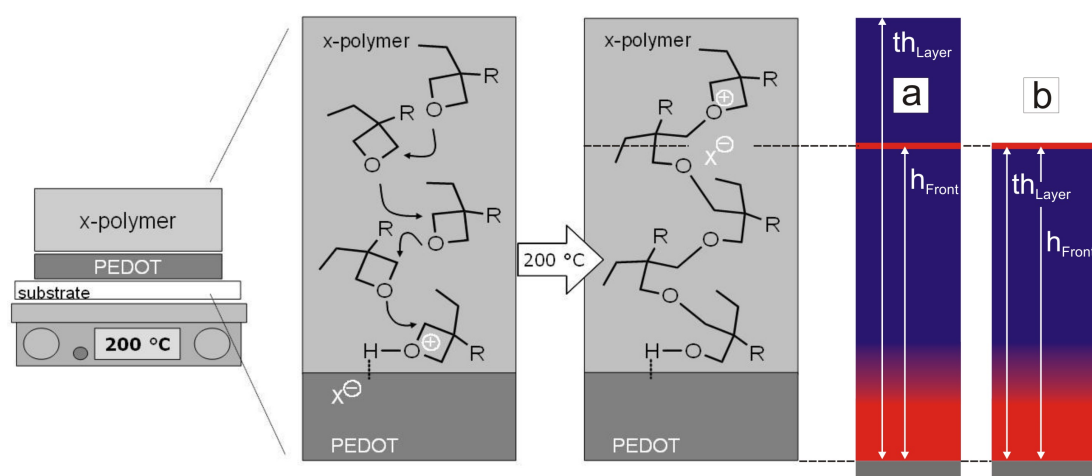

Figure 4.1: Left: Principle of the PIX crosslinking mechanism. The heating of the sample starts the cationic ring opening polymerization (CROP); protons released by dissociation of PEDOT/PSS molecules initiate the crosslinking process. A front of reactive sulfur ions (X^-) parallel to the interface migrates through the polymer layer. The right picture schematically shows different sample compositions, where the non-crosslinked polymer remained (**a**) or was removed (**b**)) after crosslinking. The sulfur concentration is marked red.

4.1.1 Samples

Two series of crosslinked polymer layers (indicated A and B) and several reference samples have been analyzed. Series A was analyzed in order to detect and to characterize the counterion front, the results are shown in Figure 4.5. The purpose of the experiments with sample series B (data shown in Figure 2.12) is the characterization of the XSW field. In particular, the knowledge about the vertical intensity distribution and the upper limit

of the field is important for a correct evaluation of the fluorescence signals from the given marker distributions. The reference measurements are done to verify that the front was excited by standing waves and not by resonance effects.

The composition of the sample is schematically shown in the right part of Figure 4.1, with the expected sulfur distribution marked in red. The thickness of the polymer layer, which was spin-coated onto silicon wafer substrates, ranged between 70 and ca. 150 nm. The extension of the crosslinked phase was adjusted by the temperature and duration of the heating process. The remaining (non-crosslinked) part of the polymer has been removed using tetrahydrofuran (Figure 4.1 **b**), except for samples used for reference measurements (Figure 4.1 **a**).

Concerning the properties of refraction and reflection, which determine the XSW field and the fluorescence signal, samples of the present type can be regarded as "solid solutions" rather than as solid multilayer structures. In these systems, which have been analyzed by Krämer et al. [72, 73], substrates are covered by several layers of different electron density, so the incoming beam undergoes multiple reflection and refraction before reaching the substrate.

Instead, in the present samples the incident beam is refracted and reflected only at the surface of the polymer layer and at the interface between the polymer "solution" and the silicon substrate, the vertical inhomogeneity of the electron density within the polymer is too small to cause any deflection of the beam. This results in a beam path like in liquid films, which is described in section 3.5. Therefore, the geometrical considerations discussed referring to Figure 3.5 **a** apply, also the notation for the critical angles α_c^{sol} and α_c^{sub} is maintained in the following.

4.1.2   X-ray Resonance in Thin Layers

In thin layered samples with sufficiently plane-parallel interfaces, a second standing waves field can be generated by resonance of X-rays, which are reflected at the upper and lower interface of the layer and interfere [58]. In this case, the sample acts as waveguide for the electromagnetic field [74]. The interference field enhances scattering, so in almost all polymer layers, oscillating Compton and Rayleigh signals were detected. The same oscillations can be detected in the fluorescence signal of the marker distribution, an example is given in Figure 3.7 **a**. Also in some liquid films this effect was found, an shown in diagram **b** of the same Figure. This plot shows the XSW-excited fluorescence signal of a counterion distribution which is superimposed by strong resonance-induced intensity

oscillations. In practice, the occurrence of such superimpositions considerably complicate or even make impossible the to identify the relation between angle-dependent fluorescence signal and the position of markers above the interface.

Therefore, an unambiguous evaluation of XSW-excited fluorescence data from thin layers is only possible when scattering influences can be excluded. For grazing incidence X-rays in thin layered structures, resonance effects induced by multiple reflection between interfaces of media of different electron density can occur.
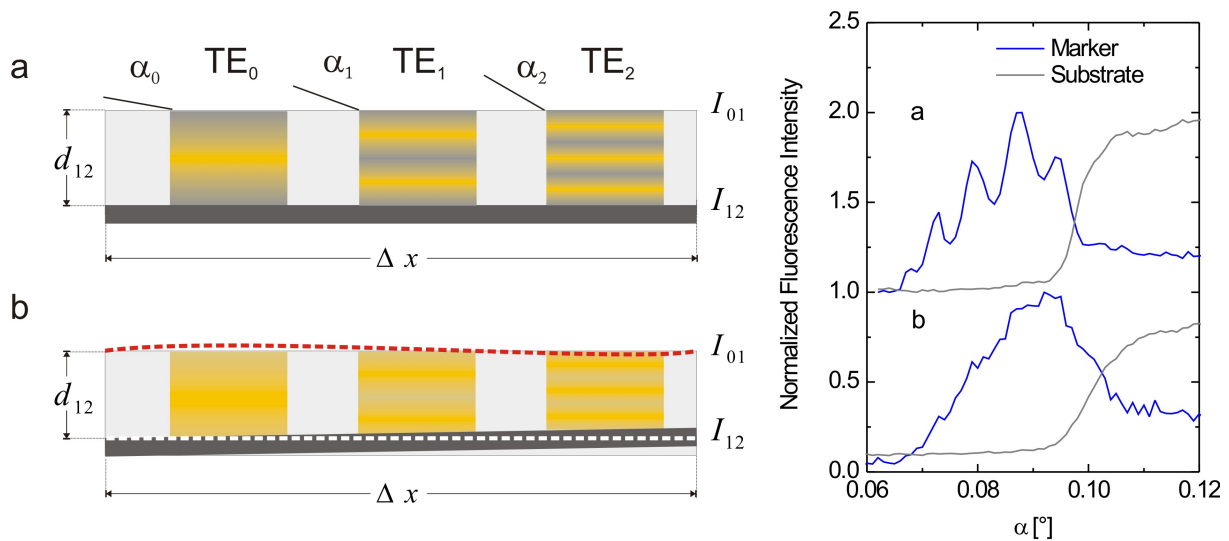

Figure 4.2: Formation of transverse electric field modes inside a thin layer. In the case of plane-parallel interfaces (**a**), interference of the radiation reflected at the interfaces I_{01} and I_{12} induces a vertically oscillating intensity distribution (TE modes). Scattered radiation causes additional excitation of marker fluorescence, leading to an oscillating contribution to the XSW-excited signal. Non-parallel or undulated interfaces (**b**) suppress resonance effects, here nearly no superimposition of the XSW-excited fluorescence is detected.

The beams reflected at the upper and lower surface of the layer then interfere and transverse electric field modes (TE_n) are excited within the layer. The number and the vertical position of these intensity oscillations depend on the incident angle α, the layer thickness d_{12} and the wavelength λ of the incident radiation. The first node, emerging at $\alpha_0 \approx \alpha_c^{sol}$, features one intensity maximum at $z = d_{12}/2$. The second TE mode includes two maxima at a distance of $d_{12}/4$ to the substrate and to the polymer surface, respectively. With increasing index of the modes, the number of interference maxima rises and the outmost maxima approach to the upper and lower boundary of the layer. The

complementary effect is the appearance of the so-called Kiessig fringes in the reflectivity of layered structures [75]: The angle positions of reflectivity minima correspond to those angles, where the conditions for X-ray resonance inside the layer are fulfilled and so, a maximum of Compton scattering and fluorescent emission is excited.

Evidence for this waveguide-effect can also be found in data shown in Figure 4.2. The fluorescence signal from two layers containing similar element concentration profiles is presented, in both cases markers were distributed like counterions. In case **a**, the occurence of TE modes excites Compton scattering, which itself contributes to marker fluorescence excitation, is evident from the oscillations superimposing the signal. Here, a high parallelism of the interfaces I_{01} and I_{12} favors the generation of X-ray resonance. The high contrast between the vertical interference minima and maxima (drawn yellow in the sample composition sketch) leads to a strong oscillation superimposing the marker signal.

A different sample structure is shown in case **b**: The two interfaces are not perfectly plane-parallel, but feature a minimal variation of the distance d_{12} and a slight undulation of the air/polymer interface I_{01}. This structure of the layer inhibits the formation of a homogeneous resonance field extending over the entire irradiated area. A vertical offset between the maxima and minima of TE modes is induced and leads to a reduction of contrast of the interference field.

In the samples used for marker distribution analysis, generally $\Delta x \gg d_{12}$ applies, therefore the geometrical properties inhibit or at least significantly suppress the formation of TE modes inside the polymer layer. Correspondingly, the scattering-induced oscillations are nearly undetectable in the related fluorescence signal. As already discussed in section 3.3.3, scattered radiation contributes to the excitation of marker fluorescence. This modulation can occur in solid and in liquid layers, as shown in Figure 3.7 **a/b**. Resonance of grazing incidence X-rays has also been used for the measurement of element distributions in thin layers [76, 77]. However, in the experiments presented in the following it has been tried to avoid this effect, as the standing waves field generated by reflection at one surface proves significantly more appropriate for the analysis of the samples. With vertically moving field maxima of angle-independent intensity, the present distribution can be scanned more precisely than with vertically fixed maxima of the resonance field, which only emerge at certain angles. Furthermore, as the sulfur front, which is the most interesting part of the element distribution is located at the top of the layer in most samples, fluorescence maxima excited by the two interference fields almost completely superimpose each other, as principally shown in Figure 4.3. Thus, an unambiguous assignment of the

signal one of these fields is not possible. A detailed discussion of theory and experiments is given in the references [43] and [58]. Here, only the conditions to sample geometry for the appearance of TE-mode excited Compton scattering will be explained.

In literature, both types of interference fields are referred to as x-ray standing waves. To distinguish the two types of X-ray interference, in this work the term "XSW field" is reserved to interference fields caused by *single* reflection at a surface, as described in section 2.3.3.
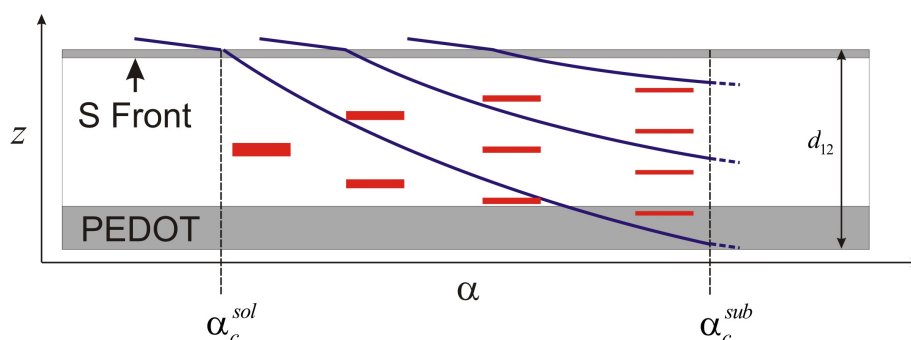

Figure 4.3: Angle-dependent position of the maxima of the XSW field (blue) and of the resonance field (red). The gray areas mark the sulfur containing parts of the polymer layers.

In principle, a correction of the scattering influence on the XSW-excited marker signal is possible, as discussed in section 3.3.3. However, in the fluorescence signal of the present samples two oscillations of similar periodicity and different amplitude superimpose. In this case, such correction introduces ambiguity in the measurement of the sulfur distribution. As such, only samples of type **b** from Figure 4.2 were chosen for the analysis, as here fluorescence data could be evaluated without any intensity correction. An appropriate method for the preparation of polymer layer samples suited for XSW experiments is the use of thin (0.3 mm) silicon wafers as a substrate. These wafers feature a slight bow, possibly induced by the spin-coating process. This inhibits the formation of interference between the two interfaces of the polymer, but produces only minor beam divergence, allowing an undisturbed formation of the XSW field. Wafers fulfilling this criterion can be identified during the adjustment of the sample in the synchrotron beam. Also the lateral homogeneity of the thickness of the polymer can be estimated: Layers of constant thickness are of uniform color, here the occurrence of resonance is likely. In the case of a

slight lateral thickness variation also the color of the sample varies, which is comparable to the appearance of oil films on water. These samples are generally more appropriate to XSW analysis.

4.2 Measurement of the Sulfur Distribution

In Figure 4.4, a series of subsequently recorded fluorescence spectra is plotted as function of the incident angle. The $K\alpha$ fluorescence lines of three elements can be identified: silicon (substrate, $E = 1.74$ keV), sulfur (analyte, $E = 2.31$ keV) and argon (ca. 1% in air, $E = 2.96$ keV).
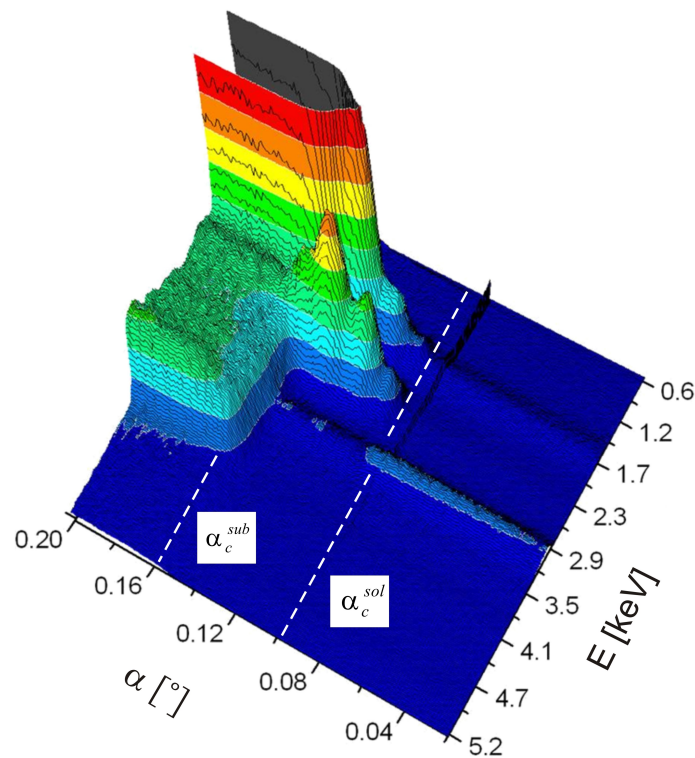
Figure 4.4: Sequence of fluorescence spectra from the XSW analysis of OLED polymer layers. Marker fluorescence (S $K\alpha, E = 2.31$ keV) is detected between α_c^{sol} and α_c^{sub}. The signal of substrate fluorescence (Si $K\alpha, E = 1.74$) keV could not be plotted completely due to its high intensity, the high background level up to $E = 3.5$ keV is related to the experimental settings.

At $\alpha = 0.11°$, the appearance of sulfur fluorescence indicates the penetration of the

beam into the polymer layer. The angular dependent intensity oscillations of the sulfur signal are characteristic for a thin marker layer. The number of oscillation maxima roughly indicates the position of this layer, where the appearance of n fluorescence maxima corresponds to a distance from the reflector of $n \cdot a$, with the XSW field period a as discussed referring to section 2.3.3 (see Figure 2.11 and equation 2.27). Similar to the fluorescence signal of liquid layers, the critical angles α_c^{sol} of the polymer layer and α_c^{sub} of the silicon substrate can be seen. The counts recorded for angles smaller than α_c^{sol} result from excitation through scattered radiation. Furthermore, along the beam path argon fluorescence is generated.

At α_c^{sub}, not only silicon fluorescence rises, but also the noise level in the energy range up to $E \approx 3.5$ keV. This effect is an artifact caused by the detector settings, which were optimized for low count rates. Two silicon $K\alpha$ photons reaching the detector within the dead time were counted as one of double energy. In later experiments, this problem has been avoided by a modification of detector and amplifier settings, cutting off a part of substrate fluorescence.

Results and evaluation of the first series of XSW measurements are shown in Figure 4.5 [78]. The thickness of the polymer layers th_{Layer} of samples **a - d** was chosen in the range of 70 to 130 nm and determined using a profilometer to within ± 5 nm prior to XSW experiments. As a cross-check, one reference sample has been prepared, omitting the heat treatment (measurement **e**). Here, no detection of a polymerization front is expected. The characteristics and interpretation of the fluorescence signals plotted in Figure 4.5 is discussed in the following.

- Curves **a - d** are similar to counterion signals superimposed by an intensity oscillation induced by the transition of XSW antinodes through a thin marker layer. The best-fit distribution models confirm the hypothetised sample composition, supporting the proposed reaction mechanism. Sulfur found in the near-interface sample volume ($z \leq 15$ nm) belongs to the PEDOT layer. The thin sulfur-containing layer detected at distances between 70 and 130 nm above the substrate can be identified as the expected sulfur counterion front. Furthermore, the expectation concerning the cross-check measurement **e** is confirmed. No oscillations are detected in the fluorescence signal, indicating the absence of the sulfur front. The triggering of the crosslinking process by sample heating and the relation between the duration of sample heating and the distance to which counterions have migrated is evidenced. Thus, the assumed reaction mechanism is proven.
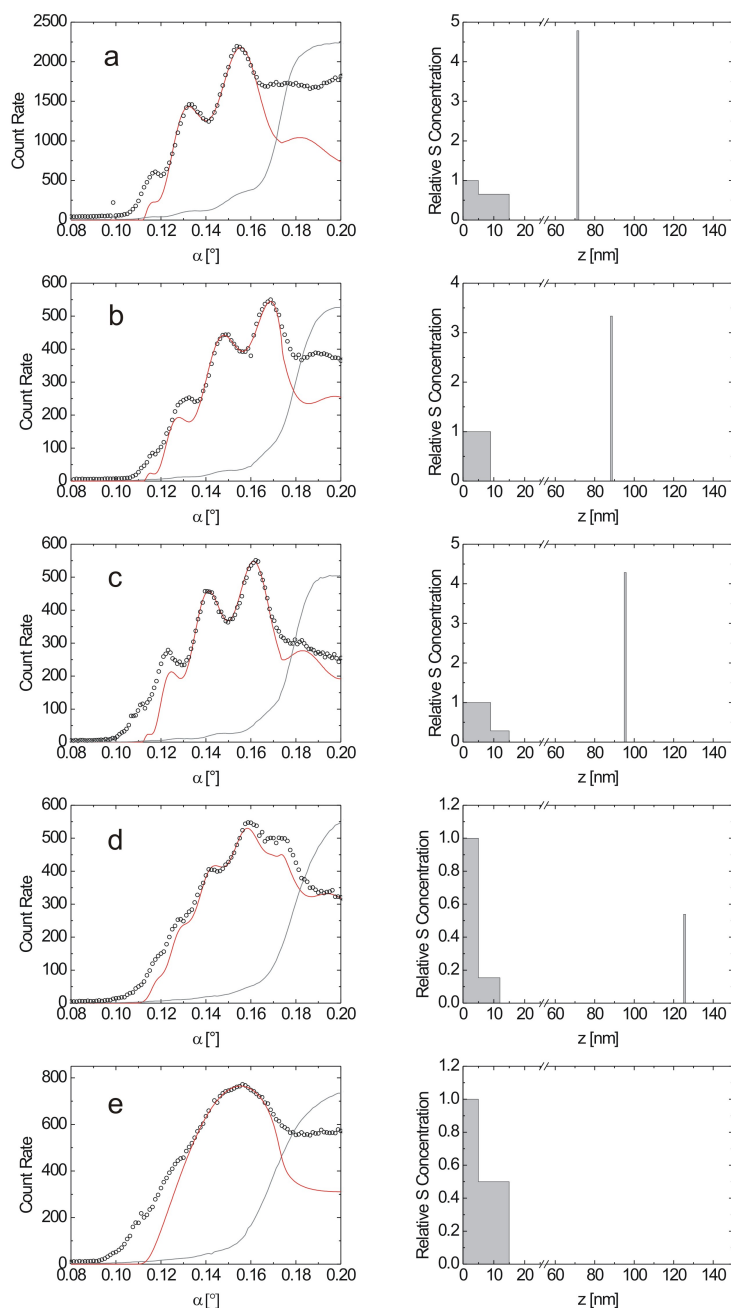
Figure 4.5: Standing waves scans of OLED polymer layers (samples series A) crosslinked to different extents (left) and the related best-fit distribution models (right). The marker concentration of the PEDOT layer ($z \leq 15$ nm) and the S front can clearly be distinguished. In the samples **a – d**, the front was detected at the positions given in Table 4.1. The signal plotted in graph **e** was recorded from a non-crosslinked polymer layer, correspondingly no oscillations of XSW-generated fluorescence intensity occur and the distribution profile only contains the model of the PEDOT layer. Radiation of $E = 10$ keV was used for the measurements.

- Considering the relative amplitude of fluorescence oscillations and the measured sulfur concentration in the corresponding front models, a significant decrease is detected in measurement **d** compared to the previous scans. This phenomenon cannot be explained by the crosslinking mechanism. Instead, it is best explained by the vertical limitation of the XSW field to $z \approx 140$ nm, as discussed in section 2.3.6. The z-dependent excitation of the front will be studied in more detail in further experiments discussed in this work.

- The models of the PEDOT layer feature a gradient-like sulfur distribution.

- In all experiments, measured intensity exceeds the simulated signal in the angular range around α_c^{sol}, which is best visible in measurement **e**. Probable reasons for this effect are a slight bowing of the polymer surface or a contribution to fluorescence excitation from resonance-enhanced scattering, which had not been completely suppressed. This is likely, as in Compton intensity weak oscillations were detected. Therefore, the simulation has been optimized to the data recorded in the range $\alpha \geq 0.13 - 0.14°$. Fortunately, the amplitude of the resonance-enhanced contribution to fluorescence is low compared to the XSW-excited signal, so the reliability of the XSW experiments is not affected.

- Regarding the concentration of sulfur ions in the front, only an estimation can be made: Using X-ray photoelectron spectroscopy, the sulfur concentration of the front (as top layer) could not be detected. Thus, from the detection limit of the applied instrument (Axis HS, Kratos Analytical) the upper limit of concentration can be assumed to be 0.5% - 1%.

In the case of the samples discussed so far, the non-crosslinked part of the polymer above the front had been removed. Thus, the sulfur front was expected at th_{Layer}. The comparison of the data from XSW and profilometer measurements given in Table 4.1 shows a good agreement between the results of the two methods.

A further reference sample has been prepared using the same procedure as for sample **a**, therefore the counterion front was expected at ca. 70 nm. However, in this case the non-crosslinked part of the polymer above the front was not removed, so the thickness of the polymer layer remained 130 nm. In Figure 4.6, fluorescence and reflectivity measurements of the two samples are plotted. The difference of layer thickness is evident from the reflectivity curve, where a shift of the Kiessig fringes of the two curves appears. However, in the fluorescence measurement the intensity maxima are detected at identical angle
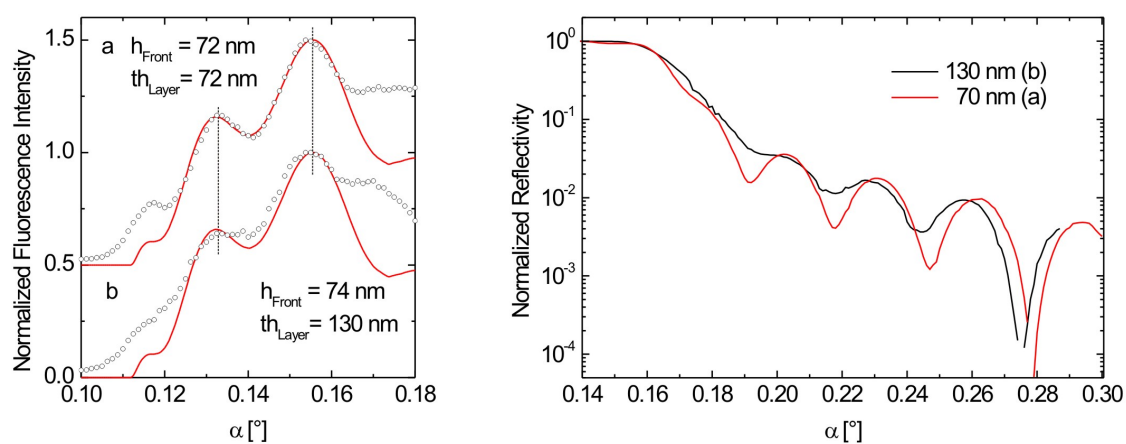
Figure 4.6: Fluorescence signals from samples of similar S front position h_{Front}, but different total thickness th_{Layer} of the polymer layer. In the case of sample **a**, the not crosslinked polymer had been removed, whereas it remained above the S front of sample **b**. Sulfur fluorescence maxima (left plot) of the two samples are at the same angular position, independently from the difference of layer thickness. The layer thickness difference is demonstrated by the comparison of the reflectivity curves shown in the right graph.

positions ($\alpha = 0.135°$ and $\alpha = 0.155°$), irrespective of layer thickness. This way, the influence of resonance effects on the fluorescence signal can be excluded, as the periodicity of this kind of excitation strongly depends on the thickness of the layer.

E [keV]	Scan	t_{cl} [s]	T [°C]	h_{Front} [nm]	th_{Layer} [nm]	C_{Front}
10	a	15	200	72	70	4.8
	b	60	200	88	85	3.3
	c	180	200	96	95	4.3
	d	600	200	126	130	0.7

Table 4.1: Experimental parameters of the distribution measurements of sample series A (Figure 4.5). The duration of the sample heating is indicated t_{cl}, th_{Layer} gives the layer thickness measured using a profilometer ($\Delta th_{\text{Layer}} = 5$ nm). The position of the sulfur front h_{Front} is determined by XSW scans.

4.2.1   Accuracy of Sulfur Front Analysis

Position of the Front

The detection and characterization of the sulfur front is an important contribution to the verification of the PIX process. Therefore, in the following the achievable precision of XSW measurements in terms of position and thickness of the front will be discussed in more detail. First, the accuracy of the measurement of the front position will be estimated. For this purpose, two simulations of slightly modified front position were fitted to the fluorescence curve plotted in Figure 4.5 **a**, where the best fit is achieved for $h_{\text{Front}} = 72$ nm. In the models applied to the simulation shown in Figure 4.7, the front in the distribution model is shifted 2 nm upwards and downwards, respectively.

The results of these modifications are shown in Figure 4.7. In both cases, the accordance of measured and calculated data significantly decreases. The simulation calculated for the front shifted upwards ($h_+ = 74$ nm, blue line) misses the angular position of experimental data around α_c^{sub}, whereas the shift of the front to $h_- = 70$ nm (red line) leads to a divergence of simulation and experiment at the first fluorescence maximum. From these observations, the position accuracy Δh_{Front} can be estimated to a maximum of 2 nm for the present sample.
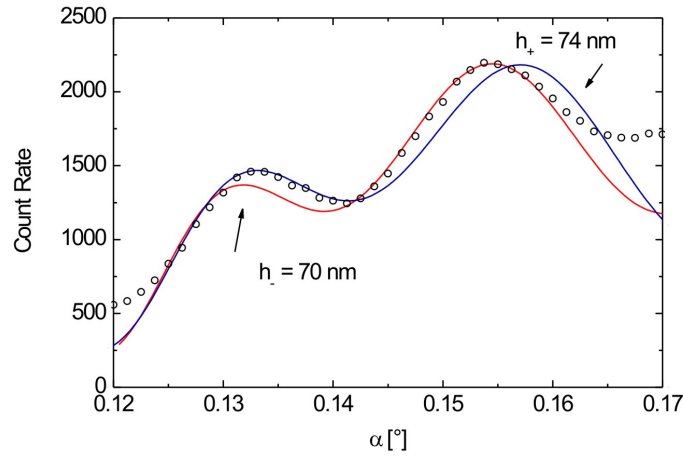
Figure 4.7: Estimation of $\Delta h_{\mathrm{Front}}$. Fluorescence data are taken from Figure 4.5 **a**, simulations are calculated using distribution models of slightly modified front position (blue: $h_+ = 74$ nm, red: $h_- = 70$ nm). In both cases, significant deviations from the optimal fit appear.

Thickness of the Front

The second parameter which will be examined more closely is the thickness of the polymerization front and the concentration profile of the counterions. The question, if a diffuse distribution of ions exists below the front, is of particular relevance for the understanding of the crosslinking mechanism. The presence of such distribution would indicate that ions are lost during the polymerization reaction and the upper limit of possible layer thickness is reached when the remaining counterion concentration in the front is too low to continue the reaction. For some polymers, such termination of the reaction has been observed [68].

So far, in the distribution models used for fluorescence simulation a front thickness of 1 nm was assumed. In Figure 4.8 **a**, a detail from the measurement **c** of Figure 4.5 is shown. Besides the original simulation (plotted red), four curves calculated with modified distributions are fitted to the fluorescence signal. The front models (diagram **b**) are of equal absolute marker quantity, but varied thickness. As criterion of fit quality, the accordance of measurement and calculation around the intensity minimum at $\alpha = 0.15°$ was chosen, as the amplitude of fluorescence oscillations are particularly distinctive at this point.

The first deviations of simulated and measured signal occur for the green curve. Thus, the thickness of the sulfur front in the analyzed sample can be estimated to $th_{\mathrm{Front}} \leq 7$
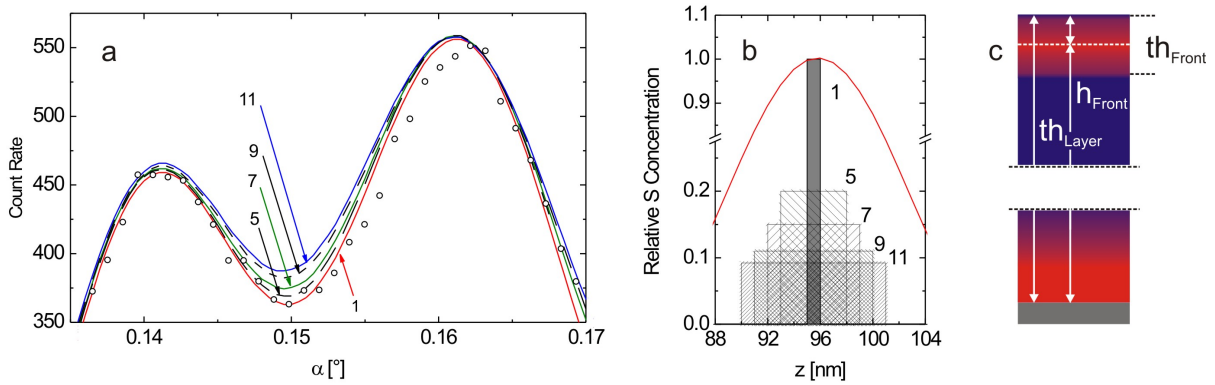
Figure 4.8: Plot **a**: Estimation of the vertical extension of the sulfur front applying distribution models featuring different front thicknesses, as shown in diagram **b**. The first visible decrease of fit quality appears in the case of the simulation calculated for a front model of 7 nm thickness (green line). In the distribution diagram, the minimal period of the XSW field a_{min} (red line) is compared to the different front models.

nm. With standing waves generated by total external reflection, the extension of thinner marker layers cannot be measured. The limiting factor is the minimal distance between the XSW antinodes a_{min}. In the case of marker distributions of larger extent which is comparable to the period of the XSW field, a higher measuring accuracy is achieved. So, for example, the parameters of the counterion distributions were determined with higher accuracy, as discussed in section 3.4.2. Standing waves generated by Bragg reflection at multilayer mirrors or single crystals are of significantly shorter period. A scan with this kind of XSW fields could provide a way to determine the thickness and the concentration profile of the sulfur front.

4.2.2 In-situ Analysis of the Crosslinking Process

The next step of the characterization of the PIX mechanism is the in-situ study of the initiation of the crosslinking process. For this purpose, an experimental setup as shown in Figure 4.1 was utilized. Five XSW measurements of an initially non-crosslinked sample were performed. Between the single scans, the sample was heated to a temperature of 130°C for different time intervals. The resulting fluorescence signals are plotted in Figure 4.9. Curves **a** and **b** are similar to the signal obtained from the non-crosslinked sample shown in Figure 4.5 **e**. Correspondingly, in the best-fit distribution models only the

PEDOT layer appears. After the second heating step, a significant variation of the shape of the fluorescence signal is observed, with **c**, the maximum of fluorescence intensity is shifted towards smaller angles. Now, a front of high marker concentration has to be included into the distribution models.

From these observations, it can be concluded that the crosslinking process has been initiated after a heating time of less than 90 seconds. Comparing the position of the sulfur front in the distribution diagrams **c** - **e**, no further migration is detected after the formation of the front. A probable reason is the limited temperature of the available experimental setup.

Furthermore, compared to the samples of the first series, the distance between counterion front and PEDOT layer is relatively small, it approximately corresponds to the XSW field period a_{min}. Therefore, the spatial resolution of the previous measurements can not be reached in the present case. Despite these experimental restrictions, this is direct evidence for the initiation of the polymerization reaction by heat-induced PEDOT/PSS dissociation.

4.2.3   Relative Excitation of the Sulfur Front

In the chapter dealing with the theoretical aspects of standing waves, the problem of the vertical limitation of the XSW field induced by the loss of coherence of the radiation was introduced. The (idealized) case of linear dependency between the coherent fraction and the path length of the beam inside the sample was discussed as an example. This effect was negligible in the analysis of the electric double layer, where the interesting marker distributions were located within the near-interface part of the sample (ca. $z < 20$ nm). However, in the case of crosslinkable polymer layers, the essential part of the sulfur distribution is located up to 130 nm above the substrate. Therefore, z-dependency of the intensity of fluorescence excitation has to be taken into account. Referring to the distribution models related to sample series A shown in Figure 4.5, a significant decrease of marker concentration representing the counterion front is found in diagram **e**, compared to the first three measurements. This behavior can not be explained by the reaction mechanism, where at most a minor loss of counterions is expected. As the measured fluorescence signal is the product of marker concentration and XSW intensity, the fading of the contrast of the XSW field can be assumed to be the reason for this effect rather than a decay of marker concentration.

The aim of the experiments presented in the following is the characterization of the ver-
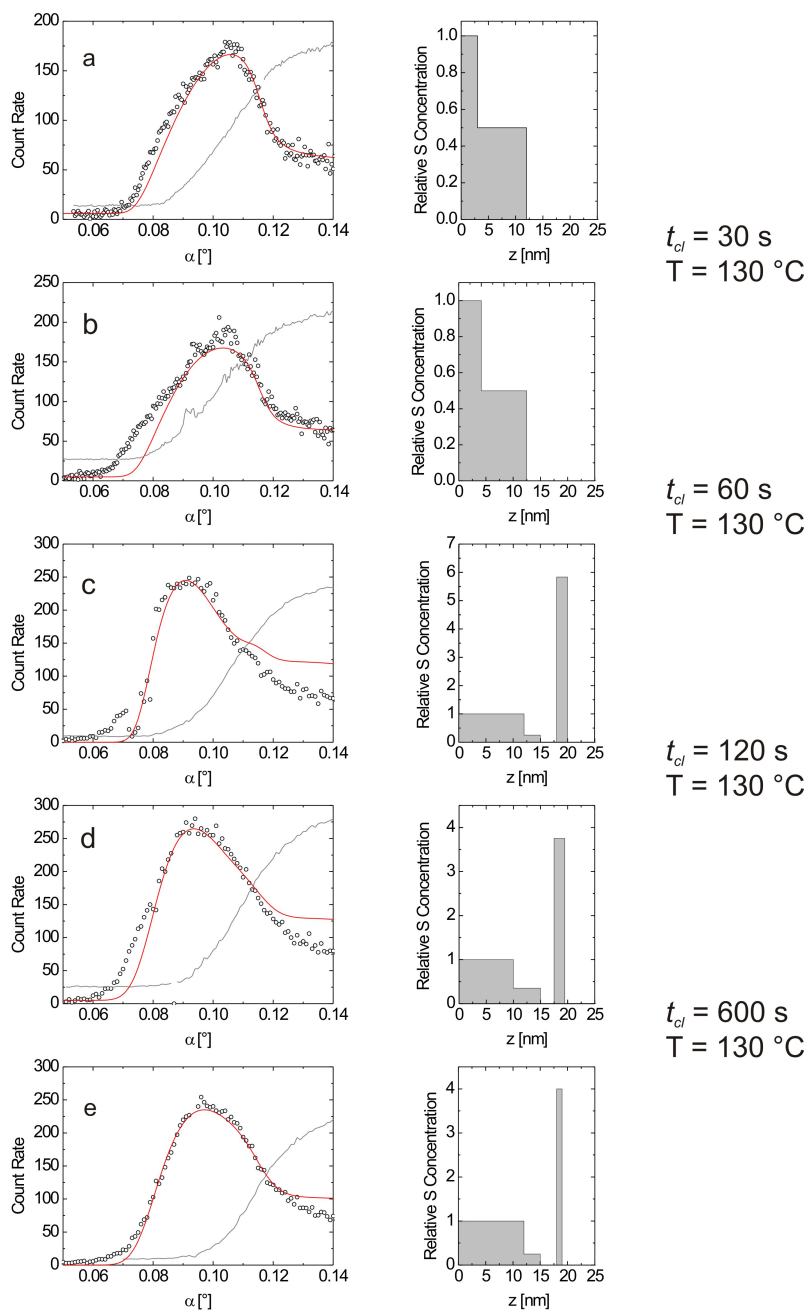
Figure 4.9: Fluorescence Scans of a crosslinkable polymer layer during a stepwise heating process. Between the measurements, a temperature of 130°C was applied to the sample for different time intervals t_{cl}. After the second heating step, an angular shift of the fluorescence maximum to $\alpha < 0.1°$ can be observed in plot **c**, which indicates a variation of S distribution in the sample. The best-fit simulation of scans **c - e** is achieved by a modification of the marker distribution model, which is interpreted as the formation of the S front and its separation from the PEDOT layer. Fluorescence was excited by 15 keV radiation.

tical intensity distribution of the XSW field. For this purpose, a new series of crosslinked polymer samples has been prepared. The positions of the sulfur front were adjusted to values between 67 and 147 nm above the substrate, where the XSW field is expected to fade away.

The Origin of Fluorescence Intensity Oscillations

Similar to the first series of crosslinked polymer samples, the origin of marker fluorescence oscillations has to be identified. In the present samples, the scattering profiles indicate the occurrence of resonance inside the polymer layer. Therefore, it has to be checked if scattering intensity influenced marker fluorescence signal. Figure 4.10 shows the scattering intensity (**a**) and marker fluorescence (**b**) from of one measurement from sample series B ($h_{\mathrm{Front}} = 90$ nm). In diagram (**c**), a reference signal with an obvious correlation between scattering intensity (Compton and Rayleigh) and marker fluorescence (Br $K\alpha$) is plotted. Based on these data it can be shown that excitation of the sulfur front is dominated by the XSW field.
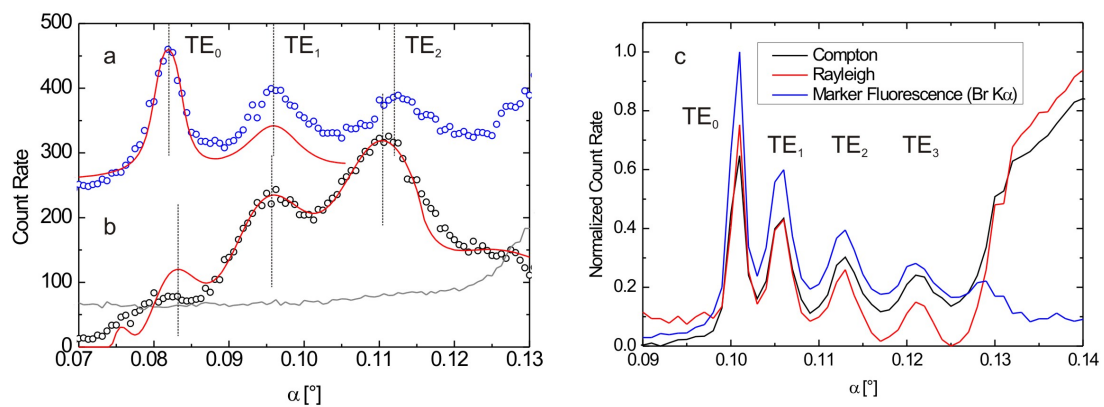

Figure 4.10: Left: Scattering intensity featuring resonance oscillations (**a**, $E = 15$ keV) and fluorescent emission from the sulfur front (**b**, $E = 2.31$ keV) excited by XSW. An angular offset between the intensity maxima of the two signals is visible (indicated by dashed lines) and the shape of the curves is different (first maximum is strongest in curve **a** and weakest in curve **b**). Thus, an influence from scattering on the marker signal can be excluded. Right: An example for a correlation between marker fluorescence and interference intensity, detected in a second sample. Here, the maxima of all signals are at identical angular positions and of similar shape.

- First, in curves **a** and **b** of Figure 4.11, the angle positions of the maxima of Compton scattering and sulfur fluorescence are not identical, as indicated by the dashed lines. This is different in diagram **c**, where both scattering and marker signal are correlated. A probable reason for this different characteristics of fluorescence excitation is the distribution of markers in the respective samples: In the sample belonging to curve **c**, markers were distributed vertically homogeneous over the entire layer thickness, thus overlapping with all field maxima of the TE modes. Also the scattering intensity plotted in **a** originates from the whole layer. In contrast, the data shown in curve **b** represent a sample composition, where marker concentration is confined to the lower (PEDOT) and upper (sulfur front) limit of the layer, where the intensity of resonance-induced field is least.

- Second, the amplitude of signals **a** and **c** is highest for the first maximum excited by the TE_0 mode and decreases for higher modes. This behavior is not detected in the case of marker fluorescence. In contrast, the first maximum of curve **b** is even lower than the simulation.

- Finally, the shape of the maxima is a further distinguishing feature: The XSW-excited sulfur fluorescence **b** signal visualizes the cosine dependency of the intensity distribution $I(\alpha, z)$, whereas the maxima of the resonance-induced signals (**a**, **c**) are considerably sharper.

Consequently, it can be concluded that the fluorescence data shown in Figure 4.11 are generated by the transition of standing waves through the sulfur front and are therefore valid for the characterization of the XSW field.

Estimation of the Vertical Extension of the XSW Field

The parameters of sample preparation and experiments are summarized in Table 4.2. Figure 4.11 shows fluorescence data from sample series B and the related distribution models.

Again, the PEDOT layer including a concentration gradient was detected in all measurements. A gradual decrease in front concentration of the best-fit models is observed until the oscillations indicating the existence and position of the front completely disappear in the last scan **e**. Here, sulfur ions have migrated beyond the coverage of the XSW field. A comparable decrease in the excitation of higher located marker atoms has been
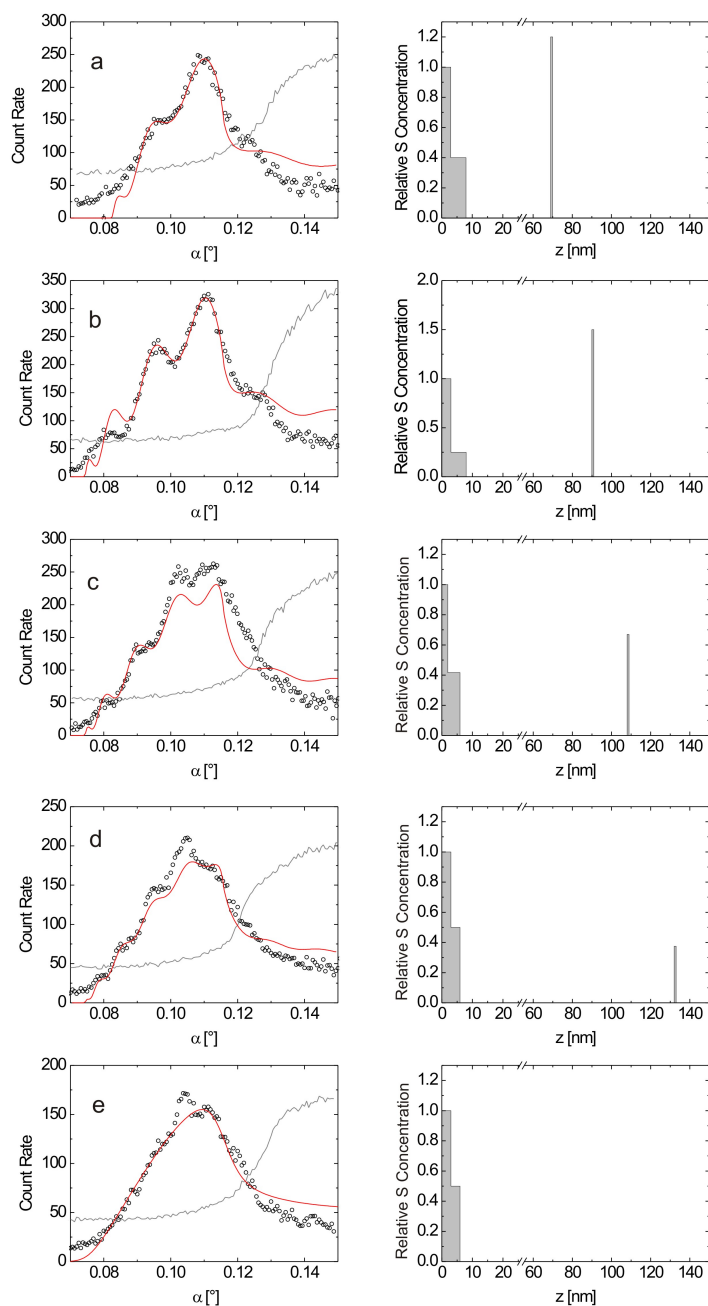
Figure 4.11: Standing waves scans of crosslinkable polymer layers (sample series B) of 67 - 147 nm thickness ($E = 15$ keV). The counterion front is located at the top of the polymer layer in all samples. The decrease of measured concentration of the sulfur front (relative to PEDOT layer) corresponds to the decrease of XSW intensity. In scan **e**, no undulation of fluorescence signal is detectable as the position of the S front $h_{\text{Front}} = 147$ nm exceeds the vertical extension of the XSW field. Thus, the markers of the front are no longer excited to fluorescence. The used X-ray energy was 15 keV.

found in experiments with nanoparticles of more than 100 nm diameter, analyzed under
nearly identical experimental conditions [45].

In scans **c**, **d** and **e**, measured data exceed the calculated curve for the third and
fourth fluorescence maximum at $\alpha \geq 0.1°$, which could not be compensated by optimiza-
tion of the fit parameters. A possible explanation for this discrepancy is the occurrence of
resonance in these samples, causing weak additional marker excitation. As described in
section 4.1.2, the distance between the maxima of the interference field and the interfaces
of the polymer layer decreases for TE modes excited at higher incident angle. The addi-
tional intensity is probably generated, when with rising angle of incidence position of the
lowermost interference maximum is shifted more and more into the PEDOT layer and the
uppermost maximum approaches the sulfur front as schematically shown in Figure 4.3.
The vertical period of higher TE modes ($n > 1$) is similar to the thickness of the PEDOT
layer, thus here resonance-induced contribution to sulfur fluorescence is likely. However,
as discussed before, the analysis of the counterion front is not affected thereby.

E [keV]	Scan	t_{cl} [s]	T [°C]	h_{Front} [nm]	th_{Layer} [nm]	C_{Front}
15	a	20	110	70	67	1.2
	b	40	110	90	90	0.8
	c	90	110	108	111	0.5
	d	120	130	132	130	0.38
	e	300	130	(147)	147	0

Table 4.2: Experimental parameters of the sulfur distribution measurements of sample series
B (Figure 4.11).

Figure 4.12 contains a summary of the relative excitation C_{Front} of the counterion front,
found in the experiments shown in Figure 4.5, 4.11 and in-situ observation of the crosslink-
ing process of Figure 4.9. As the concentration of PSS is not identical in the two series,
also the detected sulfur concentration of the counterion front is different in the respective
XSW results. The sulfur concentration of the PEDOT layer ($z = 0$), normalized to 1, was
chosen for the concentration alignment of the different distribution models. According to
the theoretical considerations in section 2.3.6, the influence of coherence can be assumed
to be least in the near-interface sample volume containing the PEDOT layer. From the
data shown in the diagram, the vertical extension h_{xsw} of XSW fields inside thin layers
of light elements is estimated to be approximately 140 nm. This estimation applies for
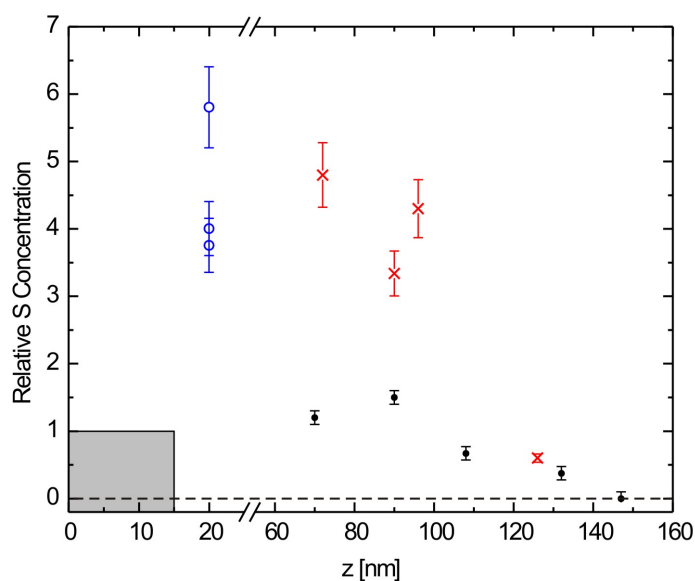
Figure 4.12: Relative concentrations of the sulfur front models applied to the simulation series A (red points) and B (black points) of XSW scans of polymer samples, shown in Figures 4.5 and 4.11, respectively. The data points plotted as blue circles represent the concentration of the sulfur front measured in the in-situ experiment. Values were normalized to the maximum of S concentration in the PEDOT layer (indicated gray). From the decreasing intensity of sulfur front excitation, a vertical XSW field extension of $h_{\mathrm{XSW}} \approx 140$ nm can be estimated for the present experiments.

an X-ray energy of 10-15 keV, whereas h_{xsw} appears to be largely independent from the marker concentration in the front.

4.3 XSW Scans of Antimony Distributions

After the sulfur-based PIX reaction, a crosslinkinking process initiated by the dissociation of antimony containing surface groups was analyzed. Two different molecules including a propyl chain and a benzene ring (shown in Figure 4.13) were used as initiators for the crosslinking process. By analogy to the previous experiments, a front of SbF_6^- counterions is expected to be found at the top of the polymer layer, located between 56 and 126 nm above the silicon surface. The thickness of the layer was measured prior to XSW experiments using a profilometer.

Figure 4.13: Antimony containing surface groups used for the initiation of polymer crosslinking including a propyl chain (a) and a benzene ring (b). After heat-induced dissociation of the molecules, the carbocation starts the CROP process (in analogy to PEDOT-initiated crosslinking), thus a front of SbF_6^- counterions is expected to migrate through the polymer layer.

Fluorescence data and distribution scans are shown in Figures 4.15 (propyl) and 4.16 (benzene). Compared to the previous scans, the noise level of all measurements is relatively high. A possible reason is the low absolute amount of marker atoms caused by the relatively low sample size (ca. 1 cm^2) compared to the wafers of 3 cm in diameter, which were used for the PIX-processed samples of series A (shown in Figure 4.5).

Oscillations of the antimony fluorescence signal are detected neither for the propyl nor for the benzene containing initiator molecule and therefore, no evidence for the expected
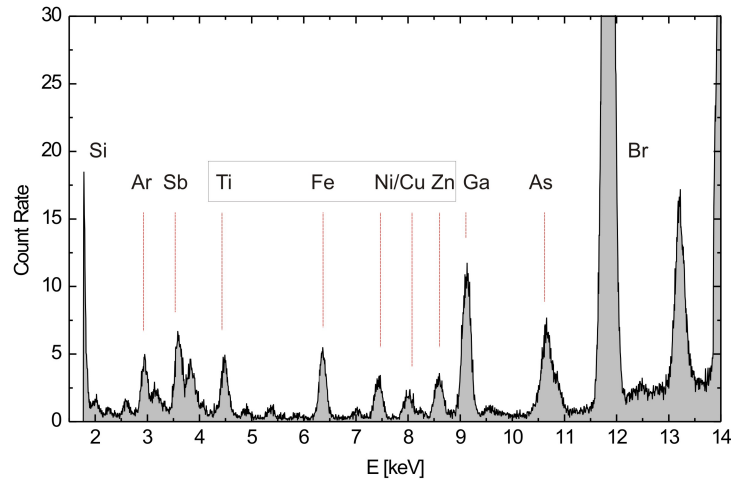
Figure 4.14:   Single spectrum from the XSW scan plotted in Figure 4.15 **c**.   Besides the fluorescence of Sb markers and Si substrate, a multitude of lines can be detected, originating from impurities of the sample material and scattering induced fluorescence of the components of the experimental setup.

formation of a counterion front is found. In most scans, no distinct maximum of fluorescence intensity can be identified. Instead, fluorescence intensity remains at a constant level between α_c^{sol} and α_c^{sub}, which indicates a broad distribution of SbF_6^- ions over the vertical range, as shown by the best-fit distribution models. In all distribution models, antimony concentration is highest at the silicon/polymer interface, which indicates that the concentration of counterions is largest in the near-interface layer.

In the sample belonging to measurement **b** of Figure 4.15, no antimony migration is detected at all. A similar effect is shown in diagram **c** of Figure 4.16 where most antimony has remained at the interface ($z \leq 5$ nm). A possible reason for this behavior is a too low oxetane concentration [79]. Unlike the previous XSW experiments on polymer layers, high count rates are recorded for angles smaller than α_c^{sol}. A similar effect was found in the measurements of ion distributions in liquid layers (cf. Figure 3.14). The appearance of marker fluorescence before this angle indicates a high roughness of the sample surface which lowers the resolution of XSW measurements.

In some scans, the occurence of X-ray resonance inside the polymer layers is indicated by the oscillation of scattering intensity. However, as in the sample discussed referring to Figure 4.11, no influence of these oscillations on marker fluorescence intensity is detected.
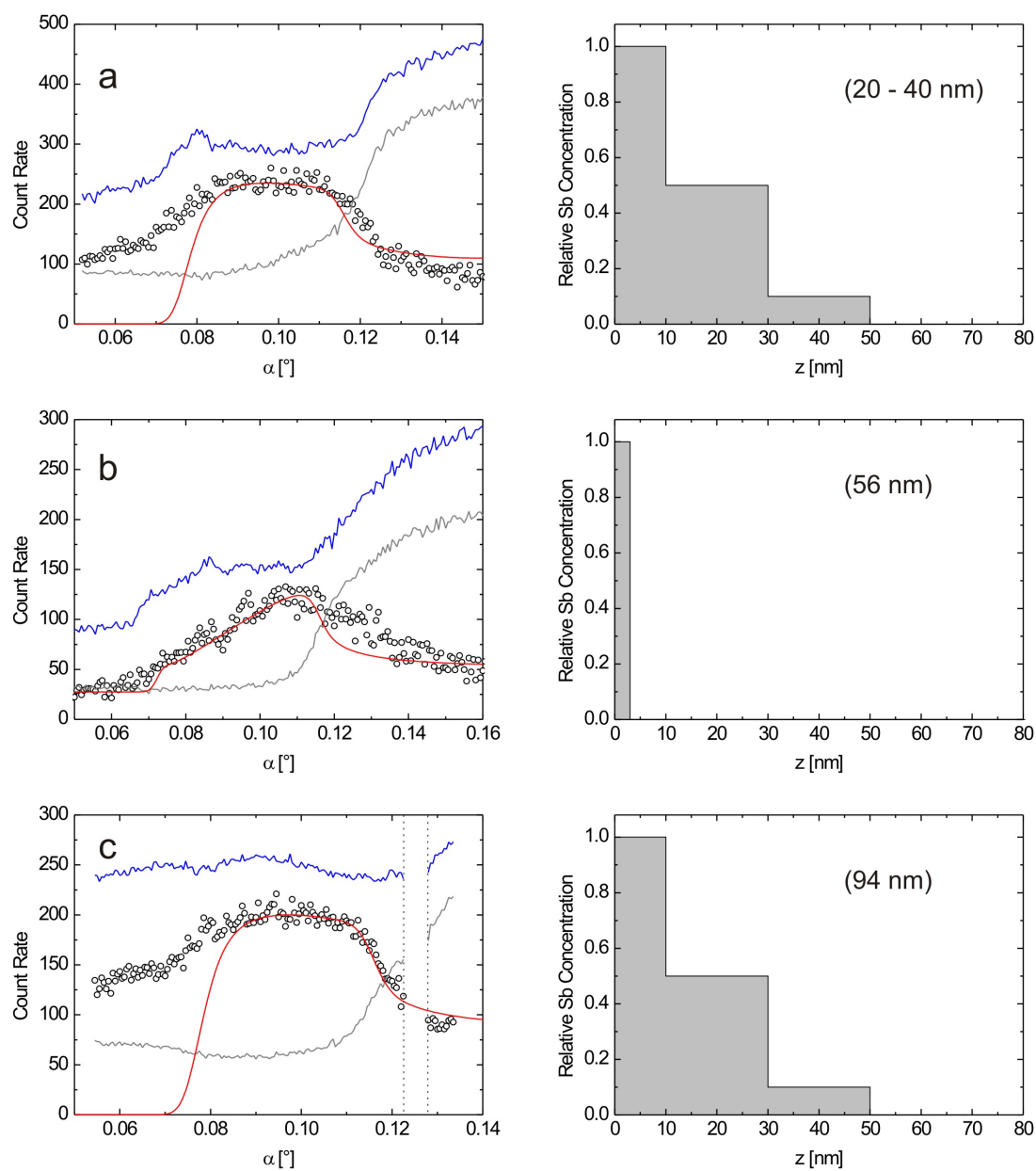
Figure 4.15: Standing waves analyses of polymer layers crosslinked using the propyl containing group as an initiator. No fluorescence intensity oscillations indicating the existence of a molecular front are seen, instead SbF_6^- ions are distributed over a broad vertical range. In the sample belonging to scan **b**, no detectable marker migration occurred as shown in the distribution model. The blue line indicates scattering intensity. The expected front height is given along with the distribution model. The lack of some data in plot **c** is due to a temporary malfunction of electronic components.
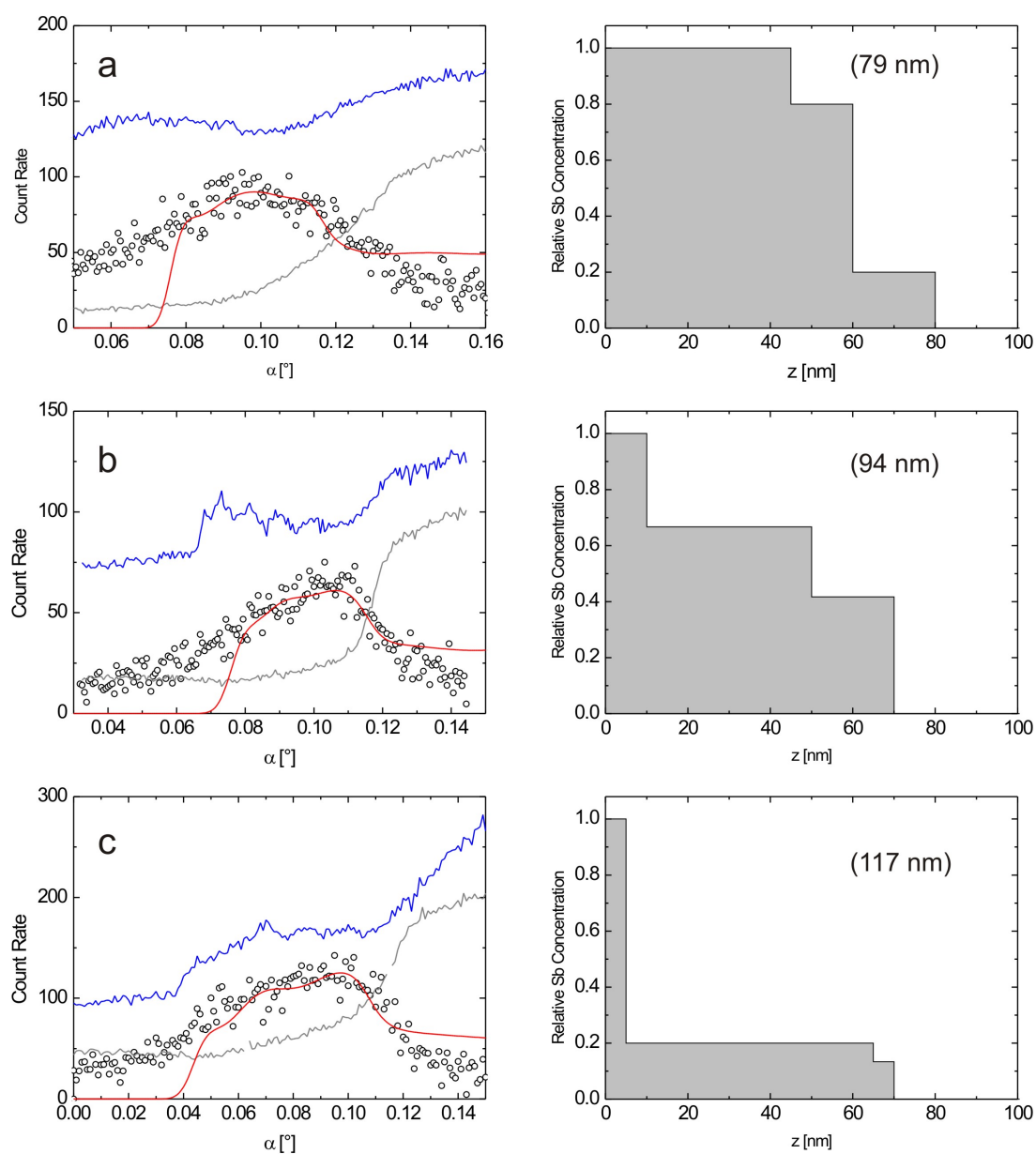
Figure 4.16: Standing waves analyses of polymer layers crosslinked using the benzene containing group as an initiator. Similar to the results shown in Figure 4.15, Sb markers are distributed continuously over the entire layer thickness, featuring a concentration maximum in the near-interface layer. No front-like distribution can be detected. The blue line indicates relative scattering intensity. The expected position of the counterion front is given along with the models.

Contrary to the sulfur containing samples, where only the peaks of silicon, sulfur and argon were detected, a great number of characteristic lines appears in these spectra. An example is shown in Figure 4.14. Gallium, arsenic and bromine fluorescence belong to impurities in the polymer, metallic elements are probably excited by scattered radiation hitting the components of the experimental setup. Therefore, secondary excitation and the overlap of peaks, which complicates fluorescence evaluation can not be excluded.

Summing up these observations, the results of the discussed XSW experiments lead to the conclusion that the antimony containing surface groups might not be as appropriate to the initiation of a crosslinking process as the PEDOT/PSS mixture used in the PIX process. Although stable polymer layers were produced, the effect of the broad SbF_6^- counterion distribution on the function of the OLED device is unclear. The reason for the detected crosslinking behavior could be an insufficient concentration of the initiator at the surface or of oxetane in the polymer.

Summary of Chapter 4

This chapter presented the results and the discussion of XSW experiments on polymer layers applied to the development of organic semiconductors. First, a general description of the sample composition and some specific X-ray optical properties of thin polymer layers were given, with the resulting criteria for fluorescence data useable for evaluation of XSW experiments. In the case of sample series A, the focus was on the characterization of a sulfur ion front inside the polymer, created by the polymerization reaction. The position and thickness of this front could be determined with an accuracy of few nanometres. This way, the proposed polymer crosslinking mechanism, allowing for a cost-effective production of stable multilayer OLEDs is evidenced. Next, the in-situ observation of the crosslinking reaction using XSW was described. The analysis of further PIX-processed polymer layer (series B) served to characterize the vertical intensity distribution of the standing waves. This way, the limit of the XSW field could be determined.

Chapter 5

Conclusion and Outlook

5.1 Conclusion

The subject of this work was the analysis of functionalized solid/liquid interfaces using X-ray standing waves (XSW). X-ray standing waves, generated by total external reflection of high-energy synchrotron radiation, were applied to determine elemental concentration profiles by angular resolved measurement of X-ray fluorescence. This experimental method is element sensitive, features a high in-depth resolution, works independently from vacuum conditions and has therefore proven to be ideally suited for the analysis of near-interface element distributions in liquid samples.

The investigation of functionalization methods, aimed to the manipulation of the charge and wetting properties of surfaces in contact with liquids, was the main topic of this work. First, the distribution of ions perpendicular to silicon wafer surfaces, which were modified by functional groups altering the interfacial charge were analyzed. Different types of concentration profiles, according to the Stern and the Gouy-Chapman models, were identified and evaluated as function of the pH value of the solution covering the functionalized surface. The Debye length of the diffuse ion layer could be determined accurately in the sub-nanometre range. In combination with streaming current measurements of the ζ-potential, a quantitative determination of the interfacial charge was achieved.

As further type of surface functionalization, the coating of silicon wafers with polyelectrolyte brushes was investigated. Applying a combination of infrared spectroscopic ellipsometry (IRSE) and standing waves, the assumed correlation of the protonation state of the carboxylic groups of the brushes and the distribution of ions both above and within

the brushes layer was confirmed. This way, the pH-controlled reversible switching of wetting properties of this modified surface was characterized. Furthermore, the penetration of ions into the brushes layer at alkaline pH was observed, which is suspected to affect the stability of the polymer brushes coating.

The second class of samples were thin polymer films on silicon wafers, being applied to the development of a new fabrication technique for multilayer organic light emitting diodes (OLEDs). Concerning X-ray optical properties, these films and the included element distributions behave like liquid layers. The concentration profile of sulfur ions inside these layers was measured and a thin reactive polymerization front was detected. Especially by the detection of this front, the proposed but so far unproven crosslinking mechanism, allowing for the production of OLEDs of high efficiency and lifetime, was verified. The position of the front was measured with an accuracy of up to 2 nanometres. Moreover, the heat-induced initiation of the crosslinking process could be verified by repeated XSW scans of one sample, where a variation of the sulfur distribution was observed during the heating process.

The experiments not only enabled the characterization of element concentration profiles of the analyzed samples, but also of the experimental method itself. In particular, the restriction of the range of application to markers within the first 140 nanometres above the reflecting interface, which is due to the limited coherence of the radiation was found. Here, the measuring range could be extended by the use of interfaces with a higher electron density contrast. This way, the critical angle of total reflection would be enlarged and by the resulting shortening of the beam path through the sample material the loss of coherence is expected to be reduced.

Also in the case of thin atom or ion layers, a limit of the applied method was reached: The vertical concentration profile of counterion front of the PIX-processed samples could not be measured by standing waves generated by total external reflection. Here, the measuring accuracy was limited by the shortest possible field period of approx. 20 nanometres. For further analysis of the polymerization front, an improvement of measuring accuracy is possible by the application of short-period XSW induced by Bragg reflection. Besides the XSW-excited fluorescence signal, also X-ray resonance was detected in the experiments with thin polymer layers. In the described measurements, this effect caused a disturbing superimposition of the fluorescence signal and therefore was avoided. However, in further experiments defined interference fields induced by X-ray resonance are expected to be an useful instrument for the characterization of element distributions.

5.2   Outlook

The interfaces analyzed in this thesis are related to the development of microfluidic systems and polymer-based semiconductors and are therefore of significant technological interest. Future projects will be focused more on biologically relevant interfaces. Lipid bilayers are planned to be analyzed as a model for cell membranes, the study of the ζ-potential and of static and dynamical ion distributions at the lipid/liquid interface could help to advance understanding of ion exchange processes at cell membranes [80]. Yet another important topic of research is the interaction of nanoparticles with biological material [81, 82]. Nanoparticles are of increasing use in commercial products, but the uptake of these particles into cells is suspected of having a toxic or carcinogenic effect and therefore requires closer investigation. For this purpose, the time-resolved measurement of fluorescence excited by static XSW fields of fixed incident angle are expected to be of use. The variation of fluorescence signal would not be caused by the use of dynamic XSW fields, but by the variation of the element distribution within the field. Such effects also occur during the long-term operation of OLEDs, where the diffusion of elements from the cathode material (indium and tin) into the polymer layer causes an accelerated aging and thus limits the lifetime of the device. Therefore, experiments with static XSW fields could also provide useful information for the characterization of the stability of OLEDs.

A further application for the future may be the combination of XSW measurements with X-ray absorption spectrometry techniques [83, 84]. This way, not only the in-depth distribution, but also their bonding state near interfaces can by determined, allowing for a sensitive near surface speciation.

Acknowledgements

Bibliography

[1] J. C. Skou, *Enzymatic Basis for Active Transport of Na$^+$ and K$^+$ Across Cell Membrane*, Physiological Reviews 45, **1965** (596-618)

[2] G. E. Brown Jr., V. E. Henrich, W. H. Casey, D. L. Clark, C. Eggleston, A. Felmy, D. W. Goodman, M. Grätzel, G. Maciel, M. I. McCarthy, K. H. Nealson, D. A. Sverjensky, M. F. Toney, J. M. Zachara, *Metal Oxide Surfaces and Their Interactions with Aqueous Solutions and Microbial Organisms*, Chemical Reviews 99, **1999** (77-174)

[3] A. H. Weerkamp, H. M. Uyen, H. J. Busscher, *Effect of Zeta Potential and Surface Energy on Bacterial Adhesion to Uncoated and Saliva-coated Human Enamel and Dentin*, Journal of Dental Research 67, **1988** (1483-1487)

[4] K. Rezwan, A. R. Stuart, J. Vörös, L. J. Gauckler, *Change of ζ Potential of Biocompatible Colloidal Oxide Particles upon Adsorption of Bovine Serum Albumin and Lysozyme*, Journal of Physical Chemistry B 109, **2005** (14469-14474)

[5] D.-Q. Lin, P. J. Brixius, J. J. Hubbuch, J, Thömmes, M.-R. Kula, *Biomass/Adsorbent Electrostatic Interactions in Expanded Bed Adsorption: A Zeta Potential Study*, Biotechnology and Bioengineering 83, **2002** (149-157)

[6] J. Sibarani, M. Takai, K. Ishihara, *Surface modification on microfluidic devices with 2-methacryloyloxyethyl phosphorylcholine polymers for reducing unfavorable protein adsorption*, Colloids and Surfaces B: Biointerfaces 54, **2007** (88-93)

[7] B. J. Kirby, A. R. Wheeler, R. N. Zare, J. A. Fruetel, T. J. Shepodd, *Programmable modification of cell adhesion and zeta potential in silica microchips*, Lab on a Chip 3, **2003** (5-10)

[8] B. J. Kirby, E. F. Hasselbrink Jr., *Zeta potential of microfluidic substrates: 1. Theory, experimental techniques, and effects on separations*, Electrophoresis 25, **2004** (187-202)

[9] V. Tandon, S. K. Bhagavatula, W. C. Nelson, B. C. Kirby, *Zeta potential and electroosmotic mobility in microfluidic devices fabricated from hydrophobic polymers: 1. The origins of charge*, Electrophoresis 29, **2008** (1092-1101)

[10] C.-Y. Lee, G.-B. Lee, L.-M. Fu, K.-H. Lee, R.-J. Yang, *Electrokinetically driven active micro-mixers utilizing zeta potential variation induced by field effect*, Journal of Micromechanics and Microengineering 14, **2004** (1390-1398)

[11] P. Mela, A. van den Berg, Y. Finitschenko, E. B. Cummings, B. A. Simmons, B. J. Kirby, *The zeta potential of cyclo-olefin polymer microchannels and its effects on insulative (electrodeless) dielectrophoresis particle trapping devices* Electrophoresis 26, **2005** (17921799)

[12] H. G. J. Moseley, *The high-frequency spectra of the elements*, Philosophical Magazine 26, **1913** (1024 - 1034)

[13] A. H. Compton, *The Total Reflexion of X-Rays*, Philosophical Magazine 45, **1923** (1121-1131)

[14] Y. Yoneda, T. Horiuchi, *Optical Flats for Use in X-Ray Spectrochemical Microanalysis*, Review of Scientific Instruments 42, **1971** (1069-1070)

[15] P. Wobrauschek, H. Aiginger, *Total-Reflection X-Ray Fluorescence Spectrometric Determination of Elements in Nanogram Amounts*, Analytical Chemistry 47, **1975** (852-855)

[16] J. Knoth, H. Schwenke, *An X-Ray Fluorescence Spectrometer with Totally Reflecting Sample Support for Trace Analysis at the ppb Level*, Fresenius Zeitschrift für Analytische Chemie 291, **1978** (200-204)

[17] J. Knoth, H. Schwenke, *A New Totally Reflecting X-Ray Fluorescence Spectrometer with Detection Limits below 10^{-11} g*, Fresenius Zeitschrift für Analytische Chemie 301, **1980** (7-9)

[18] H. D. Abruña, G. M. Bommarito, D. Acevedo, *The Study of Solid/Liquid Interfaces with X-ray Standing Waves*, Science 250, **1990** (69-74)

[19] M. J. Bedzyk, G. M. Bommarito, M. Caffrey, T. L. Penner, *Diffuse-Double Layer at a Membrane-Aqueous Interface Measured with X-Ray Standing Waves*, Science 248, **1990** (52-56)

[20] P. Fenter, L. Cheng, S. Rihs, M. Machesky, M. J. Bedzyk, N. C. Sturchio, *Electrical Double-Layer Structure at the RutileWater Interface as Observed in Situ with Small-Period X-Ray Standing Waves*, Journal of Colloid and Interface Science 225, **2000** (154-165)

[21] A. S. Templeton, T. P. Trainor, A. M. Sporman, G. E. Brown, *Selenium speciation and partitioning within Burkholderia cepacia biofilms formed on α-Al_2O_3 surfaces*, Geochimica et Cosmochimica Acta 67, **2003** (3547-3557)

[22] Z. Zhang, P. Fenter, L. Cheng, N. C. Sturchio, M. J. Bedzyk, M. L. Machesky, D. J. Wesolowski, *Model-independent X-ray imaging of adsorbed cations at the crystal-water interface* Surface Science Letters 554, **2004** (L95-L100)

[23] Z. Zhang, P. Fenter, L. Cheng, N. C. Sturchio, M. J. Bedzyk, M. Předota, A. Bandura, J. D. Kubicki, S. N. Lvov, P. T. Cummings, A. A. Chialvo, M. K. Ridley, P. Bénézeth, L. Anovitz, D. A. Palmer, M. L. Machesky, D. J. Wesolowski, *Ion Adsorption at the Rutile-Water Interface: Linking Molecular and Macroscopic Properties*, Langmuir 20, **2004** (4954-4969)

[24] M. J. Bedzyk, D. H. Bilderback, G. M. Bommarito, M. Caffrey, J. S. Schildkraut, *X-ray Standing Waves: A Molecular Yardstick for Biological Membranes*, Science 241, **1988** (1788-1791)

[25] M. Caffrey, J. Wang, *Membrane structure studies using X-ray standing waves*, Annual Review of Biophysics and Biomolecular Structure 24, **1995** (351-378)

[26] J. Wang, M. Caffrey, M. J. Bedzyk, T. L. Penner, *Structure changes in model membranes monitored by variable period x-ray standing waves: effect of Langmuir-Blodgett film thickness on thermal behavior*, Journal of Physical Chemistry 98, **1994** (10957-10968)

[27] R. Zhang, R. Itri, M. Caffrey, *Membrane Structure Characterization Using Variable-Period X-Ray Standing Waves*, Biophysical Journal 74, **1998** (1924-1936)

[28] T. P. Trainor, A. S. Templeton, G. E. Brown, G. A. Parks, *Application of the Long-Period X-ray Standing Wave Technique to the Analysis of Surface Reactivity*, Langmuir 18, **2002** (5782-5791)

[29] T. P. Trainor, A. S. Templeton, P. J. Eng, *Structure and reactivity of environmental interfaces: Application of grazing angle X-ray spectroscopy and long-period X-ray standing waves*, Journal of Electron Spectroscopy and Related Phenomena 150, **2006** (66-85)

[30] J. N. Israelachvili, *Intermolecular and Surface Forces*, Academic Press, London, **1985**

[31] J. Lyklema, *Fundamentals of Interface and Colloid Science, Vol. II*, Academic Press, London, **1995**

[32] H. L. F. von Helmholtz, *Ueber einige Gesetze der Vertheilung elektrischer Strme in körperlichen Leitern mit Anwendung auf die thierisch-elektrischen Versuche*, Annalen der Physik 89, **1853** (211-233)

[33] G. Gouy, *Sur la constitution de la charge électrique a la surface d'un électrolyte*, Journal de Physique Théorique et Appliquée 9, **1910** (457-468)

[34] D. L. Chapman, *A Contribution to the Theory of Electrocapillarity*, Philosophical Magazine 25, **1913** (475-481)

[35] O. H. Stern, *Zur Theorie der Elektrolytischen Doppelschicht*, Zeitschrift für Elektrochemie 30, **1924** (508)

[36] R. J. Hunter, *Foundations of Colloid Science*, Oxford University Press, Oxford, **2001**

[37] S. H. Behrens, D. G. Grier, *The charge of glass and silica surfaces*, Journal of Chemical Physics 115, **2001** (6716-6721)

[38] K. L. Williams, *Introduction to X-Ray Spectrometry*, Allen & Unwin, Boston, **1987**

[39] E. Bertin, *Principles and Practice of X-Ray Spectrometric Analysis*, Plenum Press, New York, **1975**

[40] L. G. Parrat, *Surface Studies of Solids by Total Reflection of X-Rays*, Physical Review 95, **1954** (359-369)

[41] M. Tolan, *X-ray Scattering from soft-matter thin Films*, Springer, Berlin, **1999**

[42] R. Klockenkämper, *Total Reflection X-Ray Fluorescence Analysis*, Wiley & Sons Inc., New York, **1997**

[43] D. K. G. de Boer, *Glancing-incidence x-ray fluorescence of layered materials*, Physical Rewiew B 44, **1991** (498-509)

[44] A. von Bohlen, M. Krämer, C. Sternemann, M. Paulus, *The influence of X-ray coherence length on TXRF and XSW and the characterization of nanoparticles observed under grazing incidence of X-rays*, Journal of Analytical Atomic Spectrometry 24, **2009** (792-800)

[45] A. von Bohlen, M. Brücher, B. Holland, R. Wagner, R. Hergenröder, *X-ray standing waves and scanning electron microscopy-energy dispersive X-ray emission spectroscopy study of gold nanoparticles*, Spectrochimica Acta B 65, **2010** (409-414)

[46] A. Röseler, *Spectroscopic ellipsometry in the infrared*, Infrared Physics 21, **1981** (349-355)

[47] K. Hinrichs, M. Gensch, N. Esser, *Analysis of Organic Films and Interfacial Layers by Infrared Spectroscopic Ellipsometry*, Applied Spectrosopy 59, **2005** (272A-282A)

[48] Y. Mikhailova, L. Ionov, J. Rappich, M. Gensch, N. Esser, S. Minko, K.-J. Eichhorn, M. Stamm, K. Hinrichs, *In Situ Infrared Ellipsometric Study of Stimuli-Responsive Mixed Polyelectrolyte Brushes*, Analytical Chemistry 79, **2007** (7676-7682)

[49] K. Hinrichs, K. Roodenko, J. Rappich, *In situ monitoring of the etching of thin silicon oxide films in diluted NH_4F by IR ellipsometry*, Electrochemistry Communications 10, **2008** (315-318)

[50] F. Evers, K. Shokuie, M. Paulus, C. Sternemann, C. Czeslik, M. Tolan, *Exploring the Interfacial Structure of Protein Adsorbates and the Kinetics of Protein Adsorption: An In Situ High-Energy X-ray Reflectivity Study*, Langmuir 24, **2008** (10216-10221)

[51] K. Giewekemeyer, T. Salditt, *Counterion distribution near a monolayer of variable charge density*, Europhysics Letters 79, **2007** (18003-p1 - 18003-p6)

[52] M. Brücher, P. Jacob, A. von Bohlen, J. Franzke, C. Sternemann, M. Paulus, R. Hergenröder, *Analysis of the Ion Distribution at a Charged Solid-Liquid Interface Using X-ray Standing Waves*, Langmuir 26, **2010** (959-966)

97

[53] J. Kim, J. Cho, P. M. Seidler, N. E. Kurland, V. K. Yadavalli, *Investigations of Chemical Modifications of Amino-Terminated Organic Films on Silicon Substrates and Controlled Protein Immobilization*, Langmuir, **2010** (in press, DOI 10.1021/la904027p)

[54] P. Jacob, personal notice.

[55] C. M. Johnson, P. R. Stout, *Interferences from Compton Scattering from Matrices of Low Atomic Number*, Analytical Chemistry 30, **1958** (1921-1923)

[56] E. D. Greaves, M. Angeli-Greaves, U. Jaehde, A. Drescher, A. von Bohlen, *Rapid determination of platinum plasma concentrations of chemotherapy patients using total reflection X-ray fluorescence*, Spectrochimica Acta B 61, **2006** (11941200)

[57] G. Andermann, J. W. Kemp, *Scattered X-Rays as Internal Standards in X-Ray Emission Spectroscopy*, Analytical Chemistry 30, **1958** (1306-1309)

[58] M. K. Tiwari, K. J. S. Sawhney, *Structural characterization of thin layered materials using x-ray standing wave enhanced elastic and inelastic scattering measurements*, Journal of Physics: Condensed Matter 22, **2010** (175003)

[59] R. J. Hunter, *Zeta Potential in Colloid Science - Principles and Applications*, Academic Press, London, **1981**

[60] J. Wang, M. Caffrey, M. J. Bedzyk, T. L. Penner, *Direct Profiling and Reversibility of Ion Distribution at a Charged Membrane/Aqueous Interface: An X-ray Standing Wave Study*, Langmuir 17, **2001** (3671-3691)

[61] L. A. Warren, F. Grant Ferris, *Kinetics of Fe(III) precipitation in aqueous solutions at pH 6.09.5 and 25°C*, Environmental Science & Technology 32, **1998** (2331-2337)

[62] M. Brücher, A. von Bohlen, P. Jacob, J. Franzke, M. Radtke, U. Reinholz, B. R. Müller, O. Scharf, R. Hergenröder, *The Charge of solid/liquid Interfaces measured by X-ray Standing Waves and Streaming Current*, ChemPhysChem 11, **2010** (2118-2123)

[63] H. Y. Erbil, *Surface Chemistry of Solid and Liquid Interfaces*, Blackwell Publishing, Oxford, **2006**

[64] K. Hinrichs, D. Aulich, L. Ionov, N. Esser, K.-J. Eichhorn, M. Motornov, M. Stamm, S. Minko, *Chemical and Structural Changes in a pH-Responsive Mixed Polyelectrolyten Brush Studied by Infrared Ellipsometry*, Langmuir 25, **2009** (10987-10991)

[65] D. Aulich, O. Hoy, I. Luzinov, M. Brücher, R. Hergenröder, E. Bittrich, K.-J. Eichhorn, P. Uhlmann, M. Stamm, N. Esser, K. Hinrichs, *In-situ studies on the switching behavior of ultrathin poly(acrylic acid) polyelectrolyte brushes in different aqueous environments*, Langmuir, **2010** DOI 10.1021/la101762f

[66] M. Krämer, K. Roodenko, B. Pollakowski, K. Hinrichs, J. Rappich, N. Esser, A. von Bohlen, R. Hergenröder, *Combined ellipsometry and X-ray related techniques for studies of organic nanocomposite films*, Thin Solid Films **2010**, DOI 10.1016/j.tsf.2010.04.033

[67] N. Houbenov, *Adsorption and Grafting of Polyelectrolytes at Solid-Liquid Interfaces*, Dissertation (TU Dresden), **2005**

[68] A. Köhnen, N. Riegel, J. H.-W. M Kremer, H. Lademann, D. C. Müller, K. Meerholz, *The Simple Way to Solution-Processed Multilayer OLEDs Layered Block-Copolymer Networks by Living Cationic Polymerization*, Advanced Materials 21, **2009** (879-884)

[69] M. C. Gather, A. Köhnen, A. Falcou, H. Becker, K. Meerholz, *Solution-Processed Full-Color Polymer Organic Light-Emitting Diode Displays Fabricated by Direct Photolithography*, Advanced Functionalized Materials 17, **2007** (191-200)

[70] K. Meerholz, Lecture at ISAS, 15. 7. 2010

[71] M. B. Smith, J. March, *March's Advanced Organic Chemistry*, John Wiley & Sons, New York, **2001**

[72] M. Krämer, A. von Bohlen, C. Sternemann, M. Paulus, R. Hergenröder, *Synchrotron radiation induced X-ray standing waves analysis of layered structures*, Applied Surface Science 253 **2007** (3533-3542)

[73] M. Krämer, A. von Bohlen, C. Sternemann, M. Paulus, R. Hergenröder, *X-ray standing waves: a method for thin layered systems*, Journal of Analytical Atomic Spectrometry 21 **2006** (1136-1142)

[74] V. K. Egorov, E. V. Egorov, *Planar waveguide-resonator: a new device for x-ray optics*, X-ray Spectrometry 33, **2004** (360371)

[75] H. Kiessig, *Interferenz von Rntgenstrahlen an dünnen Schichten*, Annalen der Physik 10 **1931** (769-788)

[76] J. Wang, M. J. Bedzyk, M. Caffrey, *Resonance-Enhanced X-rays in Thin Films: A Structure Probe for Membranes and Surface Layers*, Science 258, **1992** (775-778)

[77] R. S. Guico, S. Narayanan, J. Wang, K. R. Shull, *X-ray standing wave measurements of gold nanoparticles in polymeric thin films*, Macromolecules 37, **2004** (8357-8363)

[78] A. Köhnen, M. Brücher, A. Reckmann, H. Klesper, A. von Bohlen, R. Hergenröder, K. Meerholz (submitted)

[79] A. Reckmann, personal notice.

[80] J. K. R. Kendall, B. R. G. Johnson, P. H. Symonds, G. Imperato, R. J. Bushby, J. D. Gwyer, C. van Berkel, S. D. Evans, L. J. C. Leuken, *Effect of the Structure of Cholesterol-Based Tethered Bilayer Lipid Membranes on Ionophore Activity*, ChemPhysChem 11, **2010** (2191-2198)

[81] S. Patil, A. Sandberg, E. Heckert, W. Self, S. Seal, *Protein adsorption and cellular uptake of cerium oxide nanoparticles as a function of zeta potential*, Biomaterials 28, **2007** (4600-4607)

[82] A. E. Nel, L. Mädler, D. Velegol, T. Xia, E. M. V. Hoek, P. Somasundaran, F. Klaessig, V. Castranova, M. Thompson, *Understanding biophysicochemical interactions at the nano-bio interface*, Nature Materials **2009** (543-557)

[83] P. Pianetta, A. Singh, K. Luening, S. Brennan, T. Homma, N. Kubo, M. Watanabe, *Characterization of silicon wafer surfaces with SR-TXRF*, The Rigaku Journal 19, **2003** (36-44)

[84] F. Meirer, G. Pepponi, C. Streli, P. Wobrauschek, V. G. Mihucz, G. Záray, V. Czech, J. A. C. Broekaert, U. E. A. Fittschen, G. Falkenberg, *Application of synchrotron-radiation-induced TXRF-XANES for arsenic speciation in cucumber (Cucumis sativus L.) xylem sap*, X-ray Spectrometry 36, **2007** (408412)